EFFECTS OF TRANSITION METAL DISSOLUTION AND DEPOSITION ON LI-ION BATTERIES: A MULTI-SCALE APPROACH

by

Yoon Koo Lee

A dissertation submitted in partial fulfillment
of the requirements for the degree of
Doctor of Philosophy
(Mechanical Engineering)
in The University of Michigan
2015

Doctoral Committee:

Professor Wei Lu, Chair
Associate Professor Christian M. Lastoskie
Assistant Professor Jonghyun Park, Missouri University of Science and Technology
Professor Margaret S. Wooldridge

DEDICATION

To My Family

ACKNOWLEDGEMENTS

First, I would like to express my deepest gratitude to my advisors, Profs. Wei Lu and Ann Marie Sastry, for their outstanding guidance, encouragement, and support. Prof. Lu allowed me to explore various topics in Lithium ion battery. He always gave insights of the research and provided enormously helpful advice and support to me. Prof. Sastry provided me with the opportunity to work on the exciting research topic, Lithium ion battery. Her endless enthusiasm and effort always inspired me to be a better person as a scholar. I also would like to thank Prof. Jonghyun Park for his advice, support and discussion. He always provided me with better insight and support to the research without any hesitation.

I also would like to thank my committee members, Profs. Christian Lastoskie and Margaret Wooldridge for providing their important feedback. I truly appreciate their time and effort they volunteered to guide my dissertation work. I believe that their insightful comments have led this dissertation to be more thorough and complete.

I would also like to appreciate both former and current members of Sastry and Lu Groups, Dr. Jeong Hun Seo, Dr. Min Zhu, Dr. Greg Less, Dr. Ethan Eagle, Dr. Joseph Gallegos, Dr. Lin Liu, Dr. Sangmin Lee, Dr. Seungjun Lee, Dr. Dong Hoon Song, Dr. Sangwoo Han, Dr. Xianke Lin, Mr. Hosop Shin, Ms. Sahitya Reddivari and Mr. Guangyu Liu. Thank you for many helpful discussions and support. Also I would like to thank Ms. Leah Wright, Ms. Nichole Washington, Ms. Carol Lagemann, and Ms. Eve Bernos for their kind assistance and support. I am also deeply thank to my friends in both US and Korea for their encouragements and support.

Above all, I would like to express my deepest gratitude to my family. My family's unconditional love and support has sustained me through this endeavor. And finally, I thank to my fiance Jeong-woo Jang - without her support and love, I could never make this Ph.D journey.

I also wish to acknowledge the support of my research sponsors, including the U.S. Department of Energy and General Motors Corporation.

TABLE OF CONTENTS

LIST OF FIGURES

LIST OF TABLES

LIST OF SYMBOLS

A	the cleavage area of the slab structure
A_X	the cross-sectional area of the adsorbed molecule, m^2
c_i	*the concentration of species i in the electrolyte (*$i = Li^+, Mn^{2+}, H^+, H_2O$*),* mol/m^3
c_O	concentrations of the oxidation-form, mol/m^3
c_R	concentrations of the reduction-form, mol/m^3
c_s	concentration of lithium ions in the solid phase, mol/m^3
$c_{s,\max}$	the maximum solid phase concentration, mol/m^3
$c_{s,surf}$	surface solid phase concentration of lithium ions in the particle electrode, mol/m^3
C	empirical constant in BET methods
$D_{eff,i}$	effective diffusion coefficient of species *i* in the electrolyte ($i = Li^+, Mn^{2+}, H^+, H_2O$), m^2/s
$D^0_{Li^+}$	initial diffusion coefficient of lithium ions into the cathode material, m^2/s
E	electric potential,V
El	electrolyte solvent
E_{bulk}	energy of bulk structure per atom, eV
E_F	the formation energy of manganese vacancy, eV
E_{slab}	energy of the slab supercell, eV
f	electrochemical constant (equal to F/RT, where, F and R are Faraday and gas constant, respectively, and T is the absolute temperature), C/J

$f_{\pm}$	electrolyte activity coefficient
F	Faraday's constant, C/mol
G	the Gibbs free energy, eV
$i_{0,Li^{+}}$	exchange current of lithium intercalation/deintercalation reactions at cathode side, A/m^2
$i_{0,oxid}$	initial exchange current density due to solvent oxidation on cathode, A/m^2
$i_{H^{+}}$	current density of H deposition on the lithium foil, A/m^2
$i_{Li^{+},i}$	current density due to reaction of lithium at electrode i (i = cathode, anode), A/m^2
$i_{Mn^{2+}}$	current density of Mn deposition on the lithium foil, A/m^2
i_{Mn_redep}	current density of Mn re-deposition onto the cathode, A/m^2
i_{oxid}	current density generate due to solvent oxidation on the cathode, A/m^2
$i_{tot,i}$	sum of all the current density at electrode i (i = cathode, anode), A/m^2
I_{app}	applied total current density, A/m^2
$k_{b,Li}$	reaction rate constant of Li ion on Li metal surface, m^6/mol^{2}s
k_{decomp}	reaction rate constant of salt decomposition, m^6/mol^{2}s
$k_{H^{+}\_dep}$	reaction rate constant of hydrogen deposition on the lithium foil, A/m$^{0.5}$mol$^{0.5}$
$k_{Li^{+}}$	reaction rate constant in the positive electrode, A/m^2
k_{Mn}	reaction rate constant of Mn dissolution due to acid attack, m/s
k_{Mn_dep}	reaction rate constant of Mn deposition on the lithium foil, A/m$^{0.5}$mol$^{0.5}$
k_{Mn_redep}	reaction rate constant of Mn re-deposition onto the cathode, A/m$^{0.5}$mol$^{0.5}$
κ_{e}^{eff}	ionic conductivity of electrolyte phase, S/m
κ_{s}^{eff}	electronic conductivity of solid phase, A/m

n_e	number of electron exchange during charge transfer reactions
n_1	adjust factor of diffusion coefficient of Li ions
N	number of gas molecules adsorbed on surface
N_m	number of adsorbate molecules required to cover the solid with the layer
m	mass of the active material, g
m_d	the amount of dissolve manganese, g
m_i	the initial mass of the active material, g
M_A	the molar mass of the adsorbed molecule, g/mol
M_{Li^+}	molar mass of lithium ion, g/mol
p	applied pressure, N/m^2
p_0	saturated pressure, N/m^2
R	universal gas constant, J/mol K
$R_{contact}$	contact resistance of the electrode, Ω m^2
R_{ct}	charge transfer resistance of the electrode, Ω m^2
R_{decomp}	reaction rate of $LiPF_6$ salt decomposition reaction, mol/m^{3}s
R_{Mn}	reaction rate of manganese dissolution on the electrode surface, mol/m^{2}s
R_{oxid}	reaction rate of oxidation reaction on the electrode surface, mol/m^{2}s
SA	surface area of positive electrode, m^2/g
S_{a_oxid}	specific surface area for solvent oxidation reaction, 1/m
S_{a_pos}	specific surface area of positive electrode, 1/m
S_{a_sep}	specific surface area of separator, 1/m
t_+^0	lithium ion transference number in the electrolyte
t_e	electrode thickness, mm
T	room temperature, K
U_{Li^+}	equilibrium potential of lithium intercalation/deintercalation reactions, V

U_{Mn_dep}	equilibrium potential of the manganese deposition, V
U_{Mn_redep}	equilibrium potential of the manganese re-deposition, V
U_{oxid}	equilibrium potential of the solvent oxidation reaction, V
V	volume of active material, m^3
V_i	initial volume of active material, m^3
V_{LMO}	molar volume of active material, m^3
V_m	molar volume of positive electrode, m^3/mol
W	mass of gas molecules adsorbed on surface, g
W_m	mass of adsorbate molecules required to cover the solid with the layer, g
x	the intercalation level of lithium into the positive electrode
X_a	the ratio of initial and dissolved mass of manganese
α_{anode}	anodic transfer coefficient of lithium intercalation/deintercalation reactions
$\alpha_{cathode}$	cathodic transfer coefficient of lithium intercalation/deintercalation reactions
$\alpha_{a,oxid}$	anodic transfer coefficient of the solvent oxidation
$\alpha_{c,i}$	cathodic transfer coefficient of the side reactions ($i = Mn^{2+}, H^+$)
δ	Warburg prefactor
ε_{pos}	volume fraction of positive electrode
ε_{pos_0}	initial volume fraction of positive electrode
ε_2	porosity of the region of separator and positive electrode
μ	the reference chemical potential of the system
η_{Li^+}	overpotential for lithium intercalation/deintercalation reaction, V
η_{oxid}	overpotential of the solvent oxidation reaction, V
θ	fraction of occupied surface of gas molecules

ϕ_e	potential of the electrolyte phase, V
ϕ_s	potential of the solid phase, V
ω	Warburg impedance

LIST OF ABBREVIATIONS

AFM	Anti-Ferromagnetic
BET	Brunauer–Emmett–Teller
COHP	Crystal Orbital Hamiltonian Population
CV	Cyclic Voltammetry
DC	Direct Current
DMC	Dimethyl Carbonate
DOE	Department of Energy
DOS	Density of State
EC	Ethylene Carbonate
EDS	Energy Dispersive Spectroscopy
EIS	Electrochemical Impedance Spectroscopy
EOF	Enthalpy of Formation
EPM	Electron Probe Microanalysis
EV	Electric Vehicle
FM	Ferromagnetic
GCPL	Galvanostatic Cycling with Potential Limitation
GGA	Generalized Gradient Approximations
HEV	Hybrid Electric Vehicle
ICP-OES	Inductively Coupled Plasma – Optical Emission Spectroscopy
OCV	Open Circuit Voltage
PAW	Projected Augmented Wave
PDOS	Projected Density of State
PHEV	Plug-in Hybrid Electric Vehicle
PVDF	Poly Vinylidene Fluoride
RRDE	Rotating Ring Disk Electrode

SEI	Solid Electrolyte Interphase
SEM	Scanning Electron Microscope
SIMS	Secondary Ion Mass Spectrometry
SOC	State of Charge
TEM	Transmission Electron Microscopy
VASP	Vienna *Ab initio* Simulation Package
XPS	X-ray Photoelectron Spectroscopy

ABSTRACT

EFFECTS OF TRANSITION METAL DISSOLUTION AND DEPOSITION ON LI-ION BATTERIES: A MULTI-SCALE APPROACH

by

Yoon Koo Lee

In the past decade, lithium-ion (Li-ion) batteries have become increasingly important components in vehicle electrification due to their high power and energy density. However, Li-ion batteries exhibit degradations especially during long-term cycling or storage at elevated temperatures. One of the key degradation mechanisms of Li-ion batteries is transition metal dissolution of the cathode materials and deposition of transition metals onto the anode. Therefore, this dissertation investigates the fundamental physics underlying degradation mechanisms and presents effective solutions for minimizing metal dissolution and improving battery cell performance. Based on a series of experiments and numerical simulations, this dissertation 1) investigates manganese dissolution and deposition mechanisms, 2) predicts cell degradations, 3) presents an optimized ratio for composite electrodes, and 4) suggests approaches to reduce manganese dissolution. To obtain the results, a number of experiments were conducted to understand degradation phenomena and to provide input parameters for simulations. These experiments included 1) characterizations of both positive and negative electrodes, 2) quantifications of the amount of dissolved and deposited manganese, and 3) electrochemical measurements of the cell behaviors. Multi-scale simulations were implemented on both the cell scale and the atomistic scale. Cell scale simulations were employed to predict the cycle life of battery systems. Atomistic scale simulations were performed to investigate and subsequently minimize manganese dissolution. Moreover, comparisons between experiments and cell scale simulations were conducted to gain an advanced understanding of degradation mechanisms and to validate the simulations.

The current study found that both active material loss and electrode degradation due to manganese dissolution critically influence the performance of the cathode. Moreover, by depositing onto the anode, dissolved manganese ions accelerate the formation of the decomposed layer and continuously cause capacity fade. These results suggest that reducing manganese dissolution is necessary to improve battery capacity and cell performance. Finally, the current study suggests several effective solutions for minimizing and preventing manganese dissolution. These solutions include 1) optimization of the composition ratio in composite cathode and 2) surface treatments such as changing surface orientations and doping elements. Optimized composition ratio among active material, carbon black, and PVDF binder in $LiMn_2O_4$ composite electrode was found to be the important factor that maximizes the battery performance. Moreover, Mn dissolution from $LiMn_2O_4$ structures is strongly correlated with the electronic properties and bonding properties of the structure’s Mn-O bonds. In turn, these properties of Mn-O bonds were changed with different surface orientations and element doping, which suggests that changing surface orientations and doping elements effectively prevent Mn dissolution.

CHAPTER 1
INTRODUCTION

1.1 Lithium ion rechargeable battery-solution to future energy and environmental problems

As the number of vehicle on the road increases, global climate change and environmental impact become more critical. Gas emissions from automotive vehicles are believed to be one of the main factors of the rise of global temperatures and air pollution. In 2012, petroleum-fuel-powered vehicles contributed about 28% of the U.S. carbon dioxide (CO_2) emissions in the transportation sector as shown in Figure 1.1 [1]. One primary solution to reduce the gas emissions from transportation is to electrify automotive drivetrains. Electric vehicles on the road would help to decrease the emission of greenhouse gases and our dependence on petroleum-based fuels.

An electric vehicle is defined as any kind of vehicle with an electric powertrain, such as the Hybrid electric vehicle (HEV), the plug-in hybrid electric vehicle (PHEV) and the all-electric vehicle (EV). Electric vehicles are becoming more popular because they are more environmentally friendly, more energy efficient and more fuel efficient than petroleum-fuel-powered vehicles. For example, Figure 1.2 shows the actual and projected increase in production of battery-powered electric vehicle and demand for lithium by 2020. According to Deutsche Bank [2], the sales of battery-powered electric vehicles are expected to increase 10 times from 2008 to 2020. Because it is expected that most electric vehicles will be using Lithium-ion batteries, demand for Lithium is projected to increase exponentially by 2020. Both the sales portion of electric vehicles using lithium ion battery and lithium demand for electric vehicle are expected to increase significantly. In 2010, 96% of all hybrids available on the world market still run on nickel metal hydride batteries [3] because these batteries are relatively inexpensive and durable.

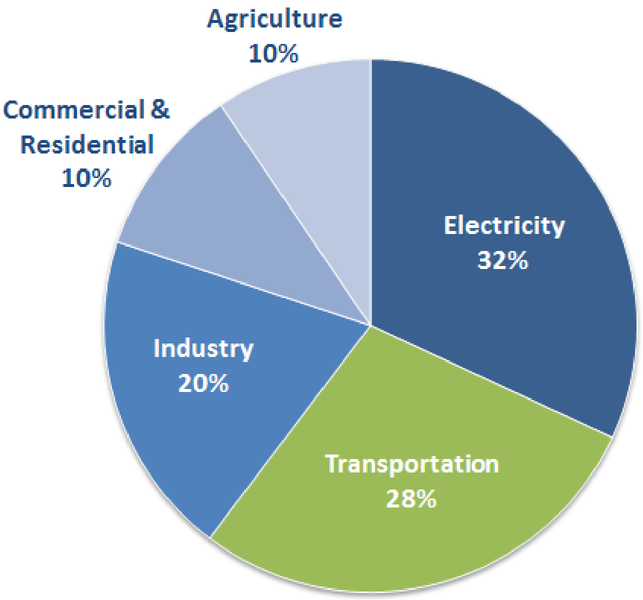

Figure 1.1 Total U.S. Greenhouse Gas Emissions by Economic Sector in 2012 [1]

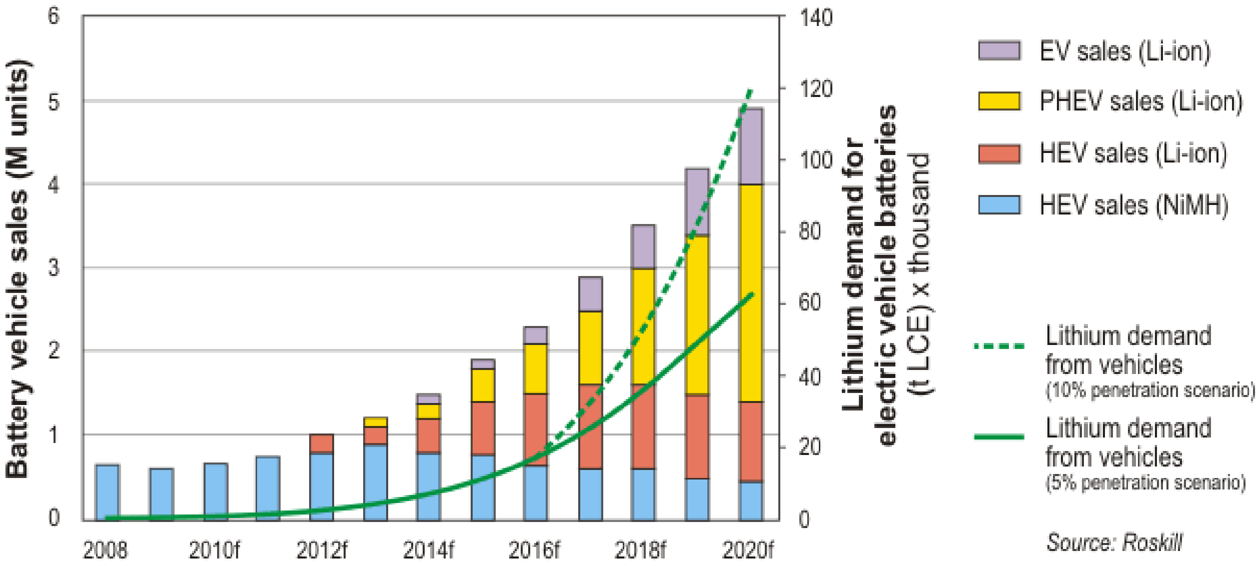

Figure 1.2 Electric vehicle production and lithium demand for electric vehicle batteries, from year 2008 to 2020 [3]

However, Lithium ion battery will likely replace nickel metal hydride batteries because of their higher energy density, higher power density and relatively longer service life. In fact, it is projected that in 2020, all PHEVs and EVs, and 70% of HEV will likely run on lithium-ion batteries. [3]

Despite their high energy density, power density and relatively long service life, Lithium-ion batteries must be improved and their cost reduced before they will be widely used as the main source of power in automotive vehicles. For example, the Department of Energy (DOE) sets specific goals that a plug-in hybrid electric vehicle (PHEV) must meet before they can be used more widely. The DOE challenge the industry to make a plug-in hybrid electric vehicle that has a range of 40 miles and a lifespan of 15 years. Figure 1.3 shows the performance of lithium ion batteries in 2011 compared to the target performance prescribed by the Department of Energy (DOE) goals. Figure 1.3 shows that Lithium-ion batteries perform inadequately in five of eight areas: cost, energy density, cycle life and calendar life, which means that in these areas of performance, lithium ion batteries need to be improved considerably.

1.1.1 **Energy density**

The energy density of lithium ion batteries may be increased through the use of advanced anode and cathode materials. Figure 1.4 shows advances in energy density of different battery types. Energy density of lithium ion battery continuously increased 300% from year 1995 to 2005. By contrast, the energy densities of Ni-Cd and Ni-MH batteries have flattened off in 1995 and 2000, respectively and have not increase since. Moreover, the energy density of lithium ion battery is 310% and 177% larger than Ni-Cd and Ni-H battery, respectively.

However, the energy densities of lithium ion batteries are still not sufficient to be used widely as the main source of power in automotive vehicles. Table 1.1 shows electric vehicles with battery type and driving range in 2010. Driving distances of the most electric vehicles are less than 100miles. The popularity and application of battery powered cars will rapidly increase if electric vehicles can offer 200 to 300 miles on a single charge. Therefore, energy density should be improved in order to increase the driving range without adding more batteries in electric vehicles.

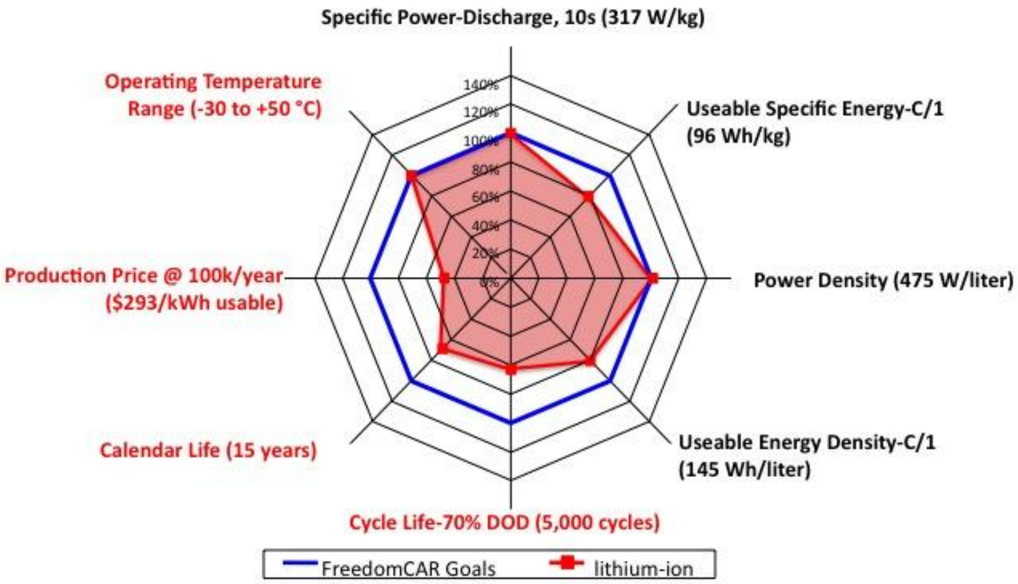

Figure 1.3 Current lithium ion battery technology (as of 2011) relative to PHEV targets (blue line) [4].

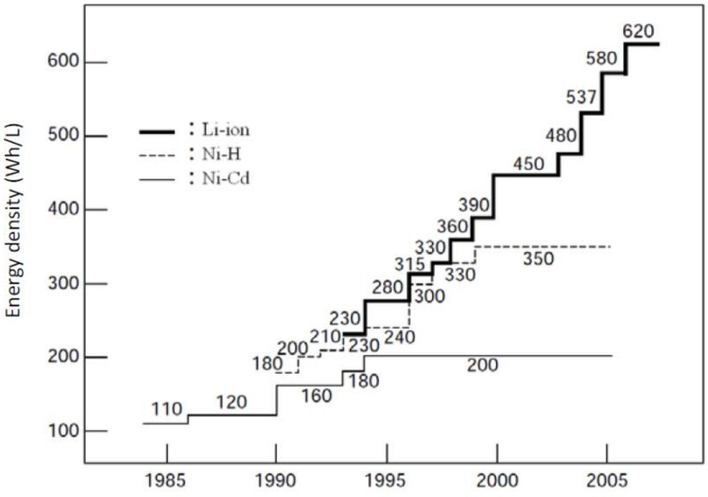

Figure 1.4 Advances in energy density of selected battery types, by year [5]

Electric vehicle	Battery	Range advertised	Range in real world	Charge times
BMW Mini E	35kWh, air cooled; 18650 cells; NMC 355V, 96s53p	250km, 156 miles	153km, 96 miles; 112km, 70 miles below freezing	26h at 115VAC; 4.5h at 230V, 32A
Chevy Volt	16kWh, liquid cooled Li-manganese, 181kg (400lb)	64km, 40 miles	45km, 28 miles; 149hp electric & 1.4 liter IC engine	10h at 115VAC; 4h at 230VAC
Toyota plug-in Prius	3 Li-ion packs, one for hybrid; two for EV, 42 temp sensors	20km, 13 miles	N/A; 80hp electric & 98hp IC engine	3h at 115VAC; 1.5h min 230VAC
Mitsubishi iMiEV	16kWh; 88 cells, 4-cell modules; Li-ion; 109Wh/kg; 330V	128km, 80 miles	88km, 55 miles; highway speed, mountain pass	13h at 115VAC; 7h at 230VAC
Nissan LEAF	24kWh; Li-manganese, 192 cells; 80Wh/kg, air cooled; 272kg (600lb)	160km, 100 miles	100km, 62 miles at highway speed with heater on	8h at 230VAC; 30 min high ampere
Tesla Roadster	56kWh, 6,831 Li-cobalt computer cells; liquid cooled	352km, 220 miles	224km, 140 miles; 172km, 108 miles driven sports car	3.5h at 230VAC high ampere
Think City	24.5kW, Li-ion or sodium-based	160km, 100 miles	N/A. Sodium-type has few problems	8h at 115VAC
Smart Fortwo ED	16.5kWh; cylindrical Li-ion (computer cells), made by Tesla Motors	136km, 85 miles	Less than predicted	8h at 115VAC 3.5H at 230VAC

Table 1.1 Electric vehicles with battery type and driving range (2010) [6]

1.1.2 **Safety**

Lithium ion batteries are not as safe as other rechargeable batteries because of their high energy density. Several factors could cause a lithium ion battery to explode, including short-circuiting and overcharging. During several charge/discharge cycles, some of the lithium ions form lithium metal deposits called ‘dendrite’ which is highly reactive. An electric current passing through these dendrites can short-circuit the battery, causing it to rapidly overheat and overcharge. When lithium ion batteries are short-circuited or overcharged, they can catch fire or explode. Moreover, chemicals that are used in lithium ion battery are also toxic to humans and the environment. Therefore, in order for lithium ion batteries to be used more widely, further safety measures and treatments need to be developed for vehicle use.

1.1.3 **Cost reduction**

The cost of Lithium ion battery is still relatively high. Currently, lithium-ion batteries cost about $1,000/KWh. However, the DOE’s goal is to reduce the cost down to $150/KWh, which needs to be further improved.

1.1.4 **Cycle life and calendar life**

Batteries are required to have reliable durability for deep cycles to keep longer life. Vehicle companies are aiming to develop lithium ion batteries with a guaranteed five year or 100,000 kilometer driving distance. However, as the cycle number increases, battery capacity also decreases rapidly. To further improve battery cycle life and calendar life, research related to capacity fade mechanism is active within the Li-ion battery research.

1.2 Lithium ion battery functions, components and materials

Figure 1.5 shows the electrochemical reactions within a lithium ion cell. A Lithium-ion cell consists of four main components: the positive electrode (cathode), the negative electrode (anode), electrolytes and the separator. During the discharge process, lithium ions are extracted from the anode (deintercalation) and inserted into the cathode (intercalation). Electrons are also moved through the external circuit from the anode to the cathode. These reactions occur spontaneously due to the voltage difference between two electrodes during the discharge process. During the charge process, lithium ions move in opposite directions. External current must be applied to move lithium ions and electrons during the charge process. In order to prevent short circuits by external currents, separators are placed in between cathode and anode. Electrolyte passes the lithium ion from one electrode to the other through the separator. Detailed lithium ion battery components, functions and materials can be found in Table 1.2.

Graphite is commonly used as the negative electrode of a Lithium-ion cell. Because graphite can reversibly place lithium ions between its many layers, it is also called lithium intercalation compound. It also has high energy densities with relatively low cost. On the other hand, transition metal oxide powders, such as $LiCoO_2$, $LiNiO_2$, $LiMn_2O_4$, $LiFePO_4$ and $Li(Ni_{1/3}Co_{1/3}Mn_{1/3})O_2$ are used as the positive electrode of a Lithium-ion cell. These transition metal oxides contain transition metals which possess two or more oxidation state, which make them as lithium intercalation compounds. The lithium ions are transported to and from the positive or negative electrodes by oxidizing and reducing the transition metal in a lithium ion cells. For example, manganese (Mn) ions in $Li_xMn_2O_4$ oxidizes from Mn^{3+} to Mn^{4+} during charge (lithium deintercalation), and reduces from Mn^{4+} to Mn^{3+} during discharge (lithium intercalation).

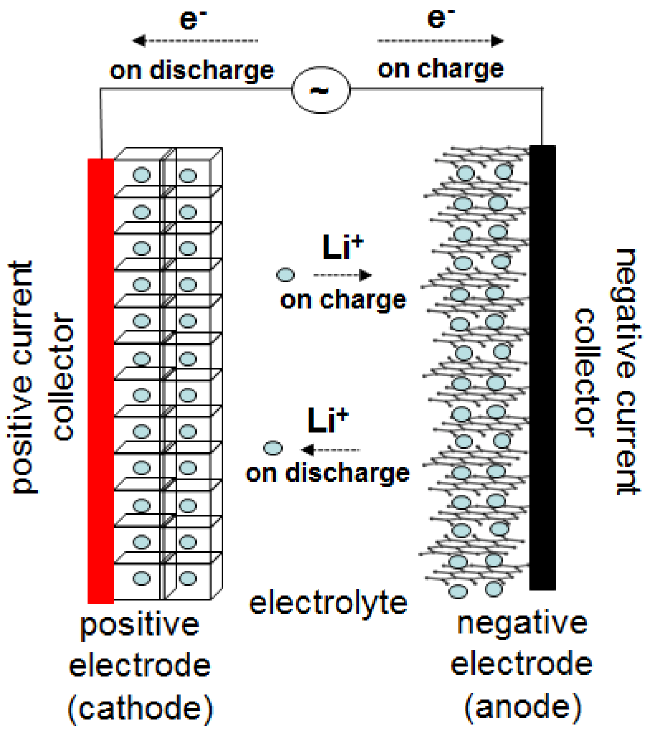

Figure 1.5 Charge/Discharge mechanisms of a lithium ion battery

Components	Functions	Materials
Cathode	- Emit lithium-ion to anode during charging - Receive lithium-ion during discharging	lithium metal oxide powder
Anode	- Receive lithium-ion from anode during charging - Emit lithium-ion during discharging	Graphite powder
Electrolyte	- Pass lithium-ions between cathode and anode	Lithium salts and organic solvents
Separator	- Prevent short circuit between cathode and anode - Pass lithium ions through pores in separator	Micro-porous membranes

Table 1.2 Lithium ion battery components, functions and materials

1.3 Lithium ion battery degradations- transition metal dissolution

Lithium intercalation compounds have become one of the most important components in vehicle electrification due to their high power density and energy density. However, these lithium intercalation compounds exhibit degradations especially during long-term cycling or storage at elevated temperatures. The degradation of the battery materials significantly reduces the capacity and power of the battery, which result in and decrease in performance and lifespan of the battery. In order to improve the performance, cycle life and calendar life of battery, understanding and preventing these degradation mechanisms are critical.

Degradation of batteries involves several chemical and physical processes of the components within the battery cell. The overview on basic degradation mechanisms of cathode materials is shown in Figure 1.6. Degradation of cathode materials includes transition metal dissolution, surface layer formation, micro cracking, contact loss to conducive particles, structural disordering and so on. [7-10]. To further improve battery performance, cycle life and calendar life, degradation of the battery should be understood and minimized.

Among the various degradation mechanisms, one of the key degradation mechanisms of Li-ion batteries involves transition metal dissolution of the cathode materials [11, 12]. Figure 1.7 shows the amount of transition metal dissolution of various lithium intercalation compounds. Among the various transition metals (Mn, Ni, Co, Fe, Zn), manganese showed the largest amount of dissolution in the lithium intercalation compounds [13]. Accordingly, substantial efforts have been made in previous studies to reduce manganese dissolution and improve battery performance among various cathode materials.

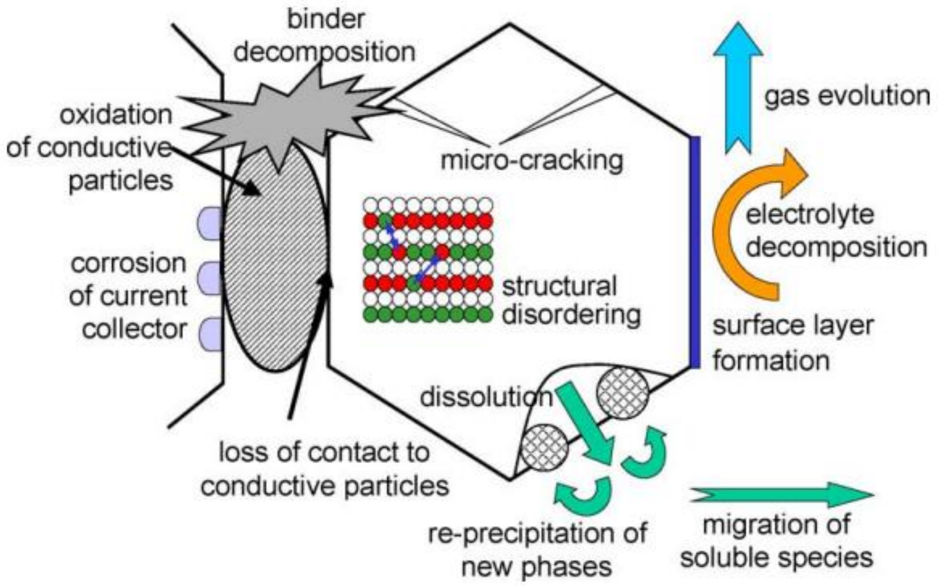

Figure 1.6 Overview on basic degradation mechanisms of cathode materials[10]

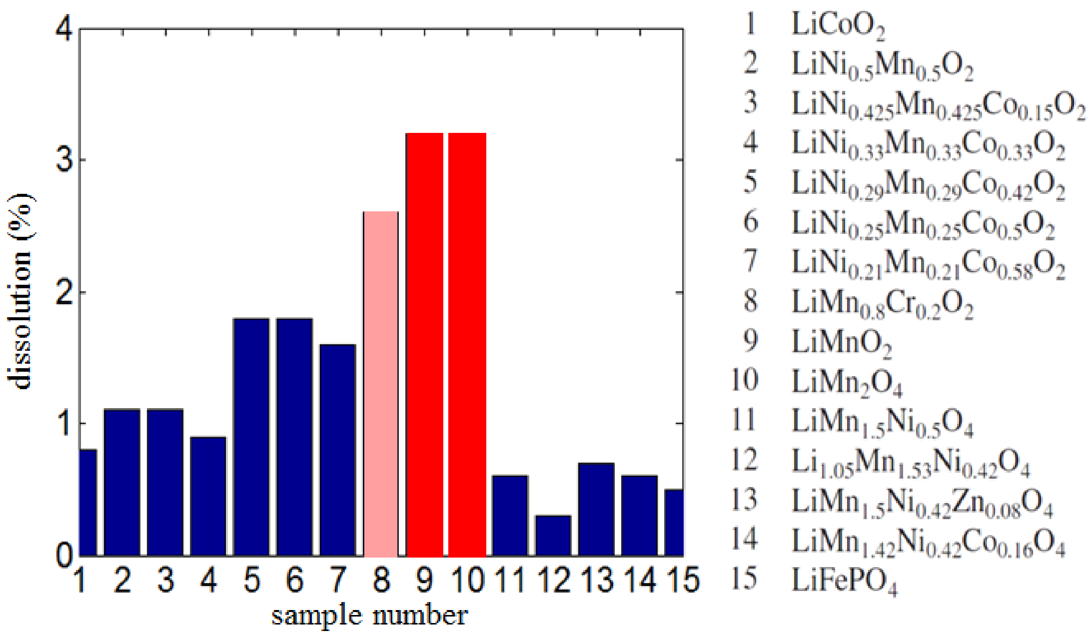

Figure 1.7 the amount of transition metal dissolution of various lithium intercalation compounds

Manganese dissolution can be attributed to several possible mechanisms. Manganese disproportionation reactions ($2Mn^{3+} \rightarrow Mn^{4+} + Mn^{2+}$) become faster in the discharged state, where Mn^{2+} ions can dissolve into the electrolyte [14]. Manganese ions also dissolve into the electrolyte when acids, generated by side reactions, attack the $LiMn_2O_4$ material. Acids such as hydrogen fluoride (HF) can be generated by two major side reactions: electrolyte oxidation and salt decomposition. Electrolyte oxidation produces hydrogen ions to form HF at voltages greater than 4.1V [15]. Salt decomposition generates hydrogen ions through the interaction of water and $LiPF_6$ salt in the electrolyte. These reactions are coupled with one another and cause capacity decrease, especially during cycling. The solubility of manganese ions also increases as a result of phase transformations in high or low voltage regions during cycling [16]. As the manganese ions dissolve into the electrolyte, several corresponding phenomena occur, including structural instability, the loss of active material, and an increase in contact resistance. All of these mechanisms are directly related to capacity fading in the $LiMn_2O_4$ electrode material.

Moreover, dissolved manganese ions are deposited onto the graphite anode and can deplete the lithium in the graphite anode [17]. Owing to manganese deposition onto the graphite, inserted lithium ions are taken out from the graphite electrode; consequently, overall capacity is decreased. It was reported that there was a close relationship between the amounts of deposited manganese and capacity fade as a function of temperature and storage time [18]. The accumulation of manganese at the electrode surface was confirmed by different measurement techniques such as XPS (X-ray photoelectron spectroscopy) [19], SIMS (secondary ion mass spectrometry) [20], ICP-OES (Inductively Coupled Plasma – Optical Emission Spectroscopy) [21] and EPM (Electron probe microanalysis) [21]. Several studies, however, show that lithium deintercalation due to manganese deposition cannot entirely explain capacity decrease. There must be accompanying side reactions related to manganese deposition—this is critically responsible for the capacity decrease of the graphite electrode [18, 21, 22]. In addition, Electrochemical Impedance Spectroscopy (EIS) [19] and Cyclic Voltammetry (CV) [19, 22] were applied to observe side reactions originating from manganese deposition. From these observations, it was proposed that additional manganese contained passivation layers similar to the SEI layers, which are produced on the surface of the graphite with the decomposed electrolyte products.

In turn, dissolved manganese ions not only deposit onto the negative electrode [12, 17-26], but also re-deposit onto the cathode surface and form electrically insulating oxides (Mn-O) or fluorides (Mn-F) [10, 27]. For example, these Mn-O and Mn-F compounds were detected on the surface of $LiMn_2O_4$ positive electrode using XPS after cycling [27]. In particular, it was observed that Mn-F compounds generated at later stage of the storage were highly resistive and led to cell polarization. These findings suggest that the manganese compounds on the cathode surface layer critically reduce the stability of $LiMn_2O_4$ spinel cathodes [10, 12, 27-31].

The objective of this work is to study the degradation of lithium ion batteries, particularly those with manganese containing cathode electrodes. In order to maximize the battery utilization and performance, manganese dissolution and deposition mechanisms should be fully analyzed. Manganese dissolution and deposition continuously decrease the active material and cycle-able lithium in the cell, respectively. In addition, cycling the battery cell creates several side reactions that are coupled with one another to make the reactions more complicated. For instance, HF generated by electrolyte oxidation attacks the active material and causes manganese dissolution. Deposited manganese ions on the graphite not only consume cycle-able lithium but also interact with SEI layer to make the layer thicker, which consequently result in degradation of the battery performance. Since side reactions caused by manganese dissolution/deposition impacts the battery performance in various ways, the current study employed multiple complementary measurements in various experimental conditions. Moreover, to predict the impact of manganese dissolution and deposition effect in two different operating conditions, electrochemical pseudo 2D model was implemented with important parameters from the experiment results.

The current study also aimed to expand its scope to composite electrode by including conductive additives and polymer binder. Composite electrode is the most widely used format of battery electrode in current industry. While $LiMn_2O_4$ cathode material provides high potential and high gravimetric energy densities (120~148 W h/kg), both polymer binder and conductive additives are used to maintain a firm structure and to provide continuous conduction path. Composition ratio among active material, binder, and additive materials of composite electrode influences interfacial reactions and side reactions, which are key factors in determining battery performance. In order to optimize the battery performance, optimal ratio of these constituents should be determined.

Lastly, in order to improve the battery performance, the current research investigates the effect of surface orientations and doping on the dissolution of Mn ions from $LiMn_2O_4$ structure using a first principle calculation. Our research aims to understand the reason why certain surface orientations and element doping is more beneficial to prevent manganese dissolution. By comparing electronic properties and structures with different surface and doping, manganese dissolution mechanisms and their prevention can be further understood.

In sum, the main purpose of this research is 1) to investigate manganese dissolution and deposition mechanisms, 2) to predict cell degradations, 3) to present optimized ratio for composite electrodes, and 4) to present guidance to reduce manganese dissolution.

1.4 Scope and outline of the dissertation

In Chapter 2, both experiment and simulation were applied to a system that excludes side reactions coupled with the anode materials to understand the reactions and degradations of $LiMn_2O_4$ composite cathode electrode. In order to develop a simulation tool capable of precisely predicting the degradation behavior of these batteries, accurate experimentally determined input parameters were essential. Thus, key parameters, including surface area, conductivity, and active material dissolution rate, were measured and used in a physics-based model that includes the most important degradations mechanisms: manganese dissolution, manganese deposition/re-deposition, solvent oxidation, salt decomposition, film formation, lithium reversibility, and lithium diffusion retardation. The current study observed that both active material loss due to degradation mechanisms and parameter changes due to degradation of the electrode critically influence cell performance.

Chapter 3 focuses on the side reactions occurred on graphite anode surface caused by manganese deposition. A Li/graphite composite electrode half-cell with dissolved manganese ions was used to investigate manganese deposition in order to focus on the degradation of graphite anode. Several electrochemical measurement techniques, such as CV, EIS, SEM, EDS and cycling testing, were employed to investigate how manganese ions influence the graphite electrode in terms of cell performance and capacity retention. Also, the interactions between SEI layer and manganese ions as well as the relationship between the lithiation-status of graphite and manganese deposition were examined by preparing different conditions of graphite electrode samples.

In Chapter 4, focuses are moved from $LiMn_2O_4$ materials to composite electrode by considering the effect of conductive additives and polymer binder. Effects of these components of $LiMn_2O_4$ composite electrode and their impacts on battery performance were investigated. Numerical simulation was conducted using updated simulation parameters with different composition ratio among active material, carbon black and PVDF binder in $LiMn_2O_4$ composite electrode.

In Chapter 5, the effect of surface orientations and doping on the dissolution of Mn ions from $LiMn_2O_4$ structure were investigated to prevent manganese dissolution using first principle calculations. Our research aims to understand the reason why certain surface orientations and element doping is more beneficial to prevent manganese dissolution. By comparing electronic properties and structures with different surface and doping, manganese dissolution mechanisms and their prevention can be further understood. The calculation results were validated and compared with previous calculation and experiment results.

BIBLIOGRAPHY

[1] The U.S. Environmental Protection Agency official website, http://www.epa.gov/ , accessed November, 26, 2014.

[2] Official Webpage of Deutsche Bank, http://www.db.com , accessed November, 26, 2014

[3] Ofiicial Webpage of Roskill, http://www.roskill.com/, accessed November, 26, 2014

[4] Official web page of the United States Advanced Battery Consortium (USABC), http://www.uscar.org/ , accessed November, 26, 2014.

[5] Ikoma, Munehisa, Matsushita Technical Journal,Retrieved August 4, 2010, http://panasonic.co.jp/ptj/v5204/pdf/p0101.pdf

[6] Official Webpage of battery university, http://batteryuniversity.com/, accessed November, 26, 2014.

[7] P. Arora, R.E. White, M. Doyle, Journal of The Electrochemical Society, 145 (1998) 3647-3667.

[8] Y. Dai, L. Cai, R.E. White, Journal of The Electrochemical Society, 160 (2013) A182-A190.

[9] D. Zhang, B.S. Haran, A. Durairajan, R.E. White, Y. Podrazhansky, B.N. Popov, Journal of Power Sources, 91 (2000) 122-129.

[10] J. Vetter, P. Novak, M.R. Wagner, C. Veit, K.C. Möller, J.O. Besenhard, M. Winter, M. Wohlfahrt-Mehrens, C. Vogler, A. Hammouche, Journal of power sources, 147 (2005) 269-281.

[11] J. Shim, R. Kostecki, T. Richardson, X. Song, K.A. Striebel, Journal of Power Sources, 112 (2002) 222-230.

[12] L. Yang, M. Takahashi, B. Wang, Electrochimica Acta, 51 (2006) 3228-3234.

[13] W. Choi, A. Manthiram, Journal of The Electrochemical Society, 153 (2006) A1760-A1764.

[14] R.J. Gummow, A. de Kock, M.M. Thackeray, Solid State Ionics, 69 (1994) 59-67.

[15] D.H. Jang, S.M. Oh, Journal of The Electrochemical Society, 144 (1997) 3342-3348.

[16] E. Iwata, K.-i. Takahashi, K. Maeda, T. Mouri, Journal of Power Sources, 81–82 (1999) 430-433.

[17] A. Biyr, C. Sigala, J Eletrochem Soc, 145 (1998) 194-209.

[18] H. Tsunekawa, S. Tanimoto, R. Marubayashi, M. Fujita, K. Kifune, M. Sano, Journal of The Electrochemical Society, 149 (2002) A1326-A1331.

[19] M. Ochida, Y. Domi, T. Doi, S. Tsubouchi, H. Nakagawa, T. Yamanaka, T. Abe, Z. Ogumi, Journal of The Electrochemical Society, 159 (2012) A961-A966.

[20] D.P. Abraham, T. Spila, M.M. Furczon, E. Sammann, Electrochemical and Solid-State Letters, 11 (2008) A226-A228.

[21] T. Tsujikawa, K. Yabuta, T. Matsushita, M. Arakawa, K. Hayashi, ECS Transactions, 25 (2010) 309-315.

[22] S. Komaba, N. Kumagai, Y. Kataoka, Electrochimica acta, 47 (2002) 1229-1239.

[23] S. Komaba, T. Itabashi, T. Ohtsuka, H. Groult, N. Kumagai, B. Kaplan, H. Yashiro, Journal of The Electrochemical Society, 152 (2005) A937-A946.

[24] C. Delacourt, A. Kwong, X. Liu, R. Qiao, W.L. Yang, P. Lu, S.J. Harris, V. Srinivasan, Journal of The Electrochemical Society, 160 (2013) A1099-A1107.

[25] M. Ochida, T. Doi, Y. Domi, S. Tsubouchi, H. Nakagawa, T. Yamanaka, T. Abe, Z. Ogumi, Journal of The Electrochemical Society, 160 (2013) A410-A413.

[26] C. Zhan, J. Lu, A.J. Kropf, T. Wu, A.N. Jansen, Y.-K. Sun, X. Qiu, K. Amine, Nature communications, 4 (2013).

[27] D. Kim, S. Park, O.B. Chae, J.H. Ryu, Y.-U. Kim, R.-Z. Yin, S.M. Oh, Journal of The Electrochemical Society, 159 (2012) A193-A197.

[28] K. Edström, T. Gustafsson, J.O. Thomas, Electrochimica Acta, 50 (2004) 397-403.

[29] Y. Matsuo, R. Kostecki, F. McLarnon, Journal of The Electrochemical Society, 148 (2001) A687-A692.

[30] M. Matsui, K. Dokko, K. Kanamura, Journal of The Electrochemical Society, 157 (2010) A121-A129.

[31] J. Lei, L. Li, R. Kostecki, R. Muller, F. McLarnon, Journal of The Electrochemical Society, 152 (2005) A774-A777.

CHAPTER 2

EXPERIMENT AND SIMULATION STUDY OF $LiMn_2O_4$ CATHODE DEGRADATION IN Li-ION BATTERY SYSTEM

Rechargeable batteries that use lithium intercalation compounds as the cathode have been extensively studied during the past decade. Spinel $LiMn_2O_4$ is one of the most widely used cathode materials in lithium ion battery systems because it offers the advantages of low cost, environmental friendliness, high electronic/ionic conductivity, excellent rate capability and safety. However, batteries that use spinel $LiMn_2O_4$ as a cathode material exhibit significant capacity fading, especially during long-term cycling or storage at elevated temperatures. Several mechanisms of capacity fading have been proposed in previous studies [1-4]. The dissolution of manganese is one of the most important causes, especially at elevated temperatures [5, 6].

Accordingly, previous simulation research has focused on manganese dissolution and deposition mechanisms to describe the degradation of battery performance. Park et al. [7] established mathematical models to predict the capacity fade resulting from manganese ion disproportional reactions. The reaction rate constant and the activation energies of manganese disproportionation reactions used in the model were obtained through experiments conducted under open circuit potential conditions using a particle electrode [8]. Park et al. suggested that disproportional reactions cause active material loss as well as a decrease in effective transport properties, which lead to capacity fade. Dai et al. [2] proposed a mathematical $LiMn_2O_4$/lithium half-cell model that also considered major side reactions, such as electrolyte oxidation, salt decomposition, manganese dissolution from acid attacks, and manganese deposition mechanisms. Lin et al.[9] also proposed side reactions that are coupled within a $LiMn_2O_4$/graphite full-cell model; these key degradation mechanisms include SEI layer formation, manganese dissolution and manganese deposition. Further, Lin et al. [9] proposed an explanation for why consecutive side reactions generate by-products, such as manganese ions, hydrogen ions and water molecules, that also leads to the loss of cycle-able lithium and active material.

The current study builds on these previous findings and expands our understanding of electrode degradation by investigating additional parameter changes caused by dissolved manganese ions. CV, EIS, and the capacity test were used to assess the effect of dissolved manganese ions on the performance of the $LiMn_2O_4$ positive electrode. In addition, key parameters such as the surface area, electronic conductivity, and the amount of manganese ions were measured and included in our simulations in an effort to better understand these phenomena. The current study considers both side reaction mechanisms and the degradation of the electrode to account for overall changes in the performance of the cathode electrode. The most important contribution of the current study is a comparison of the experimental results with those of the simulation. In particular, this study compares the degradation of the electrode and the changes in cell behavior using both experiment and simulation results.

2.1 Method

2.1.1 **Experimental method**

2.1.1.1 Fabrication of the $LiMn_2O_4$ composite electrode.

The positive $LiMn_2O_4$ composite electrodes were made from stoichiometric spinel $LiMn_2O_4$ powder (Sigma-Aldrich), carbon black, and PVDF binder (Kureha KF 7208) in a weight ratio of 90:5:5. $LiMn_2O_4$ powder and carbon black were added to the PVDF binder and mixed with Speedo Mixer (FlackTek Inc.) for 10 min. The mixed slurry was coated onto thin aluminum foil and vacuum dried at 100 ℃ for 24 h.

2.1.1.2 Conductivity measurements.

The conductivity of the composite electrode was measured using the four-point probe method. Mixed slurries of composite electrode were pasted onto a non-conductive glass substrate, and then dried in a vacuum at 100 °C for 24 h. A four-point probe DC method was applied to the composite electrode directly on the glass substrate using an EC-lab VMP3 Biologic potentiostat.

2.1.1.3 Surface area measurements.

The Brunauer–Emmett–Teller (BET) method was used to determine the surface area of the composite electrode. The surface area of the porous electrode was determined by:

$$SA = \frac{W_m N_A A_X}{M_A} \tag{2.1}$$

where W_m is the number of adsorbed molecules required to cover the solid with a layer of adsorbed molecules, N_A is the Avogadro constant, A_x is the cross-sectional area of the adsorbed molecule and M_A is the molar mass of the adsorbed molecule. For detailed calculation of conductivity measurement and surface area measurements, see the appendix.

2.1.1.4 Coin cell assembly and disassembly.

$LiMn_2O_4$ composite electrodes were assembled into sealed 2032 type coin cells (MTI) with lithium foil (Alfa Aesar) counter and reference electrodes with a separator (Celgard 2320).To investigate the direct impact of manganese ions on the $LiMn_2O_4$ composite electrode, the desired concentrations of manganese were dissolved in the electrolyte in advance. The target concentrations of manganese were obtained by dissolving $Mn(PF_6)_2$ at concentrations of 50, 100, 150 or 200 ppm in an electrolyte composed of 1M $LiPF_6$ salt (Aldrich) in a 1:1 mixture (v/v) of ethylene carbonate (EC) and dimethyl carbonate (DMC). Exact concentrations of manganese in the electrolyte were measured by using inductively coupled plasma–optical emission spectroscopy (ICP-OES).

2.1.1.5 Electrochemical measurements.

CV, capacity, and EIS measurements were performed to measure the impact of the manganese on the $LiMn_2O_4$ composite electrode. By using $LiMn_2O_4$ electrodes and different concentration of manganese in the electrolyte, $LiMn_2O_4$/lithium half cells were constructed to isolate the effect of the dissolved Mn-ion on the cathode side.

CV was applied to the Li/$LiMn_2O_4$ composite electrode to measure redox currents and current peak changes immediately following the addition of different concentrations of manganese. CV was carried out at 0.5 mV/s between 3.0V and 4.5V for Li/$LiMn_2O_4$ cell. Interfacial currents and current peak changes were measured during the formation cycles. Capacity was measured using Li/$LiMn_2O_4$ cells from 3.5 V to 4.3 V with C/10 for 20 cycles. EIS measurements were performed to measure impedance changes due to the different concentrations of manganese and to different potentials of the electrode/electrolyte interface. EIS measurements were performed at different voltages (3.5, 3.7, 3.9, 4.1 and 4.3V) with each of the manganese concentrations (0, 50, 100, 150 and 200 ppm) in the electrolyte. To achieve stabilized potentials before conducting EIS measurements, the cells were rested in the open circuit voltage (OCV) condition for 2 h. AC impedance spectra were obtained by applying sinusoidal waves with amplitudes of 5 mV over frequencies ranging from 100 kHz to 10 MHz.

2.1.1.6 Effective diffusion coefficient at the LiMn2O4 cathode, calculated using the EIS spectra of $LiMn_2O_4$/Li half-cell configurations

In the low-frequency region of the EIS spectrum, [10]

$$-Z_{\mathrm{Im}} = \delta\omega^{-1/2} \text{ or } -Z_{\mathrm{Re}} = \delta\omega^{-1/2} \tag{2.2}$$

and δ is expressed as

$$\delta = V_m (dE_{ocv} / dx) / zFS_{a\_pos} m (2D_{Li^+}^{eff})^{1/2} \tag{2.3}$$

where ω is the Warburg impedance, δ is the Warburg prefactor, V_m is the molar volume of the electrode, E_{ocv} is the open circuit potential, x is the intercalation level, z is the charge number, F is Faraday's constant, S_{a_pos} is the effective surface area, m is the mass of the active material and $D_{Li^+}^{eff}$ is the diffusion coefficient. The effective diffusion coefficient of the cathode electrode can be calculated using an OCV curve, the surface area of the electrode, and the EIS spectrum, applying equation (2.3).

2.1.1.7 ICP-OES measurements.

2.1.1.7.1 Dissolution and Deposition of Manganese due to Storage

$LiMn_2O_4$ composite electrodes were stored in 1mL of a 1.0 M solution of $LiPF_6$ in a 1:1 (v/v) mixture of EC and DMC to measure the dissolution of manganese. The positive composite electrodes were stored in the centrifuge tube at 0 ℃, 25 ℃ and 40 ℃ to observe the effect of temperature. Storage times were 1, 2, 3, 4 and 5 weeks. Five samples of each combination were measured. Three samples of $LiMn_2O_4$ powder in the separator were also stored in 1 mL of 1.0 M $LiPF_6$ in EC: DMC (1:1, v/v) for 1 week to compare the dissolution effect of composite electrodes and powder.

2.1.1.7.2 Dissolution due to cycling using an electrochemical cell

The concentration of manganese in the electrolyte was also measured to observe dissolution after a series of cycles. Initial formation cycling was performed 5 times before the actual cycling. The C rate for the formation cycles was C/10 and the C rate for cycling was C/5. The LiMn2O4 composite electrode/lithium cell was cycled from 3.5 V to 4.3 V using a Biologic VMP3 cycler. After cycling, the cell was disassembled and ICP-OES measurements were conducted to measure the concentration of manganese in the electrolyte.

2.1.2 **Simulation method**

2.1.2.1 Side reaction-coupled electrochemical modeling.

The battery cell model used in this study had the same configuration as the cells used in the experimental work. These cells consisted of a $LiMn_2O_4$ composite electrode, lithium foil, a separator and 1M $LiPF_6$ in EC: DMC (1:1, v/v), as shown in Figure 2.1. Experiments were carefully designed to investigate the degradation of the cathode material (cathode limiting cell). The modeling work also focused on the reactions and degradation of the cathodic side, thus a Li/LiMn$_2$O$_4$ half-cell model was also used in the simulation. Table 1 shows the parameters and constants of battery used in the simulations.

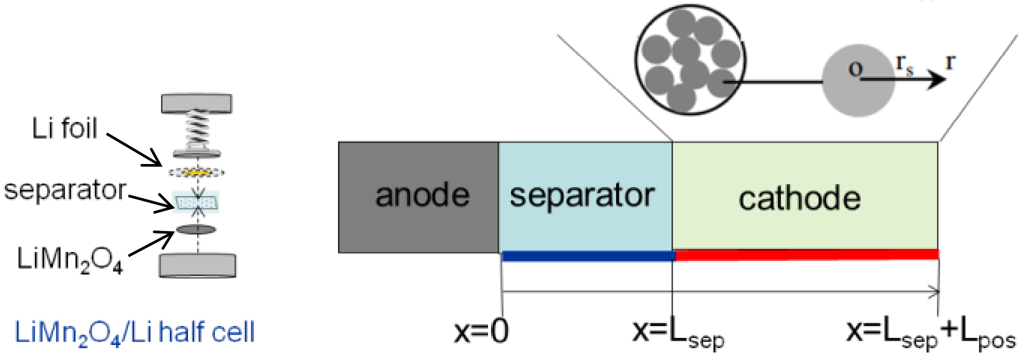

Figure 2.1 A schematic diagram of research outline of experiments and simulations

parameter	value	parameter	value
$c_{e,0}$ initial electrolyte phase concentration	1000 mol/m^3	κ_s^{eff} solid phase electronic conductivity	29.57 S/m
$c_{s,\max 0}$ initial maximum solid phase concentration	22730 mol/m^3	R Gas constant	8.314 J/mol K
$D^0_{Li^+}$ initial solid phase diffusion coefficient	1.31×10^{-12} m^2/s	t^0_+ transference number	0.363
$f_\pm$ electrolyte activity coefficient	1	T temperature	298 K
F Faraday's constant	96487 C equiv^{-1}	α_{anode} anode transfer coefficient	0.5
I_{app} Applied current density	3 A/m^2	$\alpha_{cathode}$ cathode transfer coefficient	0.5
L_{pos} length of positive electrode	50×10^{-6} m	ε_{pos_0} initial volume fraction of positive electrode	0.297
L_{sep} length of separator	50×10^{-6} m	ε_2 porosity of electrolyte	0.444
$k_{b,Li}$ reaction rate constant of Li ion on Li metal	6.1e-6 A/m^2	Initial electrode SOC	0.99
k_{Li^+} reaction rate constant in the positive electrode	1e-5 A/m^2	Initial voltage	3.6 V

Table 2.1 Key parameters of cathode electrode in the simulations

parameter	value	parameter	value
$c_{H^+,0}$ initial H$^+$ ion concentration	4 mol/m^3	k_{Mn} reaction rate constant of Mn dissolution	4.1×10^{-12} m/s
$c_{H_2O,0}$ initial H$_2$O ion concentration	4 mol/m^3	k_{Mn_dep} reaction rate constant of Mn deposition	1.3×10^{-9} Am/mol
$c_{Mn^{2+},0}$ initial Mn^{2+} ion concentration	0 mol/m^3	k_{Mn_redep} reaction rate constant of Mn re-deposition	1.3×10^{-9} Am/mol
n adjust factor of diffusion coefficient of Li ions	0.12	U_{H_dep} equilibrium potential of the H$^+$ deposition	2.5V
D_{eff,H^+} diffusion coefficient of H$^+$ ions	5×10^{-9} m^2/s	U_{Mn_dep} equilibrium potential of the Mn deposition	1.5 V
D_{eff,H_2O} diffusion coefficient of H$_2$O molecules	3×10^{-9} m^2/s	U_{oxid} equilibrium potential of the solvent oxidation reaction	4.2 V
$D_{eff,Mn^{2+}}$ diffusion coefficient of Mn^{2+} ions	0.72×10^{-9} m^2/s	$\alpha_{a,oxid}$ anodic transfer coefficient of the solvent oxidation	0.01
k_{decomp} reaction rate constant of salt decomposition	7.13×10^{-10} m^6/mol^{2}s	$\alpha_{c,Mn^{2+}}$ cathodic transfer coefficient of Mn^{2+} deposition	0.5
k_{H_dep} reaction rate constant of hydrogen deposition	2.07×10^{-8} Am/mol	α_{c,H^+} cathodic transfer coefficient of H$^+$ deposition	0.5
$S_{a\_side}i_{0,oxid}$ current generated due to solvent oxidation	10 A/m^3	α_{Mn_redep} anodic transfer coefficient of the solvent oxidation	0.01

Table 2.2 Side reaction parameters of the battery in the simulations

The major reactions considered in this study were solvent oxidation, salt decomposition, hydrogen reduction, manganese dissolution, manganese deposition and manganese re-deposition.

There are two major reaction mechanisms by which manganese dissolves into the electrolyte. Trivalent manganese ions disproportionate into divalent manganese ions and tetravalent manganese ions, [11-13], as described by the reaction:

$$Mn^{3+} \rightarrow Mn^{4+} + Mn^{2+} \tag{2.4}$$

Mn^{2+} ions dissolve in the electrolyte, which causes active material loss and additional reduction on both electrodes. This reaction is accelerated when the portion of Mn^{3+} is high, especially in the discharged state. Active material loss can be described as a volume change of the electrode:

$$V(T,t) = V_i(1 - X_a) \tag{2.5}$$

where X_a stands for the ratio of the initial and dissolved masses of manganese, defined as:

$$X_a(T,t) = \frac{m_d(T,t)}{m_i} \tag{2.6}$$

where m_d is the amount of dissolved manganese and m_i is the initial mass of the active material.

Acid attack on the active material is also responsible for manganese dissolution. The reaction is described [14-16] by the equation:

$$4H^+ + 2LiMn_2O_4 \rightarrow 2Li^+ + Mn^{2+} + \frac{3}{2}Mn_2O_4 + 2H_2O \tag{2.7}$$

The reaction rate of manganese dissolution due to acid attack can be expressed as

$$R_{Mn} = k_{Mn}c_{H^+} \tag{2.8}$$

where k_{Mn} is the reaction rate constant of Mn dissolution due to acid attack and c_{H^+} is the concentration of hydrogen ions.

Jang et al. [17] observed that manganese dissolution accelerated when storing the electrode at higher voltage, compared to rate during storage at lower voltage. They explained that the dependence of manganese dissolution on the potential arises from solvent oxidation on the positive electrode. Solvent decomposition generates hydrogen ions and electrons, which can be expressed [15, 18, 19] as:

$$solvent \rightarrow oxidized\ products + H^{+} + e^{-} \tag{2.9}$$

The rate of solvent decomposition [19], which is an irreversible reaction, can be described using the Tafel equation:

$$i_{oxid} = i_{0,oxid} \exp\left(\frac{\alpha_{a,oxid} F}{RT} \eta_{oxid}\right) \tag{2.10}$$

where i_{oxid} is the current density used to generate side reactions, $\alpha_{a,oxid}$ is the anodic transfer coefficient of the electrolyte decomposition reactions, F is Faraday's constant, R is the universal gas constant and T is the temperature. The parameter η_{oxid} is the overpotential of the decomposition reaction, which can be described as

$$\eta_{oxid} = \phi_s - \phi_e - U_{oxid} \tag{2.11}$$

The rate of the solvent decomposition reaction can be described as follows:

$$R_{oxid} = \frac{i_{oxid}}{F} \tag{2.12}$$

where U_{oxid} is the potential of the solvent oxidation reaction and ϕ_s and ϕ_e are the potentials of the solid phase and electrolyte, respectively.

Decomposition of the electrolyte containing $LiPF_6$ salt produces H^+ ions. $LiPF_6$ initially decomposes as follows:

$$LiPF_6 \rightarrow LiF + PF_5 \tag{2.13}$$

and then PF_5 reacts with water to form HF:

$$PF_5 + H_2O \rightarrow 2HF + POF_3 \tag{2.14}$$

The rate of the $LiPF_6$ decomposition reaction is given by: [20, 21]

$$R_{decomp} = k_{decomp} c_{H_2O}{}^{2} c_{Li^+} \tag{2.15}$$

Since the concentration of PF_5 is relatively high, the water content of the cell governs the rate of reaction (2.14). However, sine water is produced by the attack of HF on the active material from reaction (2.7), manganese dissolution will continuously accelerate in the cell.

The model consists of 8 different partial different equations that were coupled and solved simultaneously to describe the reaction mechanisms on the cathode :

2 charge conservation equations for Li^+ in each solid and electrolyte phase.

4 equations describing the transport of Li^+, H^+, Mn^{2+} and H_2O in the electrolyte phase.

1 equation describing the transport of Li^+ in the solid phase, near the cathode.

1 partial different equation describing the change in the volume fraction of the active material in the solid phase due to manganese dissolution, which can be described as:

$$\frac{\partial \varepsilon_{pos}}{\partial t} = -S_{a\_pos} k_{Mn} c_{H^+} V_{LMO} \tag{2.16}$$

where V_{LMO} is the molar volume of the active material of the electrode.

The initial conditions used with the equation regarding volume fraction of the cathode were:

$$\varepsilon_{pos0} = \varepsilon_{pos\_init,} \quad \text{at } t = 0 \tag{2.17}$$

$$\frac{d\varepsilon_{pos0}}{dt} = 0, \text{ at } t = 0 \tag{2.18}$$

Charge conservation in the cathode and the electrolyte phase can be described using the following equations:

$$\nabla \cdot \left(\kappa_s^{eff} \nabla \phi_s \right) - i_{tot} = 0 \tag{2.19}$$

$$\nabla \cdot \left(\kappa_e^{eff} \left(\nabla \phi_e - \frac{2RT}{F} \left(1 - t_+^0\right) \left(1 + \frac{d \ln f_\pm}{d \ln c_{Li^+}} \right) \nabla \ln c_{Li^+} \right) \right) + i_{tot} = 0 \tag{2.20}$$

Boundary conditions of the charge conservation of solid phase yields:

$$-\kappa_s^{eff} \left. \frac{\partial \phi_s}{\partial x} \right|_{x=L_{sep}} = 0 \quad , \quad -\kappa_s^{eff} \left. \frac{\partial \phi_s}{\partial x} \right|_{x=L_{sep}+L_{pos}} = I_{app} \tag{2.21}$$

Anode surface ($x = 0$ *)*:Mn^{2+} and H^+ are reduced at the lithium foil when charging the cell, which can be expressed by

$$Mn^{2+} + 2e^- \rightarrow Mn \tag{2.22}$$

$$2H^+ + e^- \rightarrow H_2 \tag{2.23}$$

Boundary conditions for the species H$^+$ and Mn^{2+} yield:

$$-D_i^{eff} \left.\frac{\partial c_i}{\partial x}\right|_{x=0} = \frac{i_i}{F}, \quad i = H^+, Mn^{2+} \tag{2.24}$$

where i_i, $i = H^+, Mn^{2+}$ when charging are expressed by the equations:

$$i_{Mn^{2+}} = k_{Mn\_dep} c_{Mn^{2+}} \left[-\exp(-\frac{\alpha_{c,Mn^{2+}} F}{RT}(\phi_1 - \phi_2 - U_{Mn\_dep})) \right] \tag{2.25}$$

$$i_{H^+} = k_{H^+\_dep} c_{H^+} \left[-\exp(-\frac{\alpha_{c,H^+} F}{RT}(\phi_1 - \phi_2 - U_{H\_dep})) \right] \tag{2.26}$$

Current generated as the result of hydrogen and manganese reduction during charging follows the Butler-Volmer equation and is also a function of the concentration of the each species in the cell.

At the anode surface ($x = 0$), the potential of the solid phase is set to zero.

$$\phi_s|_{x=0} = 0 \tag{2.27}$$

The total applied current should be the sum of the current density of lithium, the manganese deposition, and the hydrogen deposition on the anode surface, which can be described as

$$i_{tot,anode} = i_{Li^+,anode} + i_{Mn^{2+}} + i_{H^+} \tag{2.28}$$

where

$$i_{Li^+,anode} = -k_{b,Li} c_{Li^+}^{0.5} [\exp(\frac{\alpha_{anode} F}{RT}(\phi_1 - \phi_2)) - \exp(-\frac{\alpha_{cathode} F}{RT}(\phi_1 - \phi_2))] \tag{2.29}$$

Boundary conditions for the electrolyte phase can be expressed as:

$$-\kappa_e^{eff} \left.\frac{\partial \phi_e}{\partial x}\right|_{x=0} = -\kappa_e^{eff} \left.\frac{\partial \phi_e}{\partial x}\right|_{x=L_{sep}+L_{pos}} = 0 \tag{2.30}$$

It is assumed that the contributions of Mn^{2+} and H$^+$ species to the electric field are neglected. The concentration of Li$^+$ (1000 mM LiPF$_6$) is significantly higher than the concentrations of Mn^{2+} (1.016 mM after 50 cycles, from experiment results) and H$^+$ (less than 50 ppm), which are negligible.

Four species in the transport equation have different reactions within the different domains of the system. The individual material balance equations for H^+, Mn^{2+} and H_2O are coupled to each other.

First of all, the electric field is only influenced by Li^+ from the assumption above,

$$-D_{eff,Li^+}\nabla \frac{\partial c_{Li^+}}{\partial x}\bigg|_{x=0} = \frac{1-t_+^0}{F} i_{Li^+,anode} \qquad (2.31)$$

Boundary conditions at the anode ($x=0$) for the H_2O species are

$$\frac{\partial c_i}{\partial x}\bigg|_{x=0} = 0, \quad i = H_2O \qquad (2.32)$$

Separator region ($x=0$ to $x=L_{sep}$):At the separator region, Mn dissolution and solvent oxidation do not react and only electrolyte decomposition occurs. The following reactions apply in this region:

$$\frac{\partial\left(\varepsilon_2 c_{Li^+}\right)}{\partial t} = \nabla\cdot\left(D_{eff,Li^+}\nabla c_s\right) - R_{decomp} \qquad (2.33)$$

$$\varepsilon_2 \frac{\partial c_{H^+}}{\partial t} = \nabla\cdot(D_{eff,H^+}\nabla c_{H^+}) + 2R_{decomp} \qquad (2.34)$$

$$\varepsilon_2 \frac{\partial c_{Mn^{2+}}}{\partial t} = \nabla\cdot(D_{eff,Mn^{2+}}\nabla c_{Mn^{2+}}) \qquad (2.35)$$

$$\varepsilon_2 \frac{\partial c_{H_2O}}{\partial t} = \nabla\cdot(D_{eff,H_2O}\nabla c_{H_2O}) - R_{decomp} \qquad (2.36)$$

Boundary conditions at the separator regions ($x = L_{sep}$) are

$$-D_{eff,i,pos}\frac{\partial c_i}{\partial x}\bigg|_{x=(L_{sep}+L_{pos})^+} = -D_{eff,i,sep}\frac{\partial c_i}{\partial x}\bigg|_{x=(L_{sep}+L_{pos})^-}, \quad i = Li^+, Mn^{2+}, H^+, H_2O \qquad (2.37)$$

Cathode region ($x=L_{sep}$ to $x=L_{sep}+L_{pos}$): Mn-F and Mn-O compounds have been detected, using XPS, on the surface of $LiMn_2O_4$ positive electrodes [22]. The impedance of the electrolyte/electrode interface dramatically increased when a higher concentration of manganese was injected into the cell. It can be assumed that manganese ions from the electrolyte were additionally consumed during film formation. This can be described as:

$$\alpha EI + \alpha Mn^{2+} \rightarrow \alpha MnEI \tag{2.38}$$

Mn re-deposition is controlled by charge transfer reactions that follow the Tafel equation. This can be expressed as:

$$i_{Mn\_redep} = Fc_{Mn^{2+}} k_{Mn\_redep} \left[\exp(-\frac{\alpha_{Mn\_redep} F}{RT} (\phi_1 - \phi_2)) \right] \tag{2.39}$$

At the cathode region, the total applied current should be the sum of Li intercalation/deintercalation, manganese deposition, and hydrogen deposition, which can be described as:

$$i_{tot,cathode} = i_{Li^+,cathode} - \frac{S_{a\_oxid}}{S_{a\_pos}} i_{oxid} - i_{Mn\_redep} - FR_{Mn} \tag{2.40}$$

Material balance in the electrolyte phase at the cathode side can be used as

$$\frac{\partial\left(\varepsilon_2 c_{Li^+}\right)}{\partial t} = \nabla \cdot \left(D_{Li^+}^{eff} \nabla c_s\right) + \frac{1-t_+^0}{F} J^{Li} - \frac{\mathbf{i}_e \cdot \nabla t_+^0}{F} + S_{a\_pos} R_{decomp} \tag{2.41}$$

The individual material balance equations for H^+, Mn^{2+}, and H_2O in the cathode region are:

$$\varepsilon_2 \frac{\partial c_{H^+}}{\partial t} = \nabla \cdot (D_{eff,H^+} \nabla c_{H^+}) + S_{a\_oxid} R_{oxid} + 2R_{decomp} - 4S_{a\_pos} R_{Mn} \tag{2.42}$$

$$\varepsilon_2 \frac{\partial c_{Mn^{2+}}}{\partial t} = \nabla \cdot (D_{eff,Mn^{2+}} \nabla c_{Mn^{2+}}) + S_{a\_pos} R_{Mn} + \frac{1}{F} S_{a\_pos} i_{Mn\_redep} \tag{2.43}$$

$$\varepsilon_2 \frac{\partial c_{H_2O}}{\partial t} = \nabla \cdot (D_{eff,H_2O} \nabla c_{H_2O}) - R_{decomp} + 2S_{a\_pos} R_{Mn} \tag{2.44}$$

Boundary conditions for the material balance of species (Li^+, Mn^{2+}, H^+, H_2O) at the cathode side ($x = L_{sep} + L_{pos}$) are:

$$-D_{eff,i} \left.\frac{\partial c_i}{\partial x}\right|_{x=L_{sep}+L_{pos}} = 0, \quad i = Li^+, Mn^{2+}, H^+, H_2O \tag{2.45}$$

In the transport equation of the cathode part, it is assumed that the particles of active material are spheres. Thus, c_s is a concentration of solid phase and D_s is a diffusion coefficient of the solid phase. Material transport within the spherical particles in the cathode yields

$$\frac{\partial c_s}{\partial t}+\frac{1}{r^2}\nabla(r^2 D_s \nabla c_s)=0 \tag{2.46}$$

The boundary conditions for solid phase diffusion can be expressed as:

$$-D_s \left.\frac{\partial c_s}{\partial r}\right|_{r=0}=0 \tag{2.47}$$

$$-D_s \left.\frac{\partial c_s}{\partial r}\right|_{r=R_{pos}}=\frac{i_{n,pos}}{F} \tag{2.48}$$

Lithium intercalation/deintercalation reactions are governed by the Butler-Volmer equations:

$$i_{Li^+,cathode}=i_{0,Li^+}\left[\exp(\frac{\alpha_{a,Li}F}{RT}\eta_{Li^+})-\exp(\frac{\alpha_{c,Li}F}{RT}\eta_{Li^+})\right] \tag{2.49}$$

where i_{0,Li^+} is the exchange current of lithium intercalation/deintercalation reactions, defined as

$$i_{0,Li^+}=k_{Li^+}c_{s,surf}{}^{0.5}(c_{s,\max}-c_{s,surf})^{0.5}c_{Li^+}{}^{0.5} \tag{2.50}$$

where k_{Li^+} is the reaction rate constant in the positive electrode, $c_{s,\max}$ is the maximum concentration of lithium ion particles in the cathode electrode, and $c_{s,surf}$ is the surface concentration of lithium ions in the particle electrode.

Table 2 summarizes the side reaction parameters of the battery used in the simulations.

2.1.2.2 Degradation of cathode material.

2.1.2.2.1 Mn dissolution

All these side reaction mechanisms influence Mn dissolution, which in turn decreases the effective volume fraction of the solid phase, which can be expressed as

$$\frac{\partial \varepsilon_{pos}}{\partial t}=-S_{a\_pos}R_{Mn}V_{LMO} \tag{2.51}$$

where V_{LMO} is the molar volume of the active electrode material.

The rate constant for manganese dissolution is determined by using the measured surface area and the amount of manganese dissolved from the cathode material with time. Manganese dissolution is coupled with other side reactions and originates from several mechanisms, which makes it harder to estimate the exact reaction rate constant for manganese dissolution. Several assumptions were made to estimate the rate of manganese dissolution in order to calculate the reaction rate coefficient for manganese dissolution.

First, it is assumed that manganese ions are only dissolved by the acid attack described in equation(2.7). Although there are several mechanisms that cause manganese to dissolve into the electrolyte, the influence of the reaction on battery performance will be same. Second, using equation (2.8) and equation(2.43), the reaction constant for manganese dissolution can be determined by the surface area of the cathode electrode, the concentration of manganese ions, and the concentration of hydrogen ions. From the experiment results, the concentration of hydrogen ions (about 25 mM at the initial cycle) is higher than the concentration of manganese (about 1mM after 50 cycles). This means that the amount of dissolved manganese is only governed by the rate of manganese dissolution, and not by the concentration of H^+ ions. Thus, the concentration of hydrogen ions can be calculated using the concentration of manganese from equation(2.7), which can be measured by using ICP-OES.

The rate of manganese dissolution k_{Mn} was estimated using,

$$\varepsilon_2 \frac{\partial c_{Mn^{2+}}}{\partial t} = k_{Mn} c_{H^+} S_{a\_pos} \tag{2.52}$$

Because the amount of active material continuously decreases as the result of manganese dissolution, the maximum solid phase concentration also decreases proportional to the effective volume fraction decrease, which can be described as

$$c_{s,\max} = c_{s,\max 0} \frac{\varepsilon_{pos}}{\varepsilon_{pos0}} \tag{2.53}$$

2.1.2.2.2 Contact resistance

Contact resistance increases with cycling due to the formation of film on the cathode material and the re-deposited manganese compounds on the cathode surface.

η_{Li^+} is the overpotential for the lithium intercalation/deintercalation reaction, including the contact resistance increase, which causes ohmic drop of the system. This can be expressed as:

$$\eta_{Li^+} = \phi_s - \phi_e - U_{Li^+} - Fi_{Li^+} R_{contact} \tag{2.54}$$

where U_{Li^+} is the equilibrium potential of the lithium intercalation/deintercalation reactions

The influences of film resistance on the performance of the cell can also be found elsewhere in the cell [23-25]. By measuring the contact resistance of the electrode with pre-dissolved manganese (0, 50, 100, 150 and 200ppm), resistance information at an arbitrary concentration of manganese can be determined using linear interpolation.

2.1.2.2.3 Charge transfer resistance

The interfacial resistance change at the cathode/electrolyte interface resulting from manganese ions was also considered in the simulation using equation (2.55) [26-28]. The ability to transfer lithium ions at the electrode/electrolyte interface is decreased and the charge transfer reactions are slowed due to manganese ions. In order to evaluate the effect of manganese ions on cell performance, reaction rate constant changes are considered in the simulation. This requires measuring charge transfer resistance by using an experiment at the same voltage. As was the case with contact resistance, charge transfer resistance information with arbitrary concentration of manganese ions was acquired using experiment results.

$$R_{ct} = \frac{RT}{{n_e}^2 F^2 c_{\max} k_0 (M_{Li^+})^{0.5} (1-x)^{0.5} x^{0.5}} \tag{2.55}$$

In the classical equation (2.55), R is the gas constant, T is the temperature, n_e is the number of electrons exchanged, F is Faraday's constant, $c_{\max}$ is the maximum solid phase concentration, k_0 is a reaction rate constant and x is the intercalation level.

2.1.2.2.4 Diffusion coefficient

As manganese re-deposition occurs on the cathode surface, the effective diffusion coefficient decreases because the pores in the cathode material become clogging [2, 29, 30].

$$D_{Li^+}^{eff} = D_{Li^+}^{0}[1-\left(\frac{\varepsilon_{pos_0}-\varepsilon_{pos}}{\varepsilon_{pos_0}}\right)^{n_1}] \tag{2.56}$$

$D_{Li^+}^{0}$ is the initial diffusion coefficient measured using EIS method and n_1 is the adjustment factor for the diffusion coefficient of lithium ions in the electrolyte.

2.2 Results and Discussion

An outline of the current study, including experiments, simulations and the connection between them, is shown in Figure 2.2. The experiments were designed to understand the degradation of the cathode due to manganese ions and to provide input parameters for the simulations. By performing the simulations using a physics-based model and input parameters from experiments, comparisons between the output simulations and the results of experiments could be presented.

2.2.1 **Experimental results**

2.2.1.1 Conductivity measurements.

Table 2.3 shows the electronic conductivity measurements from $LiMn_2O_4$ composite electrode samples with different ratios of active material, carbon black and PVDF binder. The conductivities of these electrodes varied significantly among the samples. For example, the conductivity of sample 1 was more than 30 times greater than that of sample 8. Electrical resistivity hinders the flow of the electrons and also causes an ohmic drop in the system. Electrical resistance of the cell consists of the resistance of electrode particles, conductive additives, percolation networks in the electrode, current collectors, and the electrical tap [31]. The electronic conductivity of $LiMn_2O_4$ is about 0.2 $x10^{-6}$–$2x10^{-6}$; the conductivity of an overall composite electrode is highly dependent on the amount of carbon black in the sample [31-33]. Sample 5 was used in the experiments and simulations described in this work.

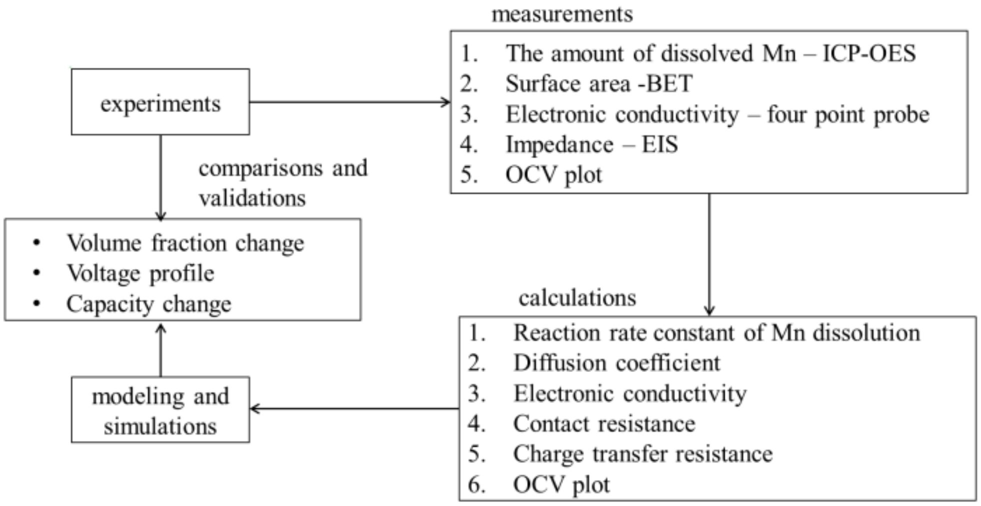

Figure 2.2 $LiMn_2O_4$/Li half-cell configurations of experiments and simulations

Sample	Ratio of Active material: Carbon Black :PVDF (CB:PVDF)	coating thickness(inch)	resistance(ohm*cm)	conductivity(S/m)
1	85:7.5:7.5 (1:1)	0.001	2.034	49.15 ±5.1
2	85:6.67:8.33 (0.8:1)	0.001	4.829	20.70 ±2.3
3	85:5.63:9.38 (0.6:1)	0.0012	6.879	14.53 ±1.1
4	85:4.29:10.71 (0.4:1)	0.001	42.18	2.370 ±0.2
5	90:5:5 (1:1)	0.0015	3.381	29.57 ±3.2
6	90:4.44:5.56 (0.8:1)	0.0007	10.20	9.802 ±0.9
7	90:3.75:6.25 (0.6:1)	0.003	25.39	3.937 ±0.4
8	90:2.86:7.14 (0.4:1)	0.001	67.70	1.477 ±0.2

Table 2.3 Conductivity measurements with different composition ratio of $LiMn_2O_4$ composite electrode samples

2.2.1.2 Surface area measurements.

Primary side reactions [1], such as electrolyte decomposition, SEI layer formation and manganese dissolution, originate primarily from reactions between the electrode and the electrolyte interface. The main influences on the intensity of these side reactions were the electrode area in contact with the electrolyte and the porosity of the composite electrode. For example, Marks et al. [34] measured the coulombic efficiency of two Li/graphite cells that contained 4 wt% and 7 wt% Super-S carbon black, respectively . The coulombic efficiency of the electrode containing the greater concentration of carbon had a more detrimental effect because SEI layer formation was boosted due to its higher surface area. In order to evaluate the precise intensities of various electrochemical reactions, the surface area of the $LiMn_2O_4$ composite electrode was determined using BET methods. Figure 2.3 (a) and (b) show the isotherms for the adsorption and the BET plot of the LiMn2O4 composite electrode, respectively. By calculating the slope and intercept from Figure 2.3(b), the surface area of the electrode could be determined using equation (2.1). The empirical constant C and the surface area of the $LiMn_2O_4$ electrode were 28.942 and 2.277 m2/g, respectively. Literature values for the $LiMn_2O_4$ particle surface vary from 1.5 to 3.0 m2/g [35, 36]. The results of our measurements lie within the range of those reported in previous literature.

(a)

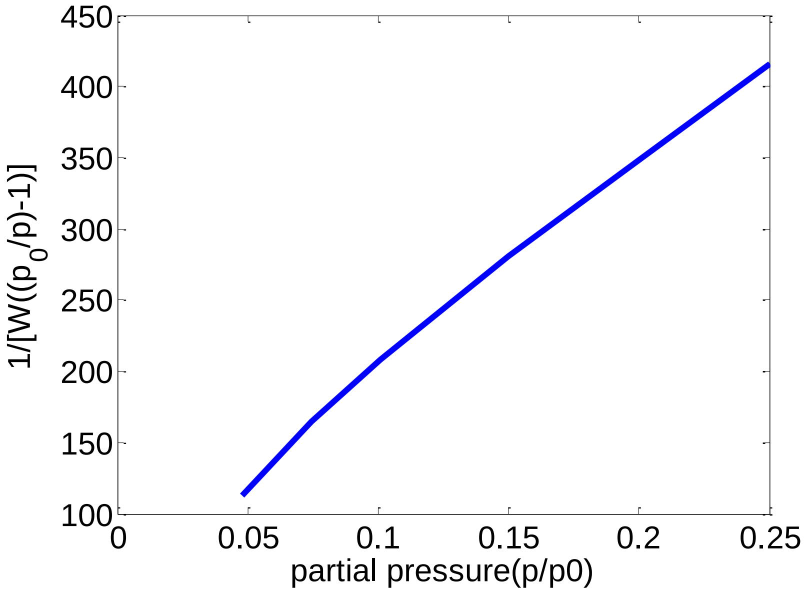

(b)

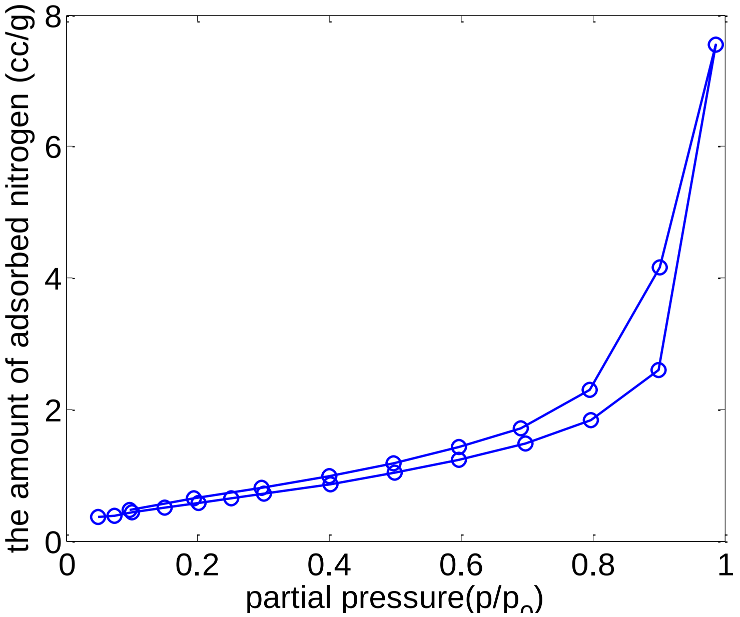

Figure 2.3 (a) Isotherms for the adsorption of nitrogen on $LiMn_2O_4$ composite electrode and (b) BET plot of $LiMn_2O_4$ composite electrode (partial pressure(p_0/p) versus 1/[W((p_0/p)-1]])

2.2.1.3 ICP-OES measurements.

Manganese dissolution is coupled with other side reactions, such as electrolyte oxidation. Manganese deposition onto both the cathode and anode degrades cell performance. Moreover, the amount of manganese dissolved from the $LiMn_2O_4$ spinel electrode is greatly affected by many other parameters, including temperature, operating voltage, electrolyte, salt, particle size and C-rate, which make the reaction even more complicated. To accurately predict the change in cell performance due to these side reactions, the precise amount of dissolved manganese must be determined.

To understand the effects of temperature, storage time, and particle size on manganese dissolution, the amount of manganese dissolved from the positive electrode was measured using ICP-OES. Table 2.4 shows the concentration of manganese dissolved from a $LiMn_2O_4$ composite electrode during storage in 1.0M $LiPF_6$ EC: DMC (1:1) electrolyte for 5, 10, 15 and 20 days at 0 ℃, room temperature, and 40 ℃. The results demonstrate that high temperature and extended storage time accelerate the dissolution process. For example, manganese in a porous electrode dissolved 2.6 times faster at 40 ℃ than at room temperature after 20 days.

Panels (a) and (b) in Figure 2.4 show the average concentration of manganese dissolved from a composite electrode and a powder particle electrode with different particle size, respectively, after storage for 7 days. Electrode particles of smaller size (less than 0.5μm) tend to dissolve more than electrode particles of larger size (less than 5μm) on both powder and composite electrodes. This is caused by the larger surface area exposed to the electrolyte that is attacking the cathode material. The concentration of manganese derived from the powder electrode was about 10 times higher than that derived from the composite electrode. The cathode surface area in contact with the electrolyte was larger for the powder electrode than for the composite electrode. Moreover, this may be happening, in part, because the PVDF used in the composite electrodes slows the dissolution reaction. The good adhesion to metallic collectors and the cohesion between active material particles achieved by the PVDF binder may reduce the surface area of active material in contact with the electrolyte, resulting in a decrease in the manganese dissolution effect.

Mn dissolution (ppm)	0 ℃	RT	40 ℃
1week	0.089	0.121	0.864
2week	0.158	0.163	3.26
3week	0.131	0.169	5.27
4week	0.133	0.229	7.87
5week	0.225	0.298	19.5

Table 2.4 The amount of dissolved manganese from $LiMn_2O_4$ composite electrode with time at different temperature (mM)

	15 cycle	30 cycle	50 cycle
Mn dissolution(mM)	0.178 ±0.05 (9.79ppm)	0.246±0.08 (13.53ppm)	1.016±0.21 (55.88ppm)

Table 2.5 Concentration of dissolved manganese from composite electrode in 1M $LiPF_6$ in EC:DMC (1:1) with different cycle number

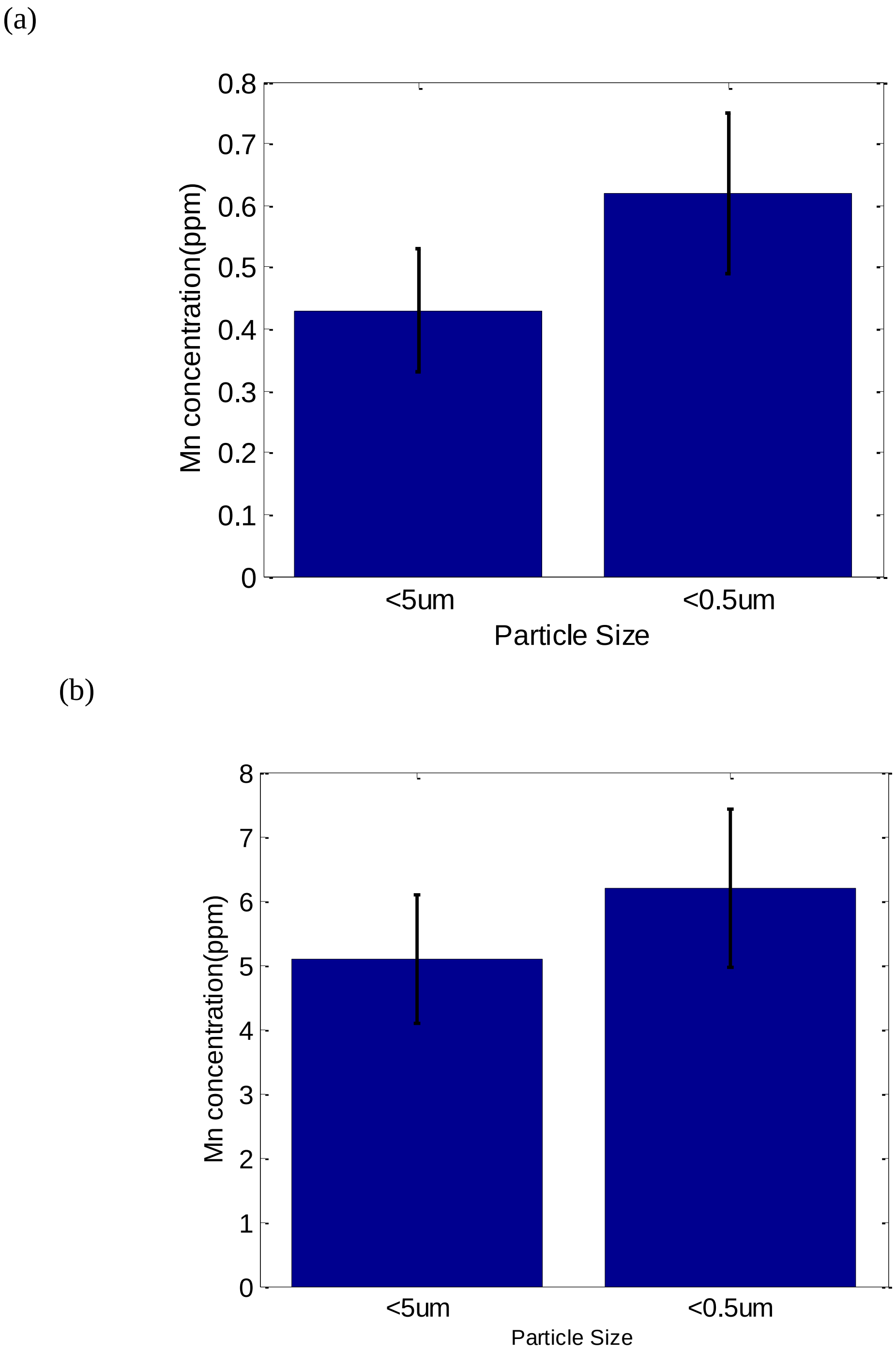

Figure 2.4 concentration of dissolved manganese after 7 days from (a) composite electrode and (b) powder particle in 1M $LiPF_6$ in EC:DMC (1:1) with different particle size

Table 2.5 shows the change in the concentration of dissolved manganese with different numbers of cycles. Three formation cycles were performed with C/10 before the actual cycles. Cycling the cell causes more manganese ions to dissolve from the $LiMn_2O_4$ electrode than does storing the electrode in electrolyte. For example, the amount of dissolved manganese resulting from storage in the electrolyte for 3 weeks was similar to the amount of dissolved manganese resulting from cycling for 30 hours. A previous study that used the rotating ring disk electrode (RRDE) method showed that 16.5 ppm (0.3 mM) of manganese dissolved after 50 cycles [37]. Another study reported that 60 ppm (1.092 mM) of the manganese dissolved after 55 cycles [38]. In this study, 1.016 mM of manganese dissolved after 50 cycle, which falls within the range observed in previous studies.

2.2.1.4 CV and EIS measurements.

Figure 2.5 (a) shows the results of CV measurement made with $LiMn_2O_4$ electrodes in electrolytes containing different concentrations of manganese. Increasing the concentration of dissolved manganese to 200 ppm caused a 5.37% decrease in the cathodic current peak of a $LiMn_2O_4$ electrode. The ability to transfer currents between electrolyte/electrode interfaces is decreased due to manganese ions. Moreover, it can be seen from Figure 2.5 (b) that the cathodic current peak shifts to the right when a higher concentration of manganese is included in the electrolyte. This shift indicates that the reaction rate constant is decreased and charge transfer resistance is increased due to manganese re-deposition. Figure 2.6 shows the EIS response with different voltages applied to the $LiMn_2O_4$ electrodes. By using EIS, we can separate the sources of impedance such as the electrolyte, the SEI layer, the interface, and diffusion through the $LiMn_2O_4$ electrodes. High-frequency resistance and charge-transfer resistance were separately plotted to see the different effects of voltages on both electrodes, as shown in Figure 2.7. High frequency resistance was similar throughout the range between 3.5 V and 4.3 V, whereas there was a change in charge-transfer resistance with different voltages. Changes in charge transfer resistance are due to the lithium concentration in the electrodes. The charge-transfer resistance (R_{ct}) versus voltage plot is supposed to perform according to the following classical equation [10]:

$$R_{ct} = \frac{1}{fFk_0 A c_O{}^{0.5} c_R{}^{0.5}} \tag{2.57}$$

where *f* denotes the usual electrochemical constant (equal to *F/RT*, where, *F* and *R* are the Faraday and gas constants, respectively, and *T* is the absolute temperature) and k_0 is the heterogeneous reaction rate constant. Also, the concentrations of the reduction-form, c_R, and that of the oxidation-form, c_O, are identified with the concentration of Li ions and unoccupied intercalation sites, respectively. From this equation, we can easily find that x = 0.5 has the minimum charge transfer resistance in $Li_xMn_2O_4$ electrode. From Fig 3, it is easy to find that the lowest R_{ct} in $Li_xMn_2O_4$ is 4.1V, when the electrode has intercalation level x = 0.5.

Figure 2.8 shows the EIS response of the $LiMn_2O_4$ electrodes to different concentrations of manganese ions in the electrolyte. High-frequency resistance and charge-transfer resistance were plotted separately to see the different impacts of manganese on the two electrodes, as shown in Figure 2.9. The contact resistance (high frequency resistance) of $LiMn_2O_4$ electrodes increased due to the additional layer formation induced by manganese re-deposition. Charge-transfer resistance also increased remarkably in $LiMn_2O_4$ electrodes due to the manganese ions in the electrolyte. The latter result is identical to the CV results displayed in Figure 2.5, which shows the decrease in reaction rate constant at higher concentrations of manganese in the electrolyte. This decrease is probably caused by Mn-F and Mn-O compounds, which are generated during the later stage of storage and are highly resistive. Their formation leads to cell polarization and hinders the charge transfer processes [22].

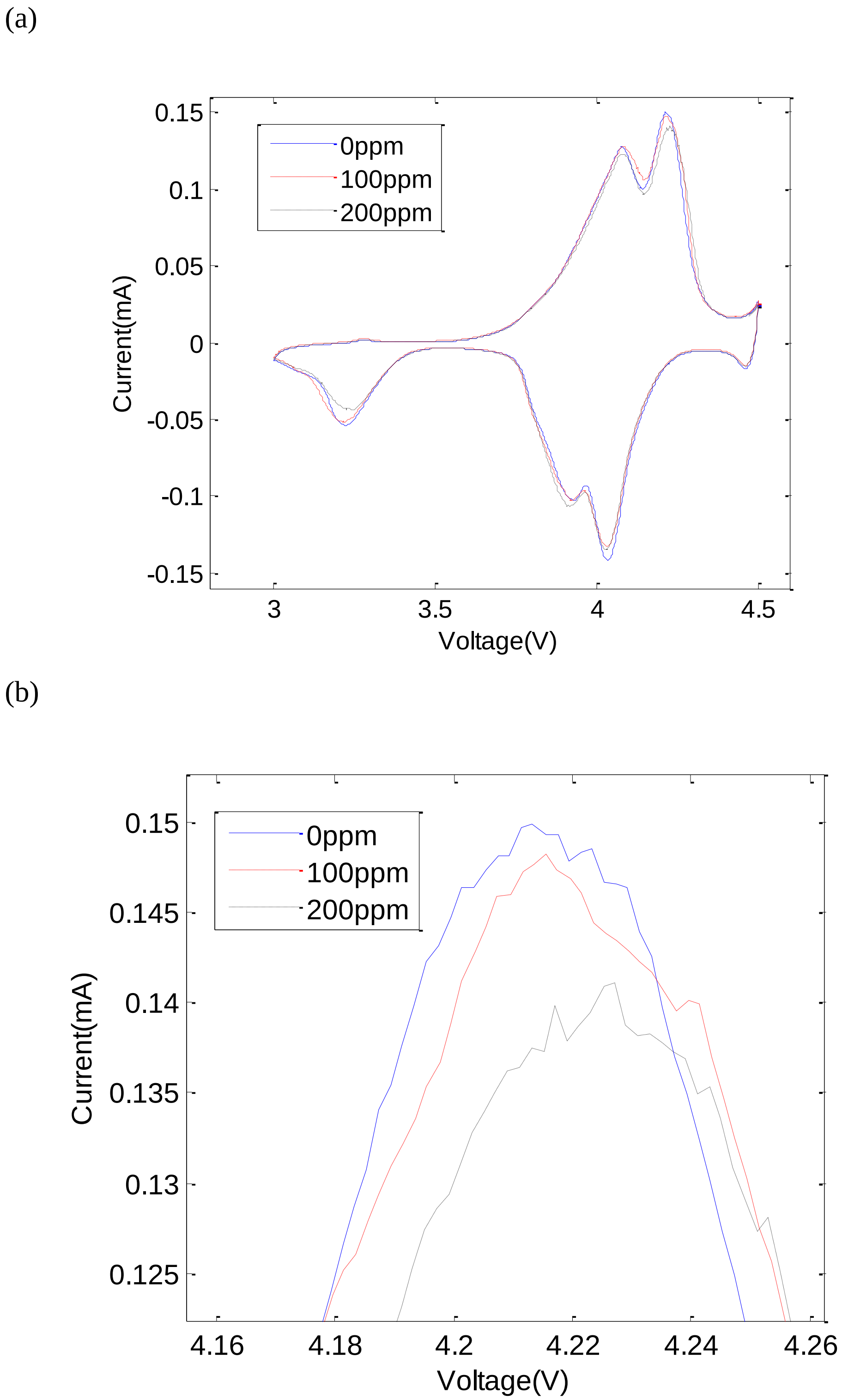

Figure 2.5 (a) CV results with different concentration of manganese in the electrolyte of $LiMn_2O_4$ electrodes and (b) magnification of the box from Figure 2.5(a)

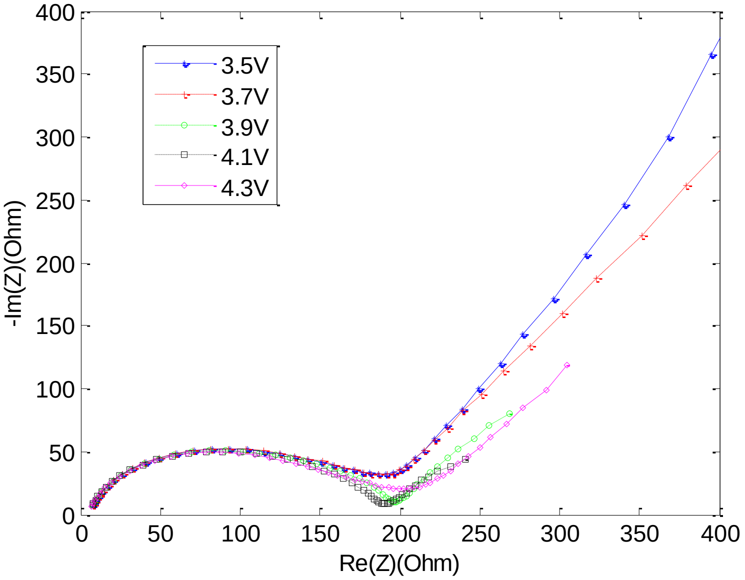

Figure 2.6 EIS response with different voltages of LMO electrodes

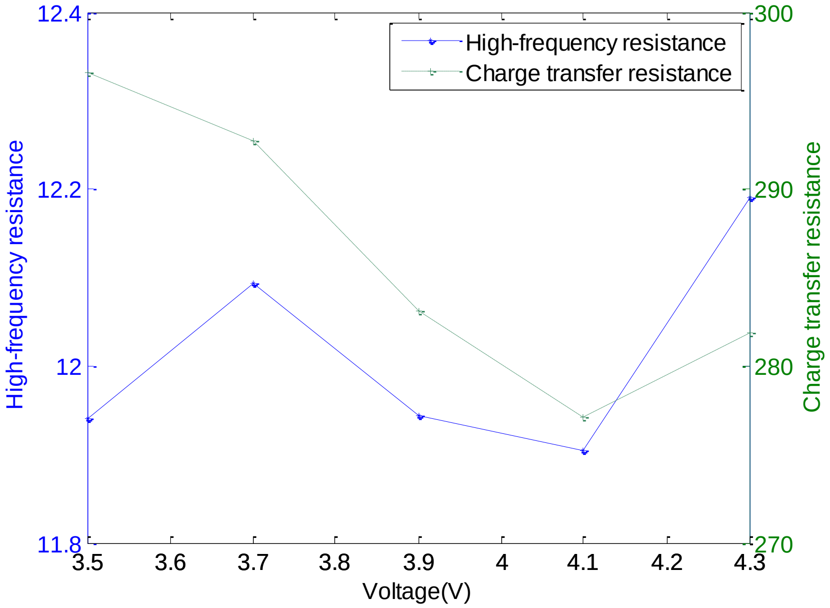

Figure 2.7 (a) High-frequency resistance change with respect to voltage (b) Charge-transfer resistance change with respect to voltage

The diffusion coefficient of $LiMn_2O_4$ was measured as a function of voltage using an EIS method as shown in Figure 2.10. The value of the diffusion coefficient of $LiMn_2O_4$ electrode varied from 10^{-8} to 10^{-12}, depending on the measurement technique and the experimental conditions [31]. Since the diffusion coefficient dramatically changes under various conditions, it is important to measure the exact value to compare between experiments and simulations. A minimum value of the diffusion coefficient is observed near the 4.1 V region, which has the highest current peak in the CV results shown in Figure 2.5 and where a voltage plateau is found in Figure 2.13. To decrease the voltage near 4.1 V, more lithium would be needed to increase the state of charge (SOC) of the electrode. This is the reason why the 4.1 V region has the minimum diffusion coefficient throughout the voltage range. For the simplicity, the average value of the diffusion coefficient was used as input to the simulation.

The diffusion coefficients of $LiMn_2O_4$ electrodes were also measured after inserting the desired concentration of manganese in the electrolyte, as shown in Figure 2.11 and Table 2.6. Manganese ions in the electrolyte substantially decrease the diffusion of lithium into the electrode. After adding manganese (200 ppm) to the electrolyte, the diffusion coefficient dropped from 1.3×10^{-12} m^2/s to 4×10^{-13} m^2/s. Dissolved manganese and electrolyte decomposition products, like the contact resistance and charge transfer resistance increase, generate additional inactive film growth, which also blocks Li-ion transport to the electrode.

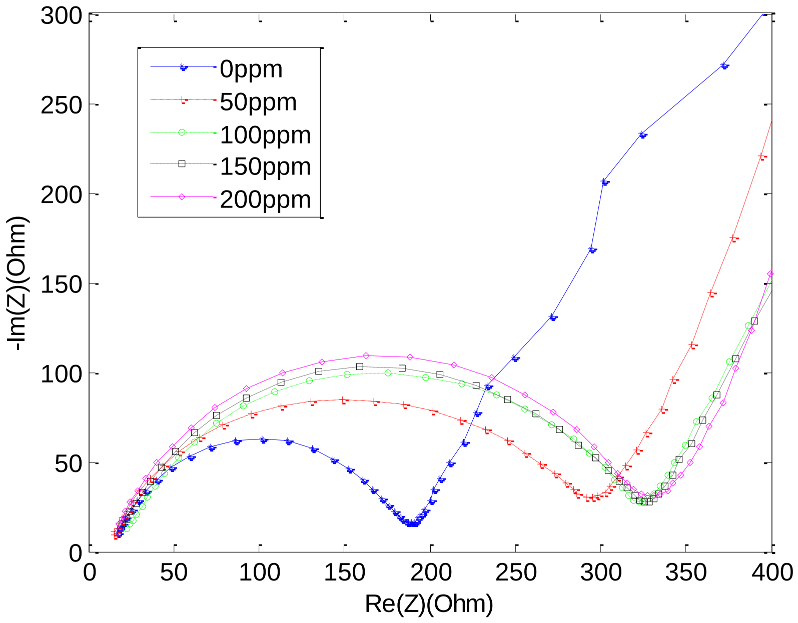

Figure 2.8 EIS response with different concentrations of manganese of LMO electrodes

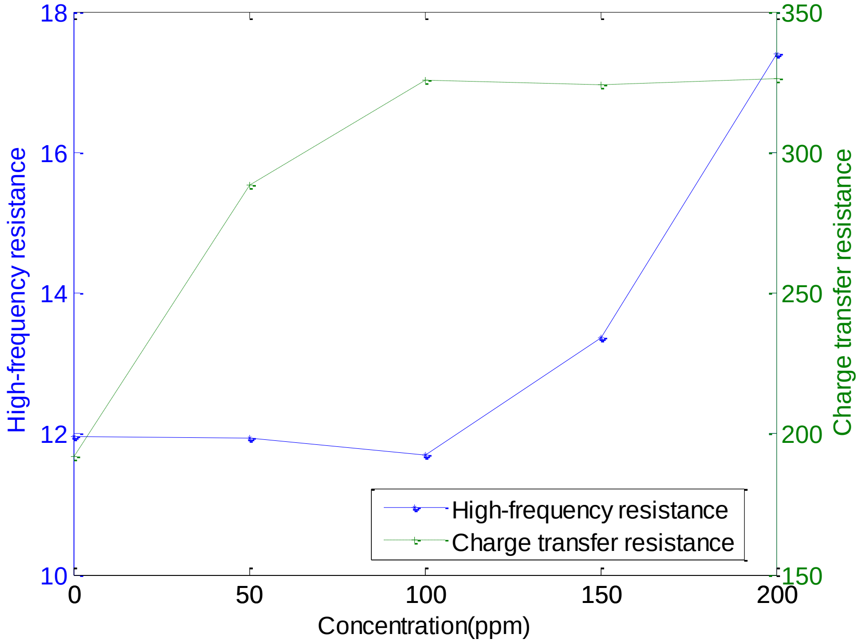

Figure 2.9 Impedance change at different concentrations in (a) high-frequency resistance region and (b) charge-transfer resistance region

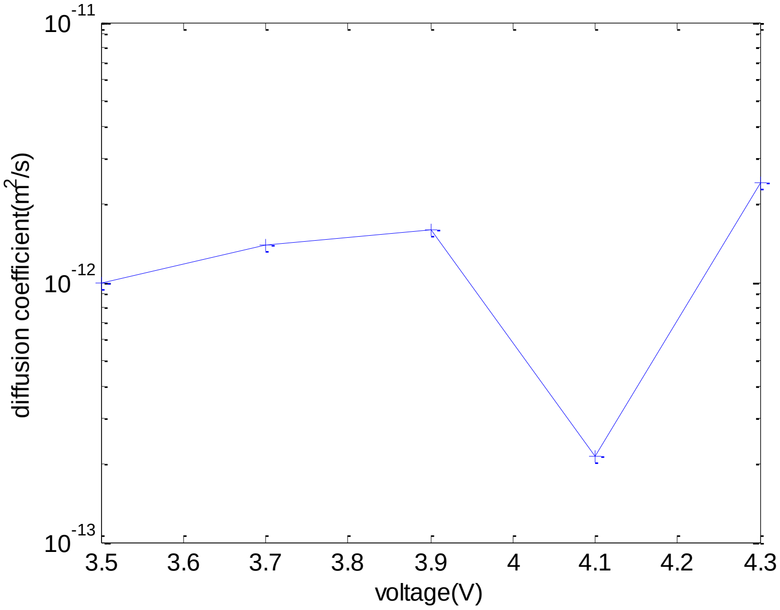

Figure 2.10 Diffusion coefficient change with different voltage of $LiMn_2O_4$ electrodes measured using EIS method

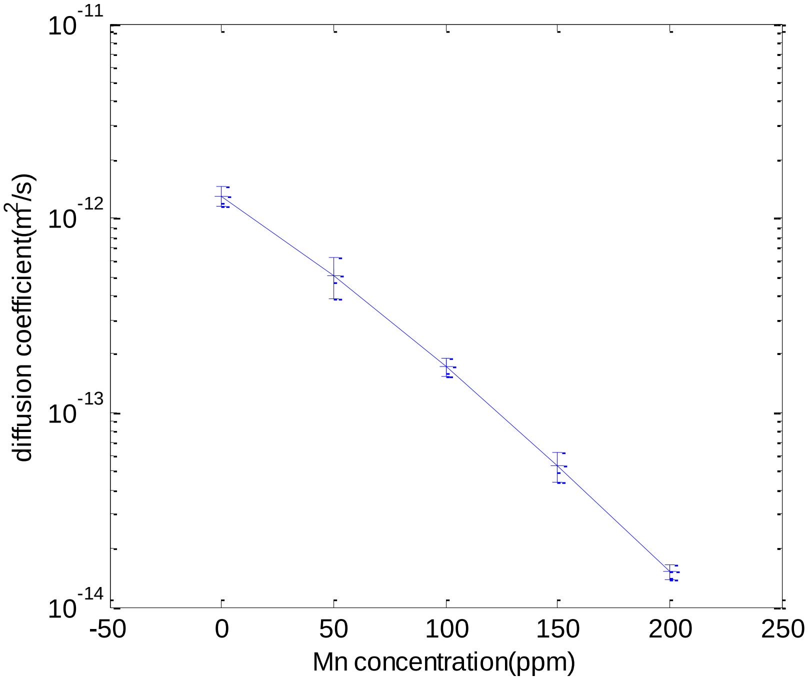

Figure 2.11 Diffusion coefficient change with different concentration of manganese in the electrolyte measured using EIS method

2.2.1.5 Capacity measurements

The change in $LiMn_2O_4$ electrode capacity with cycle number in the presence of different concentrations of manganese is shown in Figure 2.12. However, the discharge capacity of the $LiMn_2O_4$ electrode decreased continuously during the cycles. It was obvious that higher concentrations of manganese caused greater capacity decreases. The $LiMn_2O_4$ electrode capacity decreased significantly, up to 15 % in 16 cycles, due to dissolved Mn ions. Presumably, the deposition of manganese and electrolyte decomposition products on the electrode surface hinders the lithiation/delithiation process during cycling, which affects the unceasing decline of the discharge capacity of the cell. Moreover, the capacity of the cells kept decreasing as the cycle number increased, which means that a passive cathode film layer was not fully established on the $LiMn_2O_4$ surface. The cathode electrolyte interface layer is relatively thin compared with the SEI layer of a graphite electrode, which lacks a passivation effect. However, an additional capacity decrease was observed with an increase in the concentration of dissolved manganese ions. The low electronic conductivity of the manganese compounds formed on the cathode surface might be one reason for this lack of passivation effect. It is suggested that manganese ions dissolved from the cathode continuously form manganese compounds on the cathode surface. These manganese compounds hinder charge transfer reactions and the diffusion of the lithium ions, resulting in a continuous capacity fade. This result is similar to those of previous studies performed by adding manganese additives to a graphite anode. These studies also showed a continuous decrease in the capacity of the negative electrode [39]. Lithium reversibility in the graphite was found to be degraded by adding just a small amount of manganese. These reactions, in addition to active loss of the cathode material, will also contribute to capacity fade.

Mn concentration (ppm)	Diffusion coefficient (m^2/s)
0	$1.31\times10^{-12} \pm1.5\times10^{-13}$
50	$5.05 \times10^{-13} \pm1.2\times10^{-13}$
100	$1.72 \times10^{-14} \pm1.81\times10^{-14}$
150	$5.31 \times10^{-14} \pm0.91\times10^{-14}$
200	$1.51 \times10^{-14} \pm1.41\times10^{-15}$

Table 2.6 Diffusion coefficient change with different concentration of manganese in the electrolyte measured using EIS method

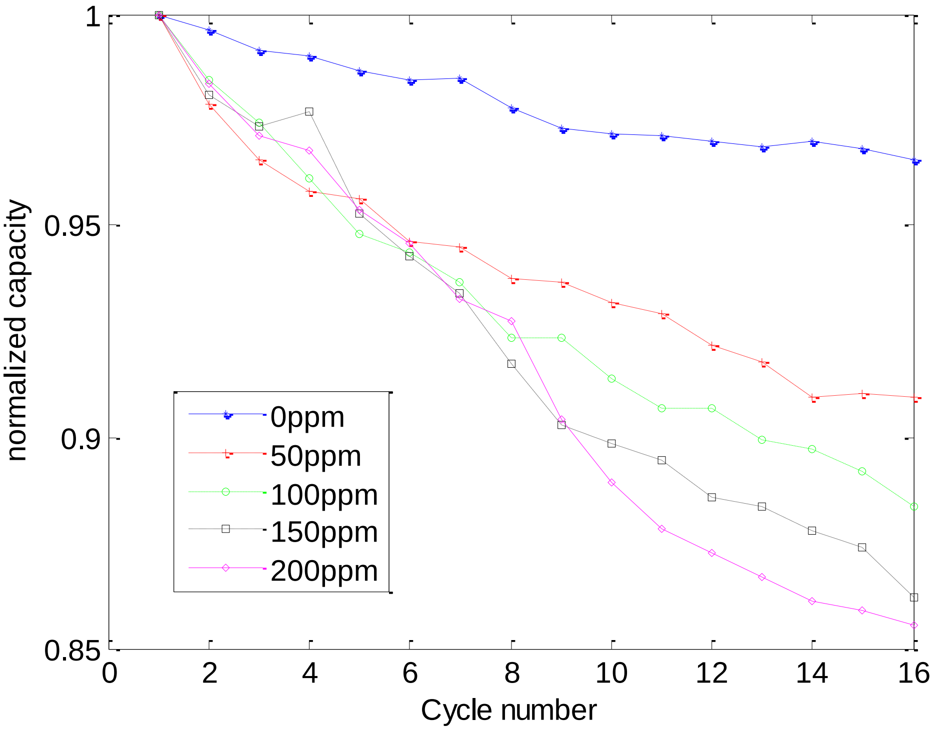

Figure 2.12 Capacity change with cycle number of $LiMn_2O_4$ electrodes with different concentrations of manganese

2.2.2 **Simulation results.**

Figure 2.13 shows a comparison of the voltage profiles obtained by experiment and simulation. The experimentally measured OCV curve was used as the input in the simulation. A black line shows the voltage profile output using the OCV curve from a previous study and the red line shows the voltage profile predicted by simulations using the measured OCV [40]. The output voltage profile obtained in the simulations using the measured OCV curve (red line) matches the experimental result (blue circles) seamlessly (Figure 2.13). Qualitative differences between the experiments and the reference arise mainly from the 4.1 V plateau during discharge. The experimental OCV curve shows a voltage drop near 4.1 V, compared with the reference, mainly due to the impedance of the cell. In order to include cell impedance information and predict cell performance more accurately, measured OCV curve is used in the simulation.

The effective volume fraction of the active material changes continuously due to the dissolution of manganese. A 4% reduction in the volume fraction of active material after 50 cycles was predicted by using a calculated reaction rate constant for manganese dissolution, as shown in Figure 2.14. Similarly, the change in volume fraction of the active material from the experiment was calculated using equation (2.5), and then the amount of manganese ions dissolved in the electrolyte was measured using ICP-OES. The results of the experiments and the simulations show similar trends. Previous manganese dissolution experiments based on sample weights from a powder electrode showed 3.2% Mn dissolution [13]. Larger amounts of manganese dissolution seen in previous studies probably resulted from the use of powder electrodes, whereas a composite electrode was used for the experimental work in this study. As the cycle number increases, the volume fraction of the active material decreases and the amount of dissolve manganese ions increases. The acceleration of these reactions results primarily from solvent oxidation, along with the generation of H_2O molecules due to the acid attack shown in equation (2.7). While hydrogen ions are generated through solvent oxidation, they also react with $LiMn_2O_4$ electrodes and generate H_2O molecules that constantly regenerate HF according to equation (2.14). These reactive species will continuously attack the active materials and are critical to the decrease in cell capacity.

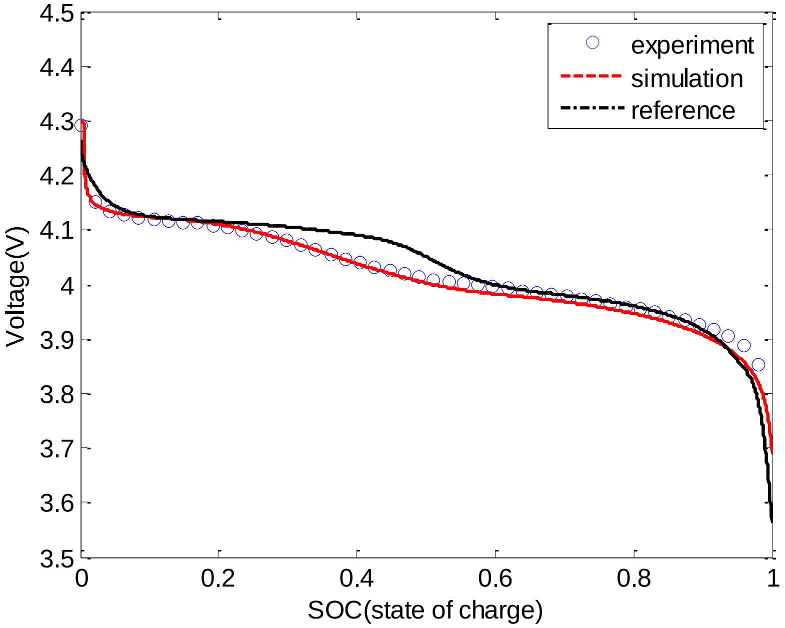

Figure 2.13 Open Circuit Voltage profile comparisons of experiment and simulations

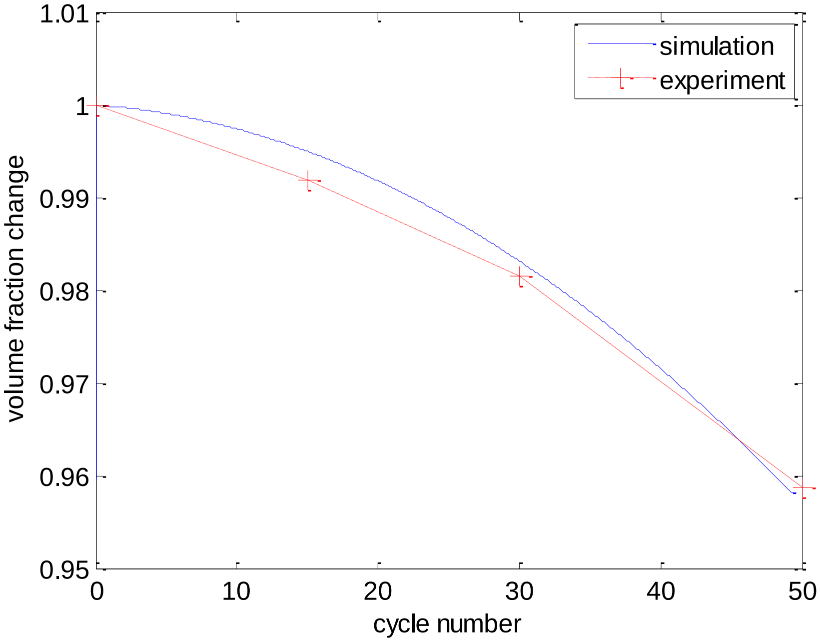

Figure 2.14 Volume fraction change of $LiMn_2O_4$ electrode with cycle number due to manganese dissolution

Figure 2.15 shows the changes in diffusion coefficient and reaction rate coefficient that result from cathode degradation. The decreases in the diffusion coefficient and the reaction rate coefficient are critical factors in the decrease in electrode capacity, especially during fast cycling. The Li-ion diffusion coefficient decreased from 1.3 x 10^{-12} m^2/s to 4 x 10^{-13} m^2/s after 50 cycles. Current experimental results showed that the lithium ion diffusion coefficient changes with changes in the voltage and manganese concentration (Figure 2.10 and Figure 2.11, respectively). The change in the lithium ion diffusion coefficient due to voltage is neglected in this work, for simplicity. The ICP results showed that approximately 55 ppm (1.016 mM) of manganese dissolved after 50 cycles. The diffusion coefficient, measured using the EIS method, decreased to 5.05×10^{-13} m^2/s after adding 50 ppm of manganese to the electrolyte. The experiments and simulations yield similar predictions for the diffusion coefficient after 50 cycles. Similar experiments have also been conducted by other research groups, using EIS methods [41-43]. One previous study [42] revealed that the diffusion coefficient of a fresh Li-ion electrode decrease from the range of (1–6) × 10^{-12} cm^2/s to 0.47 × 10^{-13} cm^2/s after repeated charge-discharge cycling. It was suggested that a passive layer forms on the electrode and clogs the pores of the lithium ion path, and continuously reduces the lithium ion diffusion coefficient.

Simulation results (Figure 15) also show that the reaction rate coefficient decreased linearly, from 2.0 × 10^{-10} m/s to 1.465 × 10^{-10} m/s, after 50 cycles. Previous experimental and simulation studies have revealed a linear relationship between resistance and cycle number. Impedance measurements from a previous study [17] showed a linear increment of contact and electrode reaction resistance. It can be argued that a change in contact area between oxide and carbon particles resulting from Mn dissolution is the main reason for the resistance increase. Park et al. [7] also predicted a linear increase in relative resistance with cycle number due to the manganese disproportion reaction. One of main reasons for the increase in resistance comes from the loss of contact between spinel particles and the carbon conductor as the spinel dissolves into the electrolyte.

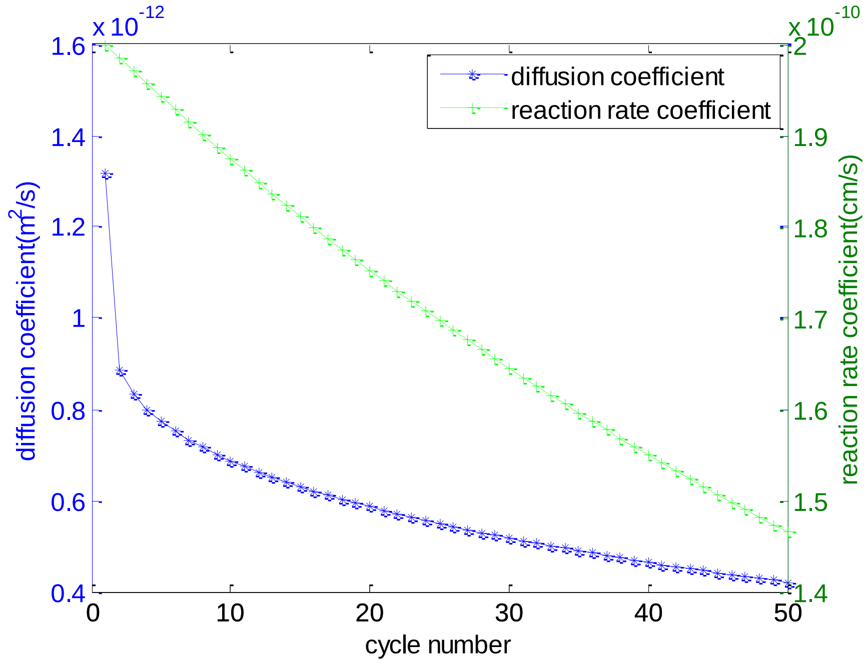

Figure 2.15 Diffusion coefficient and reaction rate coefficient change due to cycling

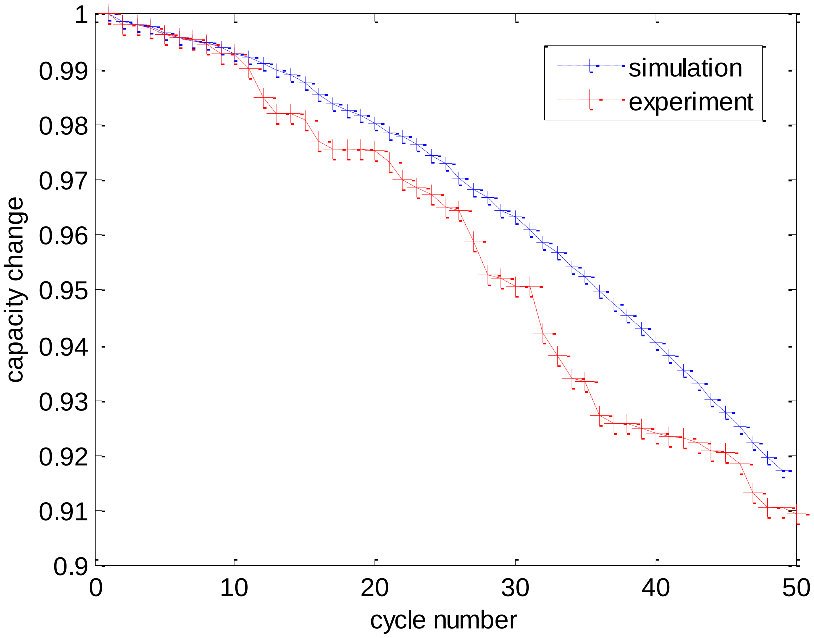

Figure 2.16 Comparison of capacity change with cycle number of $LiMn_2O_4$ electrodes between experiments and simulations.

The current impedance and CV study reveal an increase in contact resistance, an increase in charge transfer increase, and a decrease in the reaction rate coefficient of the cell due to an increase in the concentration of manganese ions in the electrolyte. It is proposed that the growth of electrochemically generated inactive material on the surface of the cathode material was increased due to dissolved manganese ions. The growth of film on the cathode surface results in an increase in the contact resistance and charge transfer resistance of the cell, as well as a decrease in lithium diffusivity. Previous spectroscopic results, which showed that the active material particles are covered by pristine surface films comprised primarily of Li_2CO_3 at initial cycles, can explain these phenomena [35]. After repeated cycling of the cell, the electrode impedance will increase further due to the precipitation of LiF, which is derived from HF, on the surface. Additionally, Mn-F compounds generated at a later stage of storage due to manganese ions in the electrolyte aggravate electrode performance even more, by increasing resistance that leads to cell polarization [22].

Figure 2.16 shows comparisons between experiments and simulations of the change in capacity with cycle number. In the experiments, 5 formation cycles with C/10 were performed before the actual cycles. In both simulations and experiments, the cells were cycled between 3.5 V and 4.3 V with C/5 rate for 50 cycles. The experimental results showed approximately 8.3% capacity loss. The results of the simulation show about 9.0 % capacity loss after 50 cycles, due to side reactions induced by degradation mechanisms and electrode degradation. Capacity loss resulting from the loss of active material due to the side reaction mechanisms shown in Figure 2.14 is only 4%. This indicates that active material loss due to manganese dissolution and other side reactions is responsible for only 4% of the decrease in cell capacity. Degradations of electrode performance, such as contact resistance increase, charge transfer resistance increase, and diffusion coefficient decrease, are also major causes of the decrease in capacity.

There have been many studies using experiments and simulations that describe decreases in the capacity of $LiMn_2O_4$ spinel electrodes under different conditions, such as temperature, cycle number, voltage range, preparation method, calcination temperature and surface area [2, 9, 44-49]. The range of these capacity decreases also changes dramatically, depending on the various conditions. Previous literature has shown 10.7 % [50], 11.03 % [51] and 12 % [48] decreases in capacity measured after 50 cycles with C/2 rate. The results of our study show an approximately 9 % decrease in capacity with a C/5 rate, which is similar to the results of previous research. The differences in C-rate between the current and previous experiments might be the primary reason for the differences in capacity decrease. Dai et al. [2] predicted a 16% decrease in capacity after 50 cycles between 3.5 V and 4.3 V, at 55 ℃, with a C/3 rate, using a physics-based model. By considering the fact that higher temperature, higher C-rate and wider voltage range accelerate capacity fade, our simulation results also show reasonable values.

The relatively slow C-rate used in this work results in a higher manganese dissolution rate. Moreover, the lower C-rate also caused a smaller capacity loss due to changes in the contact resistance, diffusion coefficient, and reaction rate coefficient. Simulation results showed that an approximately 5% loss in capacity occurred during 50 cycles as a result of changes in contact resistance, diffusion coefficient and reaction rate coefficient. However, the impact of electrode degradation on capacity will increase and active material loss due to degradation reactions will decrease when the C-rate increases. Cathode degradation that originates from diffusion coefficient decrease, reaction rate constant decrease and contact resistance will be quantitatively more responsible for the decrease in the capacity of the electrode when C-rate is higher.

2.3 Conclusions

A series of $LiMn_2O_4$ composite electrode degradations and their impact on cell performance were investigated in this study, which features unique improvements in both experiments and simulations. Specifically, our study focused on cathode degradation in the cell. It included parameter changes of the cathode electrode due to manganese ions, along with key input parameters measured using different analytical techniques. It also featured an improved electrochemical model that considered both side reaction mechanisms and degradations of the electrode.

Electrochemical measurements were conducted by using a lithium/$LiMn_2O_4$ half-cell with electrolyte containing different concentrations of manganese in order to elucidate the impact of dissolved manganese on the cathode electrode. Based on the CV, EIS and cycling results, it was observed that manganese ions negatively impact the cathode through re-deposition. For instance, the capacity of a $LiMn_2O_4$ composite electrode decreased up to 15 % after 16 cycles in the presence of a 200 ppm concentration of Mn-ions dissolved in the electrolyte.

Key parameters related to battery cell performance, including surface area, electronic conductivity, impedance, and the amount of manganese dissolution, were directly measured using numerous analytical techniques. For instance, it was experimentally observed that a 1.016 mM (60 ppm) concentration of manganese dissolved into the electrolyte after 50 cycles. By using previous findings, the contact resistance increase of the cell, the decrease in diffusion ability due to clogging of the porous structure, and the decrease in reaction rate constant due to manganese ions were also calculated and used as inputs into our simulations.

The experimental findings from the current study suggest that both manganese dissolution and its subsequent impact on cathode degradation should be considered in order to fully account for battery performance. A physics-based, side-reaction coupled electrochemical model with key input parameters was used to explain the magnitude and mechanisms of electrode degradation. The simulations and experiments showed that active material decreased 4% and capacity decreased 9 % after 50 cycles due to side reactions. This result indicates that an approximately 5% loss in capacity occurred during 50 cycles as a result of changes in contact resistance, diffusion coefficient and reaction rate coefficient due to Mn ions in the electrolyte. In conclusion, the current study suggests that both active material loss due to degradation mechanisms and parameter changes due to degradation of the electrode critically influence cell performance.

2.4 Appendix

2.4.1 **Four point probe method – Electronic conductivity measurements**

Potential differences were measured from the inner two probes and the current was supplied and extracted from the outer two probes. The electronic conductivity of the composite electrode was calculated [52] as

$$\kappa_s^{eff} = \frac{\ln(2)}{\pi t_e}\left(\frac{I}{E}\right) = \frac{0.221}{t_e}\left(\frac{I}{E}\right) \tag{2.58}$$

where t_e is the electrode thickness, κ_s^{eff} is the electronic conductivity of the electrode, I is the applied current and E is the electric potential difference between two probes.

2.4.2 **BET method – Surface area measurements**

BET theory describes the multilayer physical adsorption of gas molecules on a solid surface by considering Langmuir adsorption and condensation of gas onto liquid. In the first layer, BET theory uses Langmuir adsorption to describe the equilibrium adsorption of a gas monolayer onto a solid surface. Second and further layers are adsorbed by condensation of the gas onto the liquid phase as a function of pressure.

The fraction of occupied surface θ, which can be defined as the ratio of the number of gas molecules adsorbed on the surface to the number of adsorbed molecules required to completely cover the solid with a layer, can be expressed as:

$$\theta = \frac{N}{N_m} = \frac{C(p/p_0)}{(1-p/p_0)[1-p/p_0+C(p/p_0)]} \tag{2.59}$$

where N is the number of gas molecules adsorbed on the surface, N_m is the number of adsorbed molecules required to cover the solid with a layer, C is empirical constant, p is the applied pressure and p_0 is the saturation pressure.

The mass of gas adsorbate required to cover the solid with a layer and the empirical constant C were determined by plotting:

$$\frac{1}{W[p/p_0-1]}=\frac{1}{W_mC}+\frac{C-1}{W_mC}(\frac{p}{p_0}) \tag{2.60}$$

where W is the mass of gas molecules adsorbed onto the surface and W_m is the number of adsorbed molecules required to cover the solid with a layer of adsorbed molecules.

The surface area of the porous electrode was determined by:

$$SA=\frac{W_mN_AA_X}{M_A} \tag{2.61}$$

where N_A is the Avogadro constant, A_x is the cross-sectional area of the adsorbed molecule and M_A is the molar mass of the adsorbed molecule.

BIBLIOGRAPHY

[1] P. Arora, R.E. White, M. Doyle, Journal of The Electrochemical Society, 145 (1998) 3647-3667.

[2] Y. Dai, L. Cai, R.E. White, Journal of The Electrochemical Society, 160 (2013) A182-A190.

[3] D. Zhang, B.S. Haran, A. Durairajan, R.E. White, Y. Podrazhansky, B.N. Popov, Journal of Power Sources, 91 (2000) 122-129.

[4] J. Vetter, P. Novak, M.R. Wagner, C. Veit, K.C. Möller, J.O. Besenhard, M. Winter, M. Wohlfahrt-Mehrens, C. Vogler, A. Hammouche, Journal of power sources, 147 (2005) 269-281.

[5] J. Shim, R. Kostecki, T. Richardson, X. Song, K.A. Striebel, Journal of Power Sources, 112 (2002) 222-230.

[6] L. Yang, M. Takahashi, B. Wang, Electrochimica Acta, 51 (2006) 3228-3234.

[7] J. Park, J.H. Seo, G. Plett, W. Lu, A.M. Sastry, Electrochemical and Solid-State Letters, 14 (2011) A14-A18.

[8] C.-H. Lu, S.-W. Lin, Journal of materials research, 17 (2002) 1476-1481.

[9] X. Lin, J. Park, L. Liu, Y. Lee, A.M. Sastry, W. Lu, Journal of The Electrochemical Society, 160 (2013) A1701-A1710.

[10] B.J. Johnson, D.H. Doughty, J.A. Voigt, T.J. Boyle, Journal of Power Sources, 68 (1997) 634-636.

[11] R.J. Gummow, A. de Kock, M.M. Thackeray, Solid State Ionics, 69 (1994) 59-67.

[12] Y. Xia, M. Yoshio, Journal of The Electrochemical Society, 143 (1996) 825-833.

[13] W. Choi, A. Manthiram, Journal of The Electrochemical Society, 153 (2006) A1760-A1764.

[14] E. Wang, D. Ofer, W. Bowden, N. Iltchev, R. Moses, K. Brandt, Journal of The Electrochemical Society, 147 (2000) 4023-4028.

[15] A. Du Pasquier, A. Blyr, P. Courjal, D. Larcher, G. Amatucci, B. Gérand, J.M. Tarascon, Journal of The Electrochemical Society, 146 (1999) 428-436.

[16] R. Benedek, M.M. Thackeray, Electrochemical and Solid-State Letters, 9 (2006) A265-A267.

[17] D.H. Jang, Y.J. Shin, S.M. Oh, Journal of The Electrochemical Society, 143 (1996) 2204-2211.

[18] D.H. Jang, S.M. Oh, Journal of The Electrochemical Society, 144 (1997) 3342-3348.

[19] R. Darling, J. Newman, Journal of The Electrochemical Society, 145 (1998) 990-998.

[20] C.G. Barlowz, Electrochemical and Solid-State Letters, 2 (1999) 362-364.

[21] T. Kawamura, S. Okada, J.-i. Yamaki, Journal of Power Sources, 156 (2006) 547-554.

[22] D. Kim, S. Park, O.B. Chae, J.H. Ryu, Y.-U. Kim, R.-Z. Yin, S.M. Oh, Journal of The Electrochemical Society, 159 (2012) A193-A197.

[23] P. Ramadass, B. Haran, R. White, B.N. Popov, Journal of Power Sources, 123 (2003) 230-240.

[24] P. Arora, M. Doyle, R.E. White, Journal of The Electrochemical Society, 146 (1999) 3543-3553.

[25] W. Fang, O.J. Kwon, C.-Y. Wang, International Journal of Energy Research, 34 (2010) 107-115.

[26] M.D. Levi, K. Gamolsky, D. Aurbach, U. Heider, R. Oesten, Electrochimica Acta, 45 (2000) 1781-1789.

[27] Q.-c. Zhuang, X.-y. Fan, J.-m. Xu, G.-z. Wei, Q.-f. Dong, S.-g. Sun, Chemical Research in Chinese Universities, 24 (2008) 511-515.

[28] Q.-C. Zhuang, S. Xu, X. Qiu, Y. Cui, L. Fang, S. Sun, 孙世刚, Prog. Chem, 22 (2010) 1044.

[29] G. Sikha, B.N. Popov, R.E. White, Journal of The Electrochemical Society, 151 (2004) A1104-A1114.

[30] J.F. Yan, T.V. Nguyen, R.E. White, R.B. Griffin, Journal of The Electrochemical Society, 140 (1993) 733-742.

[31] M. Park, X. Zhang, M. Chung, G.B. Less, A.M. Sastry, Journal of Power Sources, 195 (2010) 7904-7929.

[32] J. Molenda, W. Kucza, Solid State Ionics, 117 (1999) 41-46.

[33] J. Marzec, K. Świerczek, J. Przewoźnik, J. Molenda, D.R. Simon, E.M. Kelder, J. Schoonman, Solid State Ionics, 146 (2002) 225-237.

[34] T. Marks, S. Trussler, A.J. Smith, D. Xiong, J.R. Dahn, Journal of The Electrochemical Society, 158 (2011) A51-A57.

[35] D. Aurbach, K. Gamolsky, B. Markovsky, G. Salitra, Y. Gofer, U. Heider, R. Oesten, M. Schmidt, Journal of The Electrochemical Society, 147 (2000) 1322-1331.

[36] T. Eriksson, (2001).

[37] L.-F. Wang, C.-C. Ou, K.A. Striebel, J.-S. Chen, Journal of The Electrochemical Society, 150 (2003) A905-A911.

[38] S. Lim, J. Cho, Electrochemistry Communications, 10 (2008) 1478-1481.

[39] S. Komaba, N. Kumagai, Y. Kataoka, Electrochimica acta, 47 (2002) 1229-1239.

[40] M. Doyle, J. Newman, A.S. Gozdz, C.N. Schmutz, J.M. Tarascon, Journal of The Electrochemical Society, 143 (1996) 1890-1903.

[41] D. Zhang, B.N. Popov, R.E. White, Journal of Power Sources, 76 (1998) 81-90.

[42] S.R. Das, S.B. Majumder, R.S. Katiyar, Journal of Power Sources, 139 (2005) 261-268.

[43] K.A. Striebel, A. Rougier, C.R. Horne, R.P. Reade, E.J. Cairns, Journal of The Electrochemical Society, 146 (1999) 4339-4347.

[44] Y.-K. Sun, I.-H. Oh, K.Y. Kim, Industrial & Engineering Chemistry Research, 36 (1997) 4839-4846.

[45] Y. Xia, N. Kumada, M. Yoshio, Journal of Power Sources, 90 (2000) 135-138.

[46] Y. Xia, Y. Zhou, M. Yoshio, Journal of The Electrochemical Society, 144 (1997) 2593-2600.

[47] X. Xiao, J. Lu, Y. Li, Nano Research, 3 (2010) 733-737.

[48] C.-h. Doh, J.-h. Lee, D. Lee, B.-s. Jin, S.-i. Moon, (2009).

[49] M.Y. Song, D.S. Ahn, H.R. Park, Journal of Power Sources, 83 (1999) 57-60.

[50] L. Xiong, Y. Xu, C. Zhang, Z. Zhang, J. Li, Journal of Solid State Electrochemistry, 15 (2011) 1263-1269.

[51] Y.-K. Sun, S.-H. Jin, Journal of Materials Chemistry, 8 (1998) 2399-2404.

[52] F.M. Smits, Bell System Technical Journal, 37 (1958) 711-718.

CHAPTER 3

SIDE REACTIONS INDUCED BY MANGANESE DEPOSITION

Manganese deposition on the graphite anode is also known as one of the major problem of the capacity fade. Dissolved manganese ions are deposited onto the graphite anode and can deplete the lithium in the graphite anode. Owing to manganese deposition onto the graphite, inserted lithium ions are taken out from the graphite electrode; consequently, overall capacity is decreased. It is also known that deposited manganese interacts with SEI layer which cause resistance increase and other complicated side effects. All these reactions will directly decreases the cell capacity due to manganese contamination of the graphite materials.

There are several studies focused on manganese contamination of graphite materials. The catalytic effect of deposited products toward solvent reduction is proposed as an additional capacity fade phenomenon [1-3]. Several XPS measurements were conducted to enlighten the mechanisms of manganese deposition by elucidating the chemical state of the manganese in the SEI layer of the graphite. The oxidation state of manganese present in the SEI layer of the graphite differs from the literature in the case of Mn metal [4, 5], Mn^{2+} or Mn^{3+} [1, 2, 6, 7]. Previous studies still suspected that the metallic state of Mn induces solvent reduction on the graphite surface [1-3]. The reasons for this speculation owe from the fact that 1) Mn metal was found from XPS measurement [4, 5]; 2) Mn^{2+} and Mn^{3+} (a form of $MnCO_3$, MnO_2 or Mn_2O_3) does not possess sufficient electronic conductivity to induce additional electrolyte decomposition [1, 2, 6]; and 3) capacity fade solely due to Mn reduction is too small and cannot explain continuous capacity decrease [8, 9]. Accordingly, manganese ions reduce manganese metal and then re-oxidize with electrolyte to form manganese compounds which cause significant capacity fade due to higher conductivity of the metallic surface. On the other hand, a recent study proposes that a metathesis reaction takes place as the manganese deposition mechanism is activated between Mn^{2+} and some species from the SEI layer rather than reduction reactions which lead to the formation of metallic manganese [7]. It is suggested that the manganese oxidation state does not depend on chemical potential or reactions during the discharge/charge process. The researchers proposed an ion-exchange model for manganese deposition on the graphite anode. Currently, the oxidation state of manganese in the SEI layer and the mechanisms of manganese deposition are still being debated in the literature.

However, a comprehensive understanding of manganese's impact on the graphite negative electrode is still limited. It is not yet clear how manganese ions induce side reactions on the graphite anode, affecting capacity decrease and cell performance. Also, the corresponding direct observation of the decomposed layers due to manganese deposition on the graphite surface is expected but still missing. It has been commonly understood that manganese deposition and the formation of SEI layer both critically impact the graphite negative electrode in terms of capacity and cell performance [10]. Nevertheless, none of the previous literature clearly explains the interactions and reactions between SEI layer on the graphite surface and manganese ions from the $LiMn_2O_4$ electrode. The objective of this study is to investigate the effect of manganese deposition and its side reactions on the graphite anode, and finally to elucidate the relationship between the amount of deposited manganese and capacity fade and electrochemical performance change in Li-ion battery systems.

3.1 Methods

3.1.1 **Experiment methods**

Since individual measurement techniques provide only limited information about a certain phenomenon, multiple complementary measurements are employed in various experimental conditions to achieve a comprehensive understanding of manganese deposition. Several electrochemical measurement techniques, such as CV, EIS and cycling testing, are employed to investigate how manganese ions influence the graphite electrode in terms of cell performance and capacity retention. In this chapter, four main topics are focused on in order to investigate both manganese deposition and consecutive side reactions. Those include 1) interactions between Mn ions and the SEI layer; 2) the relationship between the lithiation-status and manganese deposition; 3) cycling effects of Mn deposition on electrochemical performance; and 4) direct observation of decomposed layers induced by Mn deposition.

First, interactions between manganese ions and the SEI layers were investigated. Previous studies [10] indicate that graphite electrodes exhibit a sharp decay of capacity during the first few cycles. This is primarily due to Solid Electrolyte Interface (SEI) film growth on the graphite surface. After the formation cycles, the lithium-ion cells stabilize and maintain a constant capacity. Generally, the manganese ions are generated from the dissolution process of the cathode materials; thus, transport and deposition into the anode are expected after the formation of the SEI layer. However, a study of Mn-ion effects on the SEI layer would provide a contrast to standard measurements after the SEI layer is formed. Also, the SEI layer itself is not very robust, especially at high temperatures. Consequently, at high temperatures, the large amount of Mn ions from the accelerated dissolution may have an impact on the reformation of SEI layer due to its instability. In order to differentiate the impact of manganese on graphite electrode with and without SEI layer, fresh and cycled graphite electrodes are examined.

Second, the relationship between the lithiation-status of graphite and manganese deposition as well as operating voltage and manganese deposition were examined. The amount of lithium residing in the graphite electrode will influence the interactions between manganese ions and the graphite electrode. Therefore, lithiated and delithiated graphite samples are used in cycled graphite electrodes to investigate the relationship between state-of-charge and reactions related to manganese deposition. Moreover, the operating voltage window and corresponding reaction change is critical to the cell performance. In order to investigate reaction change due to manganese deposition, GCPL (Galvanostatic cycling with potential limitation) measurements were performed while separating the voltage window below and above the potential where manganese reduction occurs. One previous study recently suggested that manganese deposition is caused by metathesis reactions [7] rather than by manganese reduction [1-3]. These experiments will also give clear explanations of this ongoing topic.

Third, electrochemical measurements such as CV, cycling testing and ICP-OES measurements were performed with different conditions of graphite samples to investigate the cycling effect of manganese deposition. One of the main issues emerging from the side reactions is impedance change due to the development of by-products from the side reactions. In order to investigate changes in cell impedance, EIS measurements were also performed on the cycled graphite electrode. After cell capacities and impedances were identified, ICP-OES measurements were carried out to measure the exact amount of manganese deposited on the graphite. By comparing the amount of deposited manganese and changes in capacity and impedance, the connections among manganese deposition and side reactions as well as their influence on cell performance were investigated. In addition, separate experiments were performed to measure the amount of lithium extracted from the graphite anode due to manganese ions. These experiments can provide information parallel to previous experiments with regard to the Mn-Li exchange mechanism.

Finally, previous studies have shown that manganese deposited onto the graphite surface was detected by various techniques such as XPS [4], SIMS [11], ICP-OES and EPM [9]. In turn, it was proposed that the decomposed layer would be formed due to drastic decomposition of the electrolyte on the manganese metal surface [4]. However, no study has directly observed whether the additional layers were formed due to manganese deposition. In this work, in order to clearly observe the decomposed layers formed on the metallic state of the manganese surface, the graphite electrode was replaced with a manganese metal. Both fresh and cycled manganese metal surfaces were directly observed to see whether manganese was induced to form decomposed layers using SEM (Scanning Electron Microscope). Elemental analysis was also conducted on these samples using EDS (Energy Dispersive Spectroscopy) to confirm that metallic states of manganese form an additional passivation layer with electrolyte decomposition products.

3.1.1.1 Sample preparation

3.1.1.1.1 Coin cell assembly and disassembly

Graphite composite electrodes were assembled to sealed 2032 type coin cells (MTI) with a Lithium foil (Alfa Aesar) counter and reference electrodes with a separator (Celgard 2320). Formation cycling was performed three times at C/10. Finally, the cell was disassembled in the glove box and reassembled with the electrolyte possessing different concentrations of manganese for further experiment.

3.1.1.1.2 Electrolyte with pre-dissolved manganese ions

In order to investigate the direct impact of manganese ions on graphite composite electrode, the desired concentrations of manganese were dissolved in the electrolyte in advance. 50, 100, 150 and 200ppm of $Mn(PF_6)_2$ were added into an electrolyte composed of 1M of $LiPF_6$ salt (Aldrich) in ethylene carbonate (EC) and dimethyl carbonate (DMC) of 1:1 solvent mixtures to achieve the target concentration of manganese in the electrolyte. Exact concentrations of manganese in the electrolyte were measured by using Inductively Coupled Plasma- Optical Emission Spectroscopy (ICP-OES).

3.1.1.2 Electrochemical measurements

In order to measure the impact of the manganese on the graphite composite electrode, CV, capacity, and EIS measurements were performed. By using graphite electrodes and different concentration of manganese of electrolyte, graphite/lithium half-cells were constructed to decompose the effect of the dissolved Mn-ion for anode side and cathode side.

Cyclic Voltammetry was applied to Li/Graphite cell to measure redox currents and current peak changes immediately following the addition of different concentrations of manganese. CV was carried out at 0.5mV/s between 0.1V to 3.0V for Li/graphite cell. Interfacial currents and current peak changes were measured during the formation cycles. Capacity was measured using Li/graphite half-cells from 0.1V to 0.9V with C/10 for 20 cycles.

Electrochemical Impedance Spectroscopy (EIS) measurements were performed to measure impedance change due to the different concentrations of manganese and different potential of the electrode/electrolyte interface. Each concentration of manganese was measured with EIS at different voltages (0.1, 0.3, 0.5, 0.7 and 0.9V) and different manganese concentrations (0, 50, 100, 150 and 200 ppm) in the electrolyte. Before conducting EIS measurements, the cells were rested in the Open Circuit Voltage (OCV) condition for 2 hours to achieve stabilized potentials. AC impedance spectra were obtained by applying sinusoidal waves with amplitude of 5 mV over frequencies ranging from 100 kHz to 10 mHz.

3.1.1.3 ICP-OES measurements

In order to determine the correlation between manganese deposition and capacity retention, the amount of manganese deposited on the $LiMn_2O_4$ composite and graphite electrode were measured after the capacity of the cells were measured. After disassembly from the coin cells, the cycled $LiMn_2O_4$ composite and graphite electrodes were immersed in 25% nitric acid in water for 24 hours to extract the manganese. Next, ICP-OES measurements were carried out on the dissolved manganese from the positive and negative electrodes.. Samples were stored in 1 mL of EC: DMC (1:1 by volume) with 0, 50 and 100 ppm of manganese ions at room temperature for 7 and 14 days.

3.1.1.4 SEM and EDS measurements

The coin cells were first made with Li metal as a negative electrode and manganese metal as a positive electrode with 1M of $LiPF_6$ in EC: DMC (1:1 by volume) electrolyte and then cycled using the Potentiodynamic cycling method. The cycled manganese metal surface was cleaned with DMC (Dimethyl Carbonate) and scanned using SEM. Next, an elemental analysis was performed on the manganese metal surface by EDS.

3.2 Results

3.2.1 **Experiment results**

3.2.1.1 Cyclic Voltammetry (CV) measurements - Fresh graphite electrode

Figure 3.1 shows the results of Cyclic Voltammetry for the fresh graphite electrode with 0, 100 and 200 ppm of manganese ions in the graphite/lithium half-cell during (a) 1st cycle, (b) 10th cycle, and (c) 20th cycle. First, there are changes in the peaks of anodic and cathodic currents depending on the manganese concentrations. In order to track the changes of reactions induced by manganese ions more thoroughly, the cathodic and anodic current peaks of the CV curve marked as A, B and C in Figure 3.1 (a) were extracted as shown in Figure 3.2(a), (b) and (c), respectively. Region A can be interpreted as the electrolyte reduction and manganese deposition peak, whereas regions B and C represent lithium intercalaction and deintercalation peak regions. Higher concentrations of manganese in the electrolyte cause increases in the cathodic current from 2.0V to 0.1V (vs. Li/Li^+) and decreases in the anodic current peak from 0.3V to 0.6V (vs. Li/Li^+) as well as in the cathodic current peak near 0.3V to 0.1V as shown in Figure 3.2(a), (b) and (c), respectively. Manganese deposition occurred during the reductive current scan below the standard redox potential of Mn/Mn(II), which is about 1.87V (vs. Li/Li^+). After the manganese was deposited, subsequent electrolyte reduction reactions followed from the 0.8V to 0.6V region (vs. Li/Li^+). In the potential range of 0.5–0.2V, co-intercalation of the solvent and subsequent reduction of the electrolyte molecules occurred while forming SEI layer [12]. During the formation of SEI layer, electrolyte decomposition products such as $(CH_2OCO_2Li)_2$, ROLi, and LiF were passivized on the graphite surface [13]. However, due to the higher reactivity of manganese metal on the surface, the electrolyte reduction accelerated more violently at the higher concentration of manganese in the electrolyte. Due to the additional electrolyte reduction and manganese deposition reactions, decomposed layers might grow thicker and hinder lithium ions from the intercalation/deintercalation process. Consequently, the ability for lithium to (de)intercalate into the graphite considerably decreased. It can be seen that the cathodic current from 0.2V to 0.1V and the anodic current from 0.1V to 0.4V (vs. Li/Li+) (where lithium intercalation/deintercalation reactions dominate) decreased significantly as indicated in Figure 3.2 (b) and (c).

Next, as the cycle number increases, redox current related to the lithium intercalation/deintercalation process increases, and current related to side reactions such as electrolyte reduction and manganese deposition decreases. As can be seen from (a) to (c) and Figure 3.2(c), the anodic current peak related to lithium deintercalation near 0.3V ~ 0.6V increases and sharpens as the cycle number increases. This interfacial current increase was due to a slow wetting process of active material mass [14] with the subsequent progressive change in the nature of stable SEI layer on graphite [15]. Similarly, the cathodic current related to lithium intercalation also increased during the first few cycles as seen in Figure 3.2(b). On the other hand, the reductive currents between 2.0V to 0.5V (vs. Li/Li$^+$), which is where manganese deposition and electrolyte reduction take place, diminish as cycle number increases, as seen in Figure 3.2 (a).

Finally, manganese ions in the electrolyte created an additional oxidation reaction during initial cycling. The anodic current peak from 0.3V to 0.6V (vs. Li/Li$^+$) decreased while broadening and also shifted to the higher potential region due to manganese ions in the electrolyte. It seems that there is an additional anodic current peak generated between 0.3V to 0.6V which results in a broader current peak at the initial cycle. After 10 cycles, the broad anodic current peak narrows similar to the peak of the cell without manganese ions. Additional oxidation occurred due to the manganese ions at first, and these oxidation reactions fade away with time. It is supposed that this additional oxidation might be represented by the following reaction:

$$Mn^{2+} \rightarrow Mn^{3+} + e^{-} \quad (1.545\ \text{V vs. Li/Li}^{+}) \tag{3.1}$$

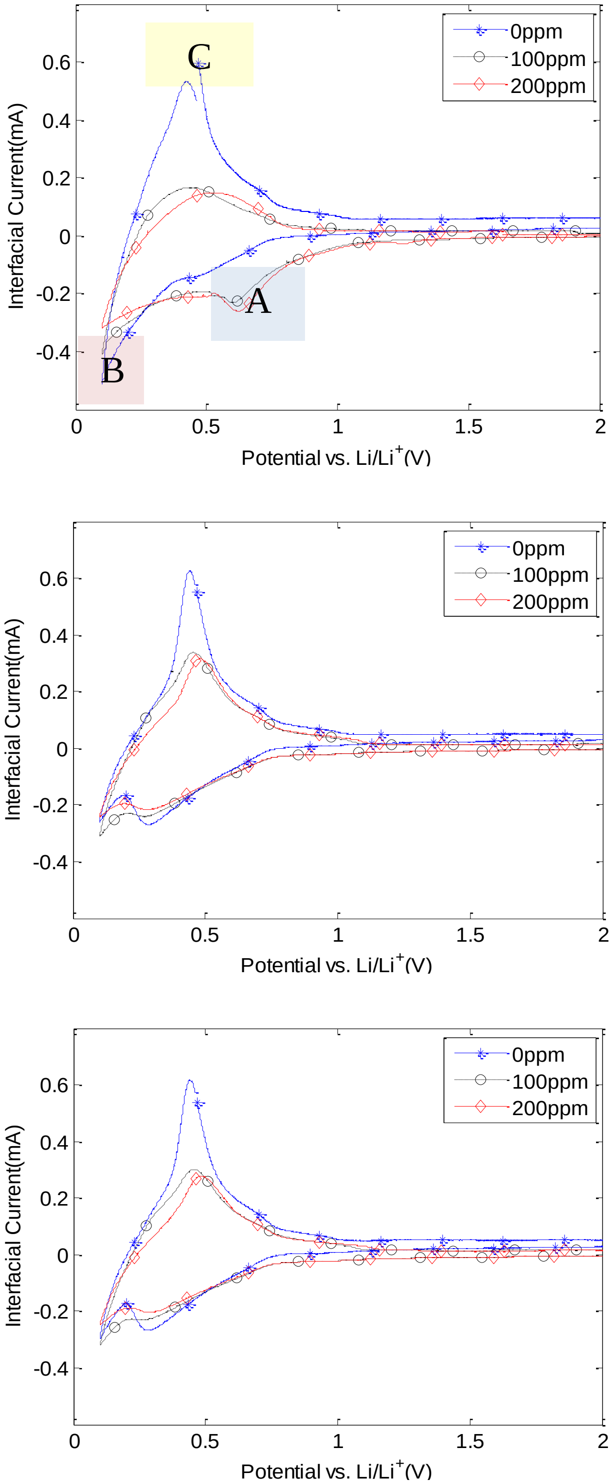

Figure 3.1 Cyclic Voltammetry of fresh graphite electrode after adding different concentrations of manganese ions into the graphite/lithium half-cell during (a) 1st cycle (b) 10th cycle (c) 20th cycle. CV was carried out at 0.5mV/s between 0.1V and 3.0V.

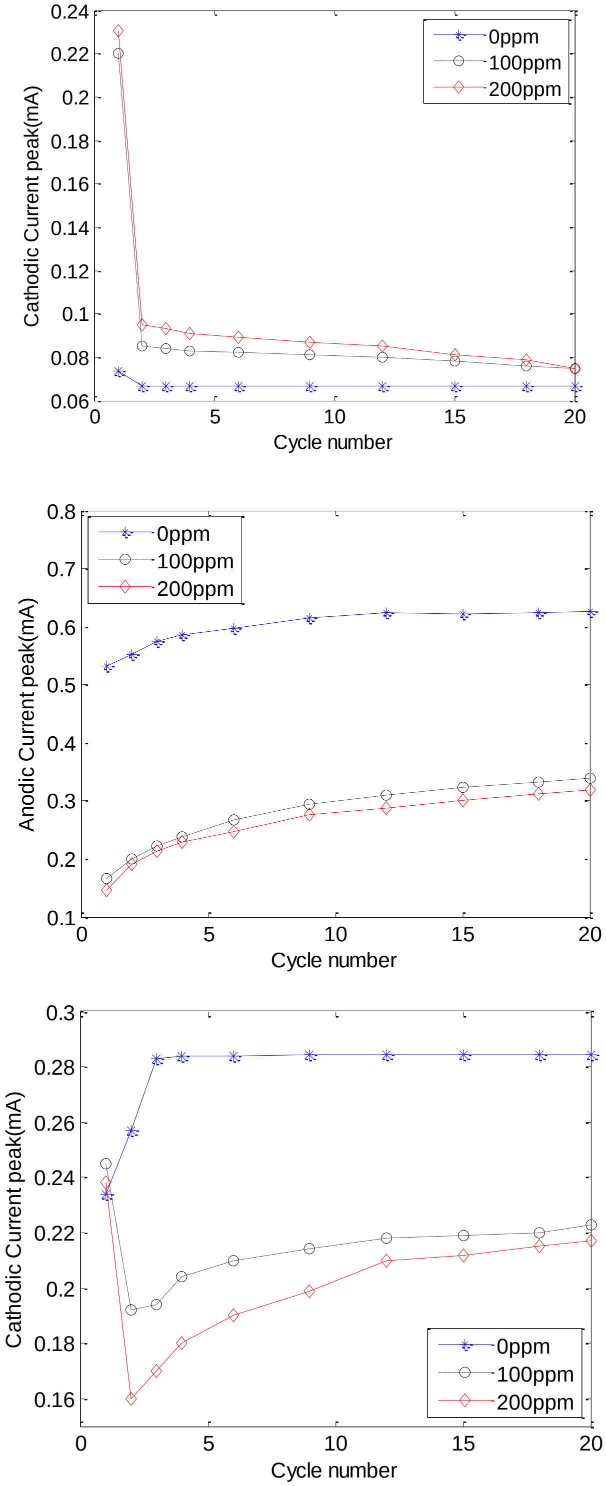

Figure 3.2 Current peak change after adding different concentrations of manganese into fresh graphite/lithium half-cell of the region (a) Mark A (b) Mark B (c) Mark C from Fig. 1. CV was carried out at 0.5mV/s between 0.1V and 3.0V.

3.2.1.2 Cyclic Voltammetry (CV) measurements - Cycled graphite electrode

Figure 3.3(a) shows the initial Cyclic Voltammetry (CV) curve right after adding different concentrations of manganese ions into the lithiated graphite/lithium cell. Since the cycled graphite samples contained lithium ions in the particles before the cell was reassembled, redox currents due to the lithium deintercalation process significantly increased at the initial cycle. On the other hand, it is observed that the higher concentration of manganese results in an additional increase of anodic current immediately after putting manganese into the first cycle. These phenomena were interesting because they are opposite results derived from the case of the fresh graphite electrode. Moreover, it can be noted that the intensities of the lithium deintercalation reactions were influenced by the amount of manganese ions in the cell. It seems that anodic current facilitates manganese oxidation and creates additional electrons from the reaction [1]. Thus, the increase of redox current due to manganese ions can be seen in Fig. 17(a).

Figure 3.3(b) shows the Cyclic Voltammetry curve of cycled lithiated graphite during the 5th cycle after adding a different concentration of manganese. Similar to the fresh graphite electrode case, it is found that the higher concentration of manganese causes further decrease in reversible lithium intercalation/deintercalation currents. Both the cathodic and anodic current peaks in the 5th cycle of the CV curve with a higher concentration of manganese ions were smaller than the lower concentration of manganese ions. Smaller interfacial currents can be interpreted as a decrease of the amount of lithium insertion/deinsertion into the graphite, resulting in capacity fade. As a result, the higher concentrations of manganese ions in the cell cause reduction of more reversible interfacial currents after a few cycles.

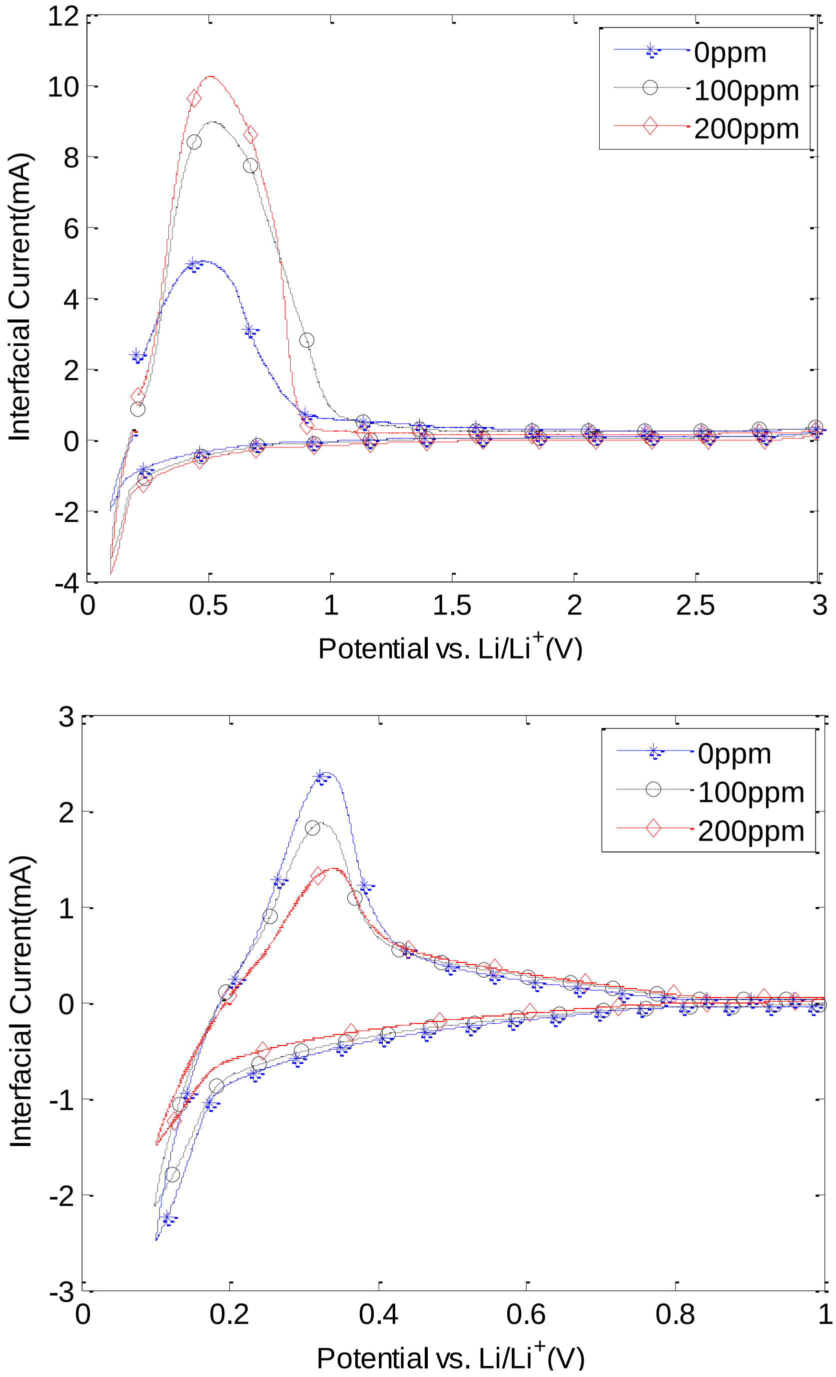

Figure 3.3 Cyclic Voltammetry of cycled graphite after adding 0, 50, 100, 150 and 200ppm of manganese ions in the electrolyte added into the lithiated graphite/lithium cell during (a) 1st cycle and (b) 5th cycle. CV was carried out at 0.5mV/s between 0.1V and 3.0V

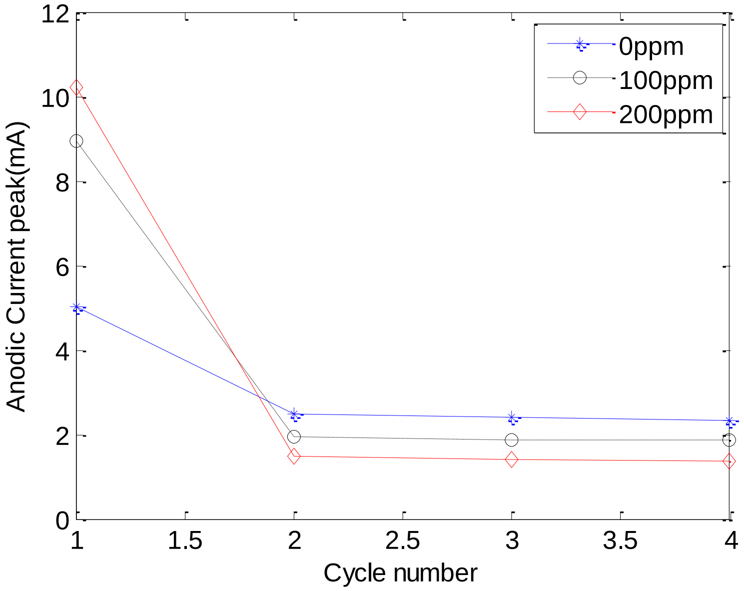

Figure 3.4 Anodic current peak change after adding different concentrations of manganese into the cycled lithiated graphite/lithium half cell

However, it is found that higher concentrations of manganese in the electrolyte have higher current peaks at the initial cycle and decrease further after the 2nd cycle. The anode current peak was remarkably decreased after the first cycle and stabilized after subsequent cycles, as shown in Figure 3.4. Considering the higher anodic current in the higher concentration of manganese at the initial cycling test, this means that more oxidation reaction occurred during the first CV cycle right after adding manganese ions into the cell. As can be seen from Figure 3.3(a), the manganese ions contributed to an increase of the cathodic current before manganese deposition occurs.

Figure 3.5(a) shows the CV curve right after adding 100ppm of manganese ions into the de-lithiated graphite/lithium cell. The anodic and cathodic current remarkably decreased at the 1st cycle of the CV after re-assembly of the cell, especially at higher concentrations of manganese ions. This result is contradictory to the previous CV results, which used lithiated graphite for the anode. A higher concentration of manganese caused a dramatic increase in the interfacial current in the lithiated graphite, whereas it caused a decrease in the de-lithiated graphite electrode. The main reason for this discrepancy is that the reduction of manganese and electrolyte occurred in the delithiated graphite compared to the lithiated graphite during the first cycle before oxidation occurs. It is supposed that manganese ions have a positive effect on cell performance by increasing the redox current before the manganese ions deposit onto the graphite. However, the cathodic and anodic currents significantly decrease right after the reductive scan is finished, as shown in Figure 3.4.

On the other hand, the Cyclic Voltammetry curve of cycled delithiated graphite during the 5th cycle after adding a different concentration of manganese is shown in Figure 3.5(b). The higher concentration of manganese ions in the electrolyte causes a greater decrease in interfacial currents, as expected. It is expected that manganese ions deposit quickly onto the graphite surface because of the higher standard redox potential of Mn/Mn(II) (1.87 vs. Li/Li+) compared to the lithium intercalation of graphite (<0.3V vs Li/Li+) [10]. Right after manganese deposition on the graphite surface, deposited manganese may react with other components such as C and O originating from electrolyte reduction and form another electrolyte interface layer containing manganese. Manganese deposition on graphite not only forces cycle-able lithium to be deintercalated from the graphite, but also induces electrolyte reduction reactions, both of which result in significant capacity fade. Moreover, it will influence power performance. The exchange current due to lithium intercalation/deintercalation further reduces the higher concentration of manganese in the electrolyte, as shown in Figure 3.3(b). This negatively impacts power performance.

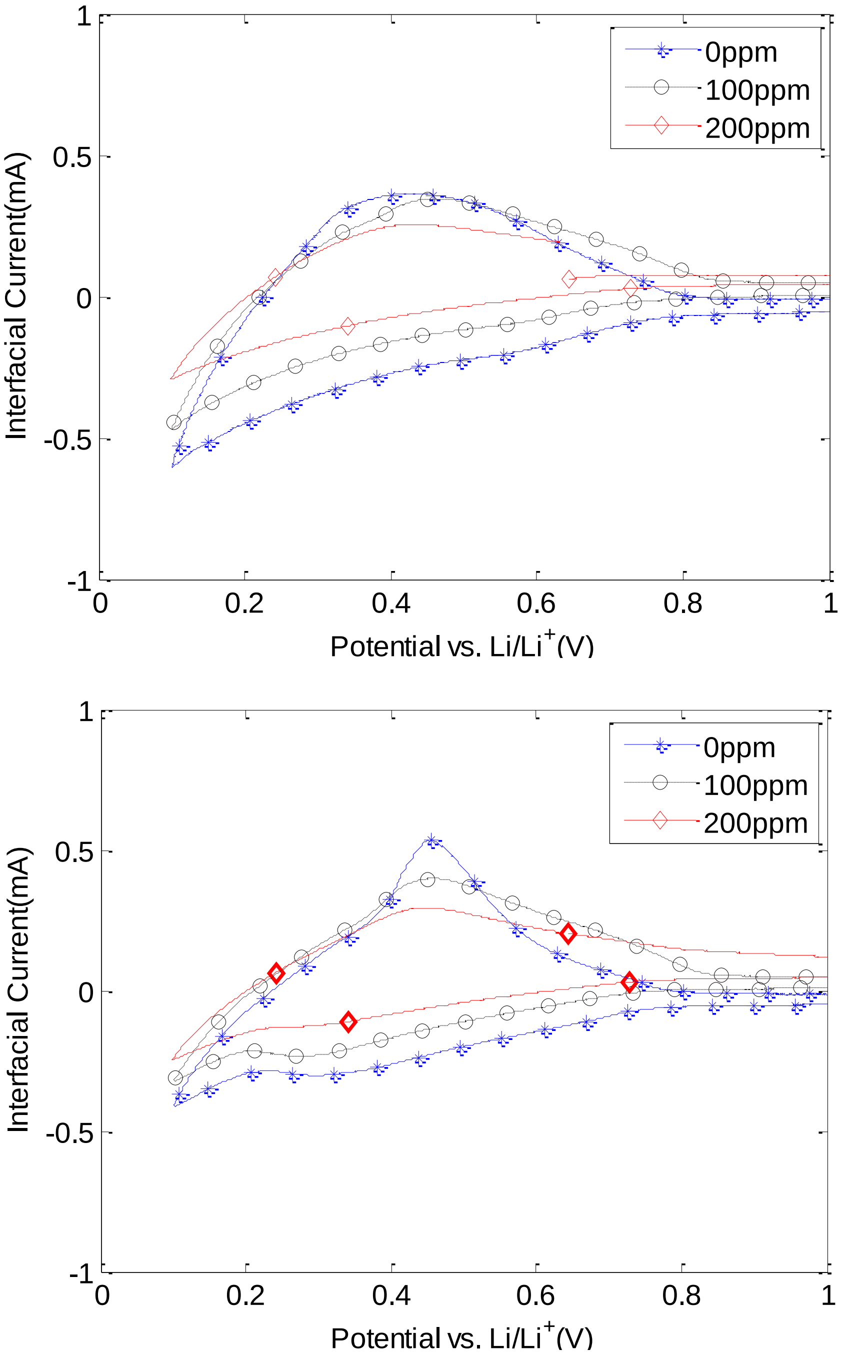

Figure 3.5 Cyclic Voltammetry of cycled graphite after adding 0, 100 and 200ppm of manganese ions in the electrolyte added into the de-lithiated graphite/lithium cell during (a) 1st cycle and (b) 5th cycle. CV was carried out at 0.5mV/s between 0.1V and 3.0V

3.2.1.3 Capacity measurements - Fresh graphite electrode

Figure 3.6(a) and (b) show the respective charge and discharge capacity change of fresh graphite electrode with cycle number after putting different concentrations of manganese into the cell.

In the first cycle, charge capacity decreased significantly due to SEI growth and irreversible electrochemical decomposition of the electrolyte. This common phenomenon is called irreversible charge loss (ICL) originating from solvent reduction and SEI formation, which is characteristic of the SEI layer [13]. However, higher concentrations of manganese ions in the electrolyte cause significant decrease of irreversible charge capacity when forming SEI layer on the graphite electrode. For example, the charge capacity of the cell decreased 37% when adding 200ppm of manganese ions and only 17% when no manganese ions are injected, as shown in Figure 3.6(a). It is highly likely that manganese ions in the electrolyte are deposited earlier due to the higher standard potential compared to electrolyte reduction and SEI layer formation. Higher reactivity of deposited manganese induces additional electrolyte reduction and decomposed layer growth. The charge capacity of the graphite does not change meaningfully as cycle number increases after the first few cycles. Electrolyte reduction and manganese deposition reaction did not aggressively take place after the initial SEI layers was formed.

On the other hand, discharge capacity does not decrease much compared to charge capacity during first few cycles [16]. However, discharge capacity of the graphite electrode was continuously decreased during those 20 cycles. It was obvious that higher concentrations of manganese caused greater capacity decrease. After 20 cycles, about 15% of capacity decreased when 200 ppm of manganese ions in the electrolyte was added into the electrolyte as shown in Figure 3.6(b). Presumably, deposited manganese with electrolyte decomposition products on the graphite surface hinders the lithiation/delithiation process during cycling, which affects the unceasing decline of the discharge capacity of the cell. Moreover, the capacity of the cells kept decreasing as the cycle number increased, which means that passivation of the SEI layer was not fully established on the graphite surface. These results agreed with the previous study [2], which proposed that high electronic conductivity of the manganese metal formed on the graphite surface might be the reason for this lack of passivation effect. It is suggested that the conversion reaction of lithium and trapped manganese in the SEI layer will constantly provide metallic manganese and cause continuous capacity fade as can be seen in Fig. 20(b).

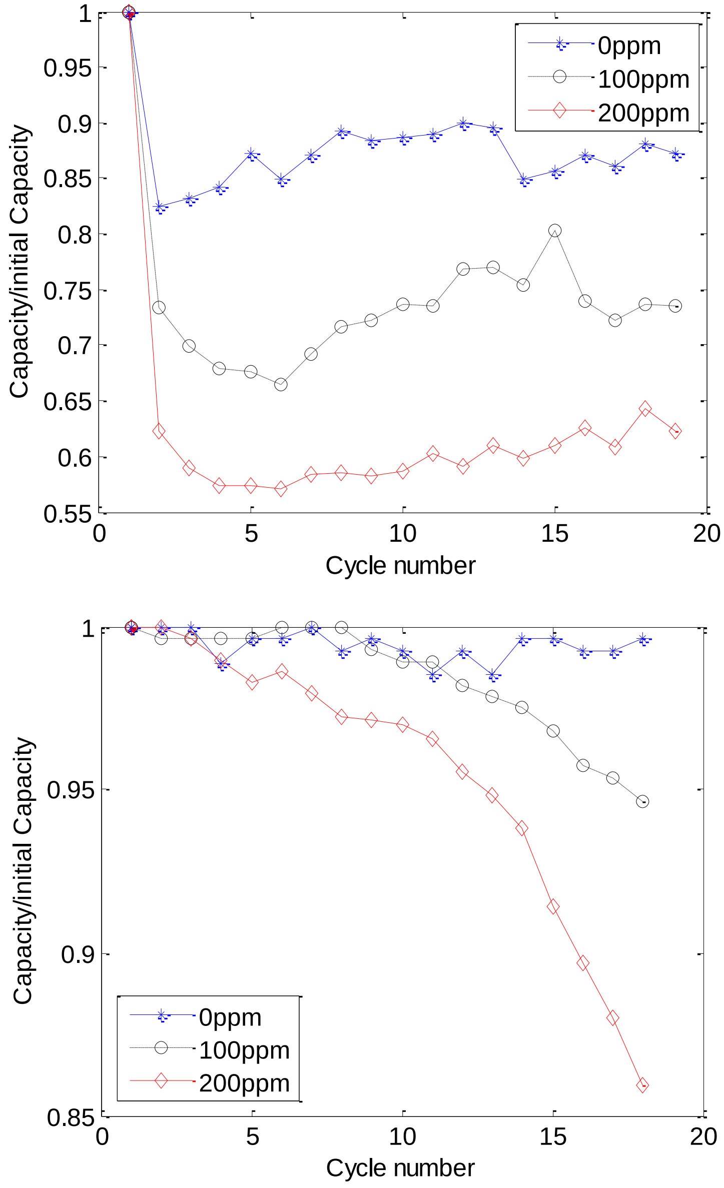

Figure 3.6 (a) Charge and (b) Discharge capacity change of fresh graphite electrode with cycle number after adding 0, 100 and 200ppm of manganese ions in the electrolyte.

3.2.1.4 Capacity measurement - Cycled graphite electrode

Capacity change of the cycled graphite electrode was measured before and after adding different concentrations of manganese in the electrolyte, as shown in Figure 3.7(a). Because the cycle-able lithium ions resided in the lithiated graphite electrode, the capacity slightly increased during the 4th cycle when the cell was re-assembled after the formation cycle. Consistent with the previous CV findings using lithiated graphite (which determined that the redox current increased due to manganese oxidation), capacity increased more when higher concentrations of manganese in the electrolyte were added to the cell. Increases of discharge capacity were probably due to the additional electrons coming from manganese oxidation right after the addition of manganese ions. However, the decreased rate of capacity with higher concentrations of manganese ions was significantly higher than that of the lower manganese concentration. It seems that the manganese ions in the electrolyte increase capacities in the cell, which positively affect the cell during initial cycling before manganese deposition. However, manganese deposition and consequent side reactions eventually increase capacity decrease rate. For instance, about 50% of the capacity decreased after 15 cycles, when 200ppm of manganese ions was added into the cell.

In order to support the claim that manganese ions improve capacity and cell performance before they deposit onto the graphite, additional experiments were performed. Cycled lithiated graphite was re-assembled with and without manganese ions and cycled between 2.0V to 3.0V with C/100 rate to avoid manganese from depositing and inducing side reactions on the graphite surface. Upon discharge of the lithiated graphite electrode, manganese oxidation should occur when the voltage rises from 0.1V to 3.0V. However, manganese deposition and electrolyte reduction is avoided by limiting the potential window from 3.0V to 2.0V of the cathodic current. C/100 charge and discharge rate was used in this experiment since the amount of lithium which can be inserted into the graphite is very limited. Figure 3.7(b) shows the discharge capacity of graphite before and after adding 0 ppm and 200 ppm of manganese ions into the electrolyte, respectively. It is obvious that manganese ions contribute to increase discharge capacity if they do not deposit on the graphite and provoke side reactions.

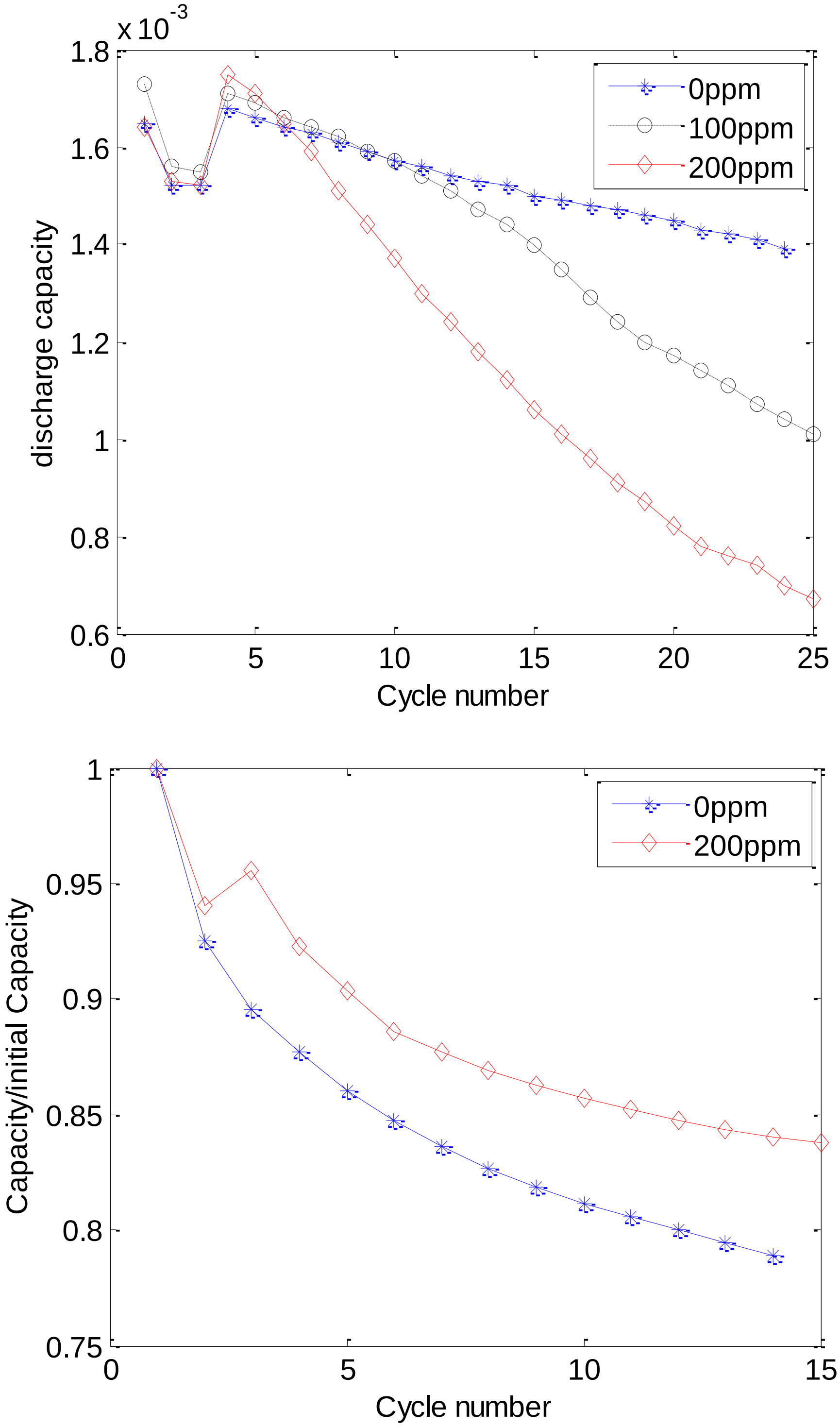

Figure 3.7 (a)Cycled lithiated graphite was re-assembled with and without manganese ions and cycled between 2.0 V to 3.0 V with C/100 rate. (b) Cycled lithiated graphite electrode was re-assembled after 2nd cycle.

3.2.1.5 Electrochemical Impedance Spectroscopy (EIS) measurements

Typical impedance spectra for a graphite composite electrode composed of a semicircle with an inclined slope can be seen in Figure 3.8 and Figure 3.9. By separating the frequency region of the EIS spectra, reactions and electrochemical characteristics of the electrode and electrolyte such as contact, charge transfer resistance and diffusion can be identified. The far left point of the semicircle in the higher frequency domain relates to the contact resistance of electrode and electrolyte, while the radius of the semicircle in the mid-range frequency zone is the charge-transfer reaction at the electrolyte/electrode interface. The inclined line connected to the semicircle on the right indicates the diffusion of lithium into the electrode. Figure 3.8(a) and (b) show the EIS spectra with different concentrations of manganese ions in the electrolyte at 0.1 and 0.7V, respectively. Impedance spectra shift to the right as the concentration of manganese ions in the electrolyte increases, implying contact resistance increase. Moreover, the radius change of the impedance spectra semi-circle also increased, which is closely related to the charge transfer resistance of the cell. Lastly, lithium diffusion into the graphite electrode is limited due to manganese ions. For instance, it can be clearly seen that the slope of the impedance spectra of the diffusion region with 0 ppm of manganese in the electrolyte is steeper than samples of different concentrations shown in Figure 3.8(a). It is well known that LiF generated from the salt reduction and $ROCO_2Li$ formed by the solvent reaction are the main contributors for increasing interfacial resistance at the surface of the graphite. These electrolyte and salt reduction processes will be accelerated when manganese ions are present in the electrolyte by depositing as a metallic state and acting as a catalyst on the graphite surface. EIS measurements confirm that the deposited manganese and additional interface layer also contribute to increasing contact and charge transfer resistance by impeding the lithium intercalation/deintercalation process and hindering the diffusion process into the graphite. These reactions will continuously degrade and decrease cell performance and capacity, respectively.

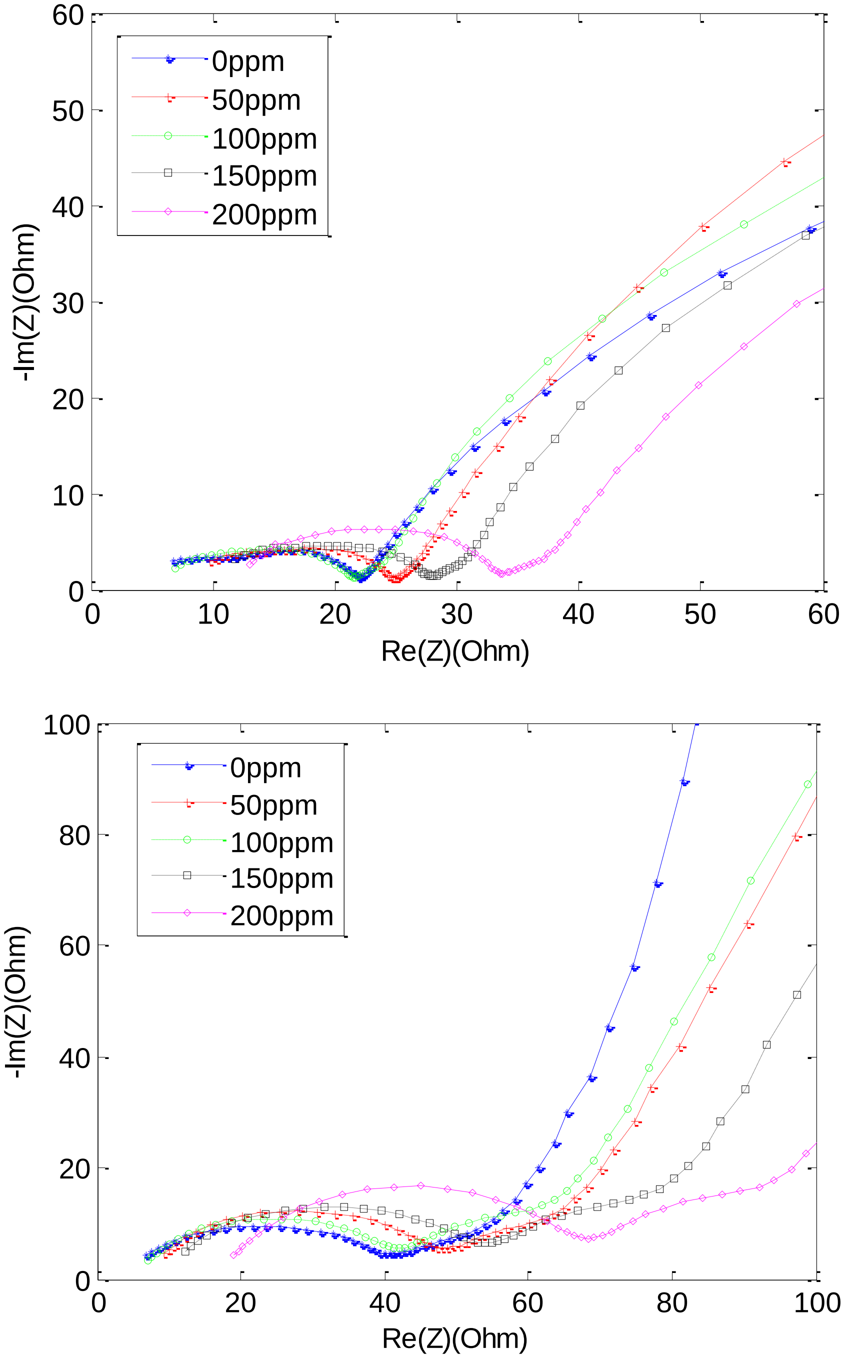

Figure 3.8 EIS spectra with 0, 50, 100, 150 and 200ppm of manganese ions in the electrolyte at (a) 0.1V and (b) 0.7V. AC impedance spectra were obtained by applying the waves with an amplitude of 5 mV over a frequency range from 100 kHz to 10 mHz.

Figure 3.9(a) and (b) show the EIS spectra at different voltages with 0 ppm and 50 ppm of manganese in the electrolyte, respectively. High frequency resistance remained similar throughout the voltage range. However, most of the impedance change was due to charge transfer resistance increase shown as the increase of the radius in the semi-circle in the figure. The amount of lithium in the graphite continuously decreases as the voltage of the cell increases from 0.1V to 0.9V. Since different amounts of the lithium are present in the graphite at different voltages, the charge-transfer resistance also changes with different voltages as expected because charge transfer resistance is SOC-dependent (41).

3.2.1.6 ICP-OES measurements for the amount of deposited manganese during cycling

In order to validate the hypothesis that capacity fade and redox current peak decreased due to manganese deposition, the amount of manganese on the graphite was measured using ICP-OES after the capacities were verified. As expected, higher concentrations of manganese added into the cell result in larger amounts of manganese deposition on the graphite as shown in Table 3.1. In addition, higher concentrations of manganese ions in the electrolyte contribute to larger discharge capacity loss as shown in Figure 3.6(a). Therefore, capacity decrease in the graphite anode is proportional to the amount of manganese ions added into the cell due to manganese deposition and its side reactions.

3.2.1.7 ICP-OES measurments for the amount of lithium loss during storage

The concentration of lithium was measured to investigate the correlation between manganese ions in the electrolyte and the amount of lithium deintercalation from the lithiated graphite electrode. The lithiated graphite electrode was put into the electrolyte with different concentrations of manganese and stored for 7 and 14 days in order to observe the effect of manganese on the charged graphite anode. Table 3.2shows the amount of deposited manganese on the graphite and the amount of lithium in the electrolyte measured using ICP-OES.

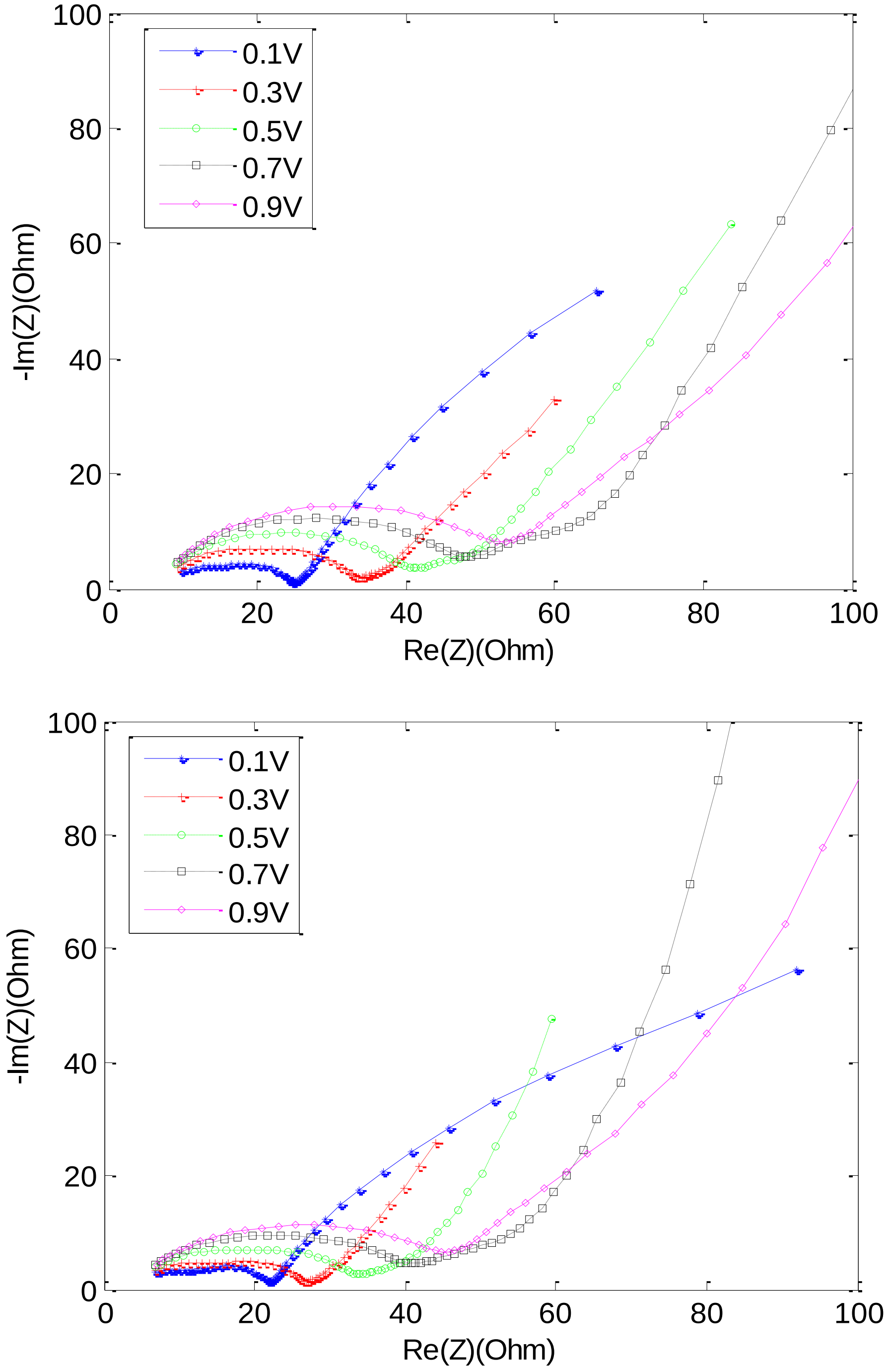

Figure 3.9 EIS spectra at 0.1, 0.3, 0.5, 0.7, and 0.9V (vs. Li/Li+) with adding (a) 0 ppm and (b) 50 ppm of manganese ions in the electrolyte. AC impedance spectra were

obtained by applying the waves with amplitude of 5 mV over a frequency range from 100 kHz to 10 mHz.

As expected, higher concentrations of manganese ions put into the electrolyte cause the deposition of more manganese on the graphite surface. Moreover, the amount of dissolved lithium in the electrolyte is increased if we put higher concentrations of manganese in the electrolyte. Even with 0 ppm of manganese in the electrolyte, 2.7 mols of lithium were dissolved into the electrolyte, which might be produced from lithium deintercalation due to the self-discharge of lithiated graphite. For instance, during long-term storage in open circuit voltage conditions, a current leakage will contribute to building the SEI layer by reacting with the electrolyte. Moreover, protic species coming from water are also reducible by consuming electrons from the graphite [17].

$$H^+ + e^- \rightarrow \frac{1}{2} H_2 \tag{3.2}$$

$$H_2O + e^- \rightarrow {}^1\!/_2 H_2 + HO^- \tag{3.3}$$

However, we can clearly see the effect of manganese ions since the amount of lithium coming out from the graphite remarkably increased as the larger amount of manganese was deposited. Moreover, the number of mols of lithium deinserted from the graphite was much higher than that of deposited manganese. These results show that manganese ions cause more than just the manganese-lithium exchange mechanism,

$$yMn^{2+} + Li_xC_6 \rightarrow yMn + Li_{x-2y}C_6 + 2yLi^+ \tag{3.4}$$

which might be only the small portion of capacity decrease from the overall capacity degradation.

From the results, the amount of lithium deintercalated from the lithiated graphite was significantly increased due to the manganese ions more so than by the stoichiometric amount of lithium from the manganese-lithium exchange mechanism [8, 9]. It is supposed that the additional formation of decomposed layers induced by manganese deposition provokes the generation of decomposed products such as LiF and RCOOLi, which additionally consume lithium from the graphite electrode.

Manganese concentration (ppm)	The amount of manganese deposited on the graphite(ug)
50	8.7783±0.18
100	14.528±0.83
150	28.078±1.35
200	31.378±1.81

Table 3.1 The measured amount of manganese deposited on the graphite with adding different concentration of manganese using ICP-OES after capacities were measured shown in Figure 3.6.

duration	Mn concentration (ppm)	The amount of deposited manganese on graphite (mol)	The amount of dissolved lithium in electrolyte (mol)
7days	0	0.00102	2.7492
7days	50	0.10584	3.4841
7days	100	0.17673	4.4027
14days	0	0.00134	2.7564
14days	50	0.11412	5.4639
14days	100	0.15899	6.3739

Table 3.2 The amount of deposited manganese on the graphite and dissolved lithium in the electrolyte. The graphite negative electrode was discharged with lithium metal (a reference electrode) and held at 0.05V (x is about 0.9 in Li_xC_6) for 3 hours before storage to achieve lithiated graphite electrodes. Samples were stored in 1 mL of EC: DMC (1:1 by volume) with different concentrations of manganese with 0, 50 and 100ppm at room temperature for 7 and 14 days.

3.2.1.8 SEM and EDS measurements

The current research predicted that deposited manganese metal induces the creation of decomposed layers with electrolyte reduction products on the graphite surface. In order to examine the suggested hypothesis, microscopic observations and elemental analysis were conducted via SEM and EDS, respectively. For clear observation of the layer generated on the manganese metal surface, the current study replaced the graphite anode with manganese metal. Figure 3.10 and Figure 3.11 show the images of the manganese metal before and after cycling as well as EDS spectra on the manganese surface, respectively. By comparing fresh and cycled manganese metal surfaces, it became clear that the additional decomposed layers are formed on the manganese metal surface. From the EDS spectra analysis, C, F and P element were detected in the cycled manganese metal surface as seen in Figure 3.11(b). These elements originated from the electrolyte decomposition product of the electrolyte and are the components of additional layers provoked by manganese metal surfaces. Similar processes can take place in the deposited manganese on the graphite anode surface.

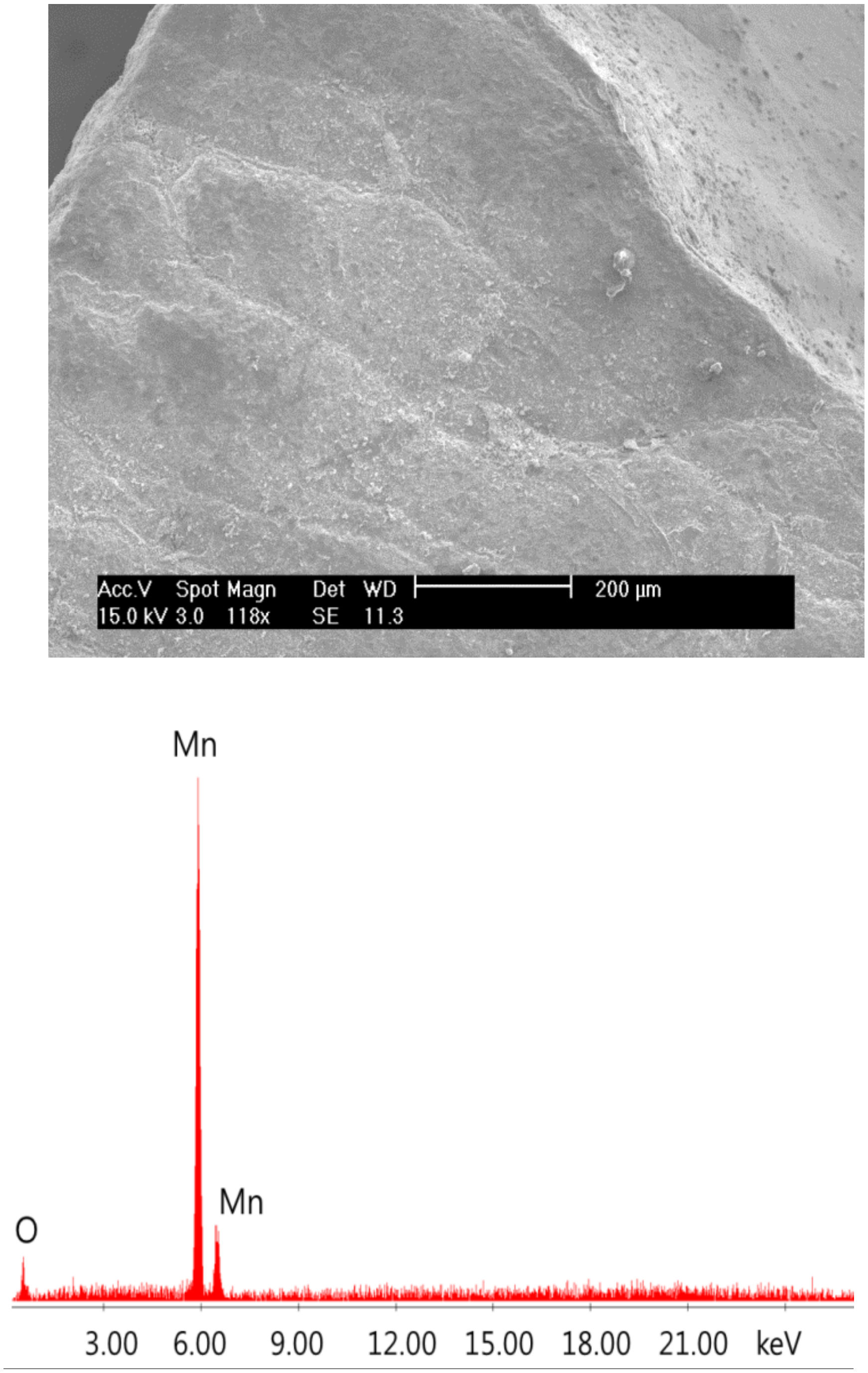

Figure 3.10 (a) fresh Mn metal surface with 118X magnification (b) EDS spectra on fresh Mn surface.

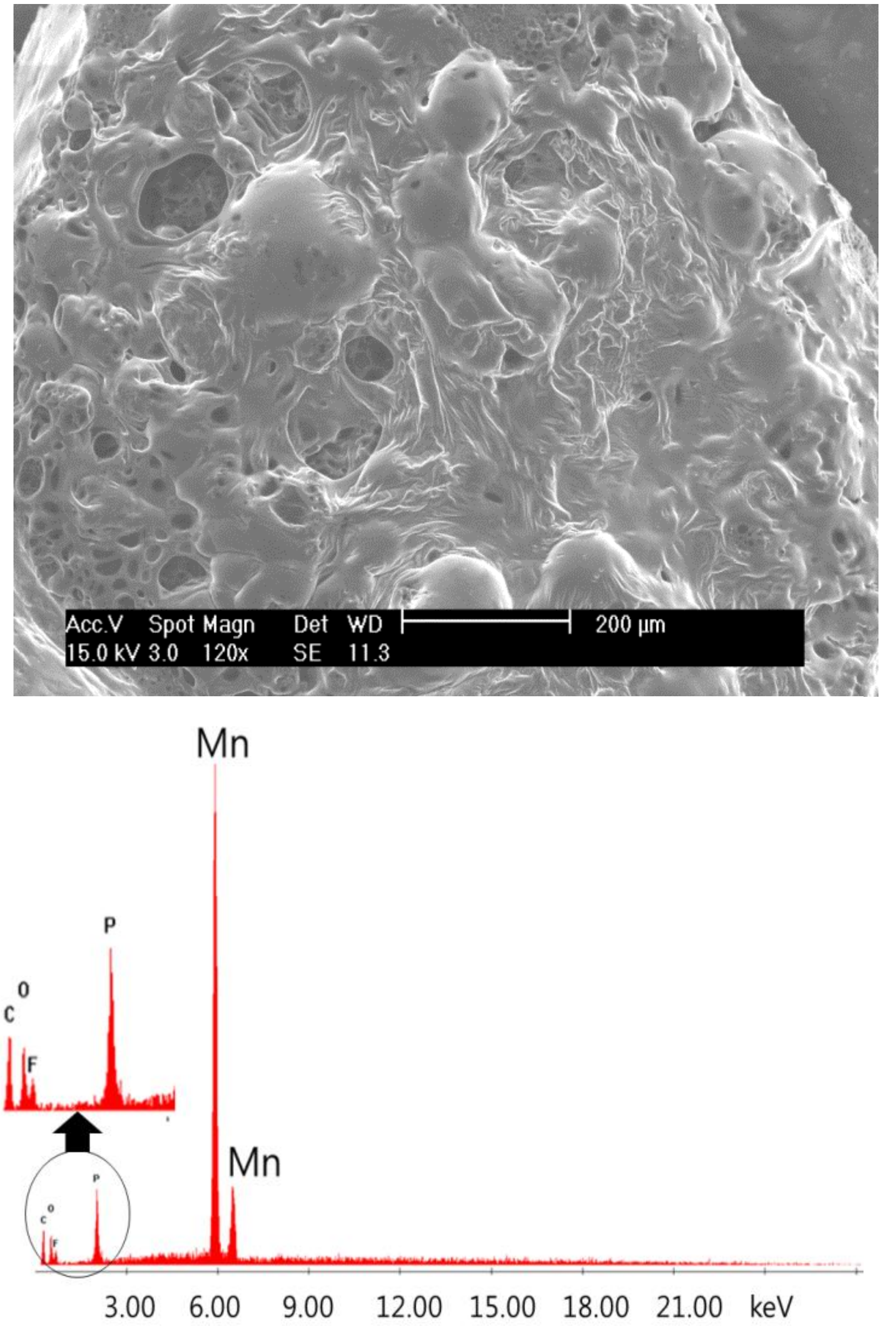

Figure 3.11 (a) cycled Mn metal surface with 118X magnification (b) EDSspectra on the cycled Mn surface.

3.3 Conclusions

From the results, it is obvious that manganese ions in the electrolyte provoke not only the dissolution of lithium in the electrolyte by reduction of manganese but also the formation of additional decomposed layers with electrolyte reduction products on the graphite electrode surfaces. Due to the higher reactivity of manganese metal on the surface, electrolyte reduction accelerates more violently when the higher concentration of manganese in the electrolyte is added to the cell. Due to solvent reduction and SEI formation at initial cycle, charge capacity of the cell decreased 37% when adding 200ppm of manganese ions and only 17% when no manganese ions are injected. Moreover, the amount of lithium deinserted from the graphite anode also increases due to manganese deposition. These processes will also contribute to form thicker decomposed layers on the graphite surface and hinder the lithium transport process, which causes contact resistance and charge transfer resistance increase. After 20 cycles, about 15% of discharge capacity decreased when 200 ppm of manganese ions in the electrolyte was added into the electrolyte. All these side reactions cause significant irreversible interfacial currents and discharge capacity decrease, which should be prevented to improve the cycle life of the battery electrode. Previous studies have not reached consensus on the oxidation state of manganese present in the SEI layer of the graphite. Since Mn metal is very reactive, it might be difficult to detect that from XPS. This is probably why several XPS measurements only observed an oxide form of Mn [1, 2, 6, 7], whereas some studies observed metallic state of manganese [4, 5].

From the various measurements of different graphite samples, the summary of the effect on the fresh, lithiated and delithiated graphite electrode due to the manganese ions are as follows:

1. Capacity and redox current increased due to the manganese ions before they deposited onto the graphite electrode and induced side reactions. However, right after manganese deposition, the redox current dramatically decreased. Moreover, capacity continuously decreased as the cycle number increased, which should mainly be caused by cell impedance rise.

2. Higher concentrations of manganese ions cause increases in currents related to side reactions but decreases in redox currents of reversible lithium intercalation/deintercalation reactions for both fresh and cycled graphite after manganese deposition occur. Moreover, capacity of the cell dramatically decreased, and impedance of the cell significantly increased.

3. Irrevesible side reactions such as electrolyte reduction and manganese deposition dominated the reaction when initially adding manganese ions into the cell. However, reversible lithium intercalation/deintercalation reactions increase and irreversible reactions fade away as the cycle number increases for both electrodes.

4. Interactions between Mn ions and SEI layer affect cell performance significantly. Decomposition of the electrolyte accelerated due to the higher conductivity of the manganese which also influences SEI layer formation. For instance, the side reaction due to the insertion of manganese ions quickly decline in the cycled graphite electrode compared to the fresh one. The current peak of the cycled graphite electrode changes during the 2nd cycle immediately as shown in Fig. 28., whereas the current peak of the fresh graphite electrode slowly transferred to the reversible peak around the 5th cycle. When the manganese ions were initially put into the cell, the manganese ions seem to be deposited before the SEI layers are formed due to the higher standard redox potential (1.87 V vs. Li/Li^+). Since deposited manganese metal has a higher reactivity than the graphite surface, subsequent electrolyte reduction reactions might be facilitated. In this process, side reactions due to manganese deposition progress rather slowly since this reaction will be accompanied by SEI layer formation throughout the whole graphite electrode area. However, when the manganese ions were put into the cell after SEI layers are present, they react and decrease redox current and capacity very quickly.

5. The operation voltage window of the cell is more critical to cell performance than the lithiation status of the graphite electrode when Mn ions are introduced to the cell. When the operating voltage is higher than the standard

potential of Mn deposition, the capacity of the cell does not decrease due to the Mn ions as shown in Fig. 21(b).

These interesting observations from the previous results suggest that manganese ions in the electrolyte positively affect capacity and cell performance if they are not deposited onto the graphite surface. Cell performance will be greatly improved due to manganese oxidation if manganese ions are prohibited from depositing onto graphite. Moreover, the presence of manganese ions in the electrolyte will reduce the generation of Mn^{2+} ions from the manganese-based cathode materials. Thus, different additives and coatings that prevent manganese deposition on the graphite might be one of the critical ways to improve capacity and cell performance.

BIBLIOGRAPHY

[1] S. Komaba, T. Itabashi, T. Ohtsuka, H. Groult, N. Kumagai, B. Kaplan, H. Yashiro, Journal of The Electrochemical Society, 152 (2005) A937-A946.

[2] C. Delacourt, A. Kwong, X. Liu, R. Qiao, W.L. Yang, P. Lu, S.J. Harris, V. Srinivasan, Journal of The Electrochemical Society, 160 (2013) A1099-A1107.

[3] S. Komaba, N. Kumagai, Y. Kataoka, Electrochimica acta, 47 (2002) 1229-1239.

[4] M. Ochida, Y. Domi, T. Doi, S. Tsubouchi, H. Nakagawa, T. Yamanaka, T. Abe, Z. Ogumi, Journal of The Electrochemical Society, 159 (2012) A961-A966.

[5] M. Ochida, T. Doi, Y. Domi, S. Tsubouchi, H. Nakagawa, T. Yamanaka, T. Abe, Z. Ogumi, Journal of The Electrochemical Society, 160 (2013) A410-A413.

[6] L. Yang, M. Takahashi, B. Wang, Electrochimica Acta, 51 (2006) 3228-3234.

[7] C. Zhan, J. Lu, A.J. Kropf, T. Wu, A.N. Jansen, Y.-K. Sun, X. Qiu, K. Amine, Nature communications, 4 (2013).

[8] H. Tsunekawa, S. Tanimoto, R. Marubayashi, M. Fujita, K. Kifune, M. Sano, Journal of The Electrochemical Society, 149 (2002) A1326-A1331.

[9] T. Tsujikawa, K. Yabuta, T. Matsushita, M. Arakawa, K. Hayashi, ECS Transactions, 25 (2010) 309-315.

[10] P. Arora, R.E. White, M. Doyle, Journal of The Electrochemical Society, 145 (1998) 3647-3667.

[11] D.P. Abraham, T. Spila, M.M. Furczon, E. Sammann, Electrochemical and Solid-State Letters, 11 (2008) A226-A228.

[12] J. Li, H. Su, L. Huang, S. Sun, Science China Chemistry, 56 (2013) 992-996.

[13] P. Verma, P. Maire, P. Novák, Electrochimica Acta, 55 (2010) 6332-6341.

[14] M.D. Levi, E. Levi, Y. Gofer, D. Aurbach, E. Vieil, J. Serose, The Journal of Physical Chemistry B, 103 (1999) 1499-1508.

[15] E. Markevich, V. Baranchugov, G. Salitra, D. Aurbach, M.A. Schmidt, Journal of The Electrochemical Society, 155 (2008) A132-A137.

[16] C. Wang, A.J. Appleby, F.E. Little, Journal of Electroanalytical Chemistry, 497 (2001) 33-46.

[17] A. Biyr, C. Sigala, J Eletrochem Soc, 145 (1998) 194-209.

CHAPTER 4

THE EFFECT OF ACTIVE MATERIAL, CONDUCTIVE ADDITIVES AND BINDER OF COMPOSITE ELECTRODE ON BATTERY PERFORMANCE

Selecting a proper format of electrode is important to maximize the battery usage, capacity, and performance in various applications. Among various electrode formats, composite electrode is the most widely used in current industry. While lithium intercalation compounds provide high potential and high gravimetric energy densities, both polymer binder and conductive additives are used to maintain a firm structure and to provide continuous conduction path. Due to low conductivity of the lithium intercalation compounds, conductive additives such as carbon black or acetylene black are added to composite electrode. In order to stick active material and conductive additives together without reacting with electrodes and electrolyte, polymer binder such as PVDF and EPDM is needed. However, conductive additives and polymer binder are both electrochemically inactive material. Too much adding conductive additives and polymer binder into the electrode sacrifices total capacity of the cell whereas too low adding them cause decrease in electronic conductivities and mechanical integrity of the electrode, respectively.

In order to improve the battery capacity and cell performance, detailed investigation of the effect of the conductive additives and the polymer binder on battery performance is critical. Numerous studies were performed to investigate the effect of each constituent material by considering different parameters. For instance, in order to achieve highest specific energy for $Li(Ni_{1/3}Co_{1/3}Mn_{1/3})O_{2,}$ ionic conductivity, electronic conductivity and porosity were investigated with different ratio of constituents [4]. Electronic conductivity and discharge capacity were also examined to achieve the highest capacity by varying $LiMn_2O_4$ and carbon black contents. [5]. Furthermore, optimal electrode utilizations for specific energy or power performance were proposed by using effective conductivity model. This effective conductivity model described the polymer binder distribution between conductive additives and polymer binder [6]. These findings suggest that the amount of conductive additives and polymer binder included in the electrode also influence different properties and parameters of the battery performance.

For instance, conductive additives in the composite electrode increase the overall surface area of the electrode because conductive additives have larger surface area than active materials. Conductive additives also increase the electronic conductivity of the composite electrode and decrease the ohmic resistances of the electrode. Moreover, they enhance the lithium intercalation/deintercalation reactions between electrode and electrolyte interfaces and generate more power of the battery. However, it is also reported that conductive additives also accelerate the side reaction of the battery. Primary side reactions [1] such as electrolyte decomposition, SEI layer formation and manganese dissolution also originated from the reactions between electrode and electrolyte interface. Intensity of these side reactions mainly influenced by the electrode area contacted with electrolyte as well as the porosity of the composite electrode. For example, Marks et al. [2] measured coulombic efficiency of two Li/graphite cells with one contained 4 wt% by weight Super-S carbon black and the other with 7 wt %. The coulombic efficiency of the electrode containing more carbon has more detrimental effect since SEI layer formation was boosted due to higher surface area. Similarly, manganese dissolution will be accelerated if more carbons are included in the positive composite electrode due to the higher surface area. Moreover, it is also suggested that solvent oxidation on the carbon surface is also responsible to increase Mn dissolution of the cathode. It is found that the dissolution of manganese was accelerated at higher potential especially over 4.0V. It is claimed that operating battery cell in the high voltage region is closely related to the current rise due to the solvent oxidation. [3] It is highly likely that not only due to higher surface area of the carbon but also the catalytic effect which accelerates solvent oxidation on the carbon surface also increase the manganese dissolution.

On the other hand, previous literature also reveal that higher ratio of polymer binder to conductive additives increase the interfacial resistance by ion- blocking effect at higher binder contents in the electrode [7]. However, it also showed that too little amount of binder also increases the resistance because binder cannot maintain firm structure of the electrode. Thus, there must be optimal ratio among conductive additives, polymer binder and active material which maximizes the battery performance.

Although many of the literatures focused on different properties and performance of the cell such as resistance, conductivity and capacity of the electrode to optimize the electrode material, the effects of side reactions on the cell performance were often neglected. Since manganese dissolution is one of the most important degradation phenomena in the $LiMn_2O_4$ cathode material, the changes in capacity and cell performance due to manganese dissolution should be considered. Therefore, this chapter investigates the effect of conductive additives and binder from $LiMn_2O_4$ composite electrode on capacity fade in terms of manganese dissolution, electronic conductivity and impedance.

Our specific objectives of this study were as follows:

1) to measure the amount of manganese dissolved into the electrolyte, conductivity and interfacial resistance change from composite electrode with different composition of active material, additive material and PVDF binder in different conditions
2) to correlate the manganese dissolution and binder effect with cycling performance
3) to simulate capacity fade due to manganese dissolution and binder effect using numerical simulations

4.1 Methods

The current study builds on previous developed Pseudo-2D electrochemical model in chapter 2 and expands our understanding of electrode degradation by using updated simulation parameters with different composition ratio among active material, carbon black and PVDF binder in $LiMn_2O_4$ composite electrode. In addition, key parameters such as the surface area, electronic conductivity, and the amount of manganese ions were measured and included in our simulations in an effort to better understand these phenomena. However, this work only considered the active material loss due to Mn dissolution .The effect of side reactions and degradation of electrode due to Mn dissolution considered in chapter 2 was neglected in this work.

4.1.1 **Experiment methods**

4.1.1.1 Sample Preparation

Fresh $LiMn_2O_4$ composite electrodes were made from $LiMn_2O_4$ electrochemical grade powder (Sigma-Aldrich), carbon black (TIMCAL) and PVDF (Kureha KF 7208) binder with different weight ratio among them. They were mixed together using Speedo Mixer (FlackTek Inc.) for 30 minutes. The mixed slurry was coated on a thin aluminium foil and dried in a vacuum at 100 ℃ for 24 hours, then transferred into an Ar-filled glove box without exposure to ambient air.

Table 4.1 shows different samples with different composition of the active material, carbon black and PVDF binder. Total 11 samples were prepared. First 4 samples have same amount of active material (85 %) but the ratio between carbon black and PVDF was changed from 1:1 to 0.4:1. Next four samples also have the same amount of active material (90%) with different ratio of CB/PVDF accordingly. By using these 8 samples we can compare three different composition factors depending on the materials.

In addition, sample 9, 10 and 11 has twice the amount of active material, carbon black and PVDF binder compared to the sample 1, respectively. The effects of each component on cell parameters and performance with respect to the absolute amount of each component (not the composition ratio) can be compared using sample 1,9,10 and 11.

Next, $LiMn_2O_4$ positive electrodes were assembled to sealed 2032 type coin cells (MTI) with a Lithium foil (Alfa Aesar) counter and reference electrodes with a separator (Celgard 2320). Formation cycling was performed three times at C/10.

Sample number	Active Material(g)	Carbon Black(g)	PVDF binder(g)	Ratio of Active material: Carbon Black :PVDF (CB:PVDF)
1	1.7	0.15	0.15	85:7.5:7.5 (1:1)
2	1.7	0.1333	0.1667	85:6.67:8.33 (0.8:1)
3	1.7	0.1125	0.1875	85:5.63:9.38 (0.6:1)
4	1.7	0.0857	0.2143	85:4.29:10.71 (0.4:1)
5	1.8	0.1	0.1	90:5:5 (1:1)
6	1.8	0.0889	0.1111	90:4.44:5.56 (0.8:1)
7	1.8	0.075	0.125	90:3.75:6.25 (0.6:1)
8	1.8	0.0571	0.1428	90:2.86:7.14 (0.4:1)
9	3.4	0.15	0.15	91.89:4.05:4.05 (1:1)
10	1.7	0.3	0.15	79.07:13.96:6.97 (2:1)
11	1.7	0.15	0.3	79.07: 6.97: 13.96 (1:2)

Table 4.1 Cathode electrode sample ratio among active material, carbon black and PVDF binder. Total 8 samples of the electrodes were prepared.

Sample	slope(V/mA)	Coating thickness(inch)	resistance(ohm*cm)	conductivity(S/m)
1	0.1767	0.001	2.034	49.15 ±5.1
2	0.4195	0.001	4.829	20.70 ±2.3
3	0.498	0.0012	6.879	14.53 ±1.1
4	3.664	0.001	42.18	2.370 ±0.2
5	0.1958	0.0015	3.381	29.57 ±3.2
6	1.266	0.0007	10.20	9.802 ±0.9
7	0.7353	0.003	25.39	3.937 ±0.4
8	5.881	0.001	67.70	1.477 ±0.2

Table 4.2 Conductivity measurements with different composition ratio of $LiMn_2O_4$ composite electrode samples

4.1.1.2 Measurement of electronic conductivity

The conductivity of a composite electrode is measured using four point probe method. In order to measure the conductivities of the different ratios of active material, carbon black and PVDF binder, the mixed slurries of composite electrode were pasted on the heat resistant glass substrate. Slurries were dried in a vacuum at 100 °C for 24 hours. Four point probe dc method was applied into the composite electrode on the glass substrate directly using EC-lab VMP3 Biologic potentiostat. Voltage difference was measured from inner two probes and the current was supplied and extracted from outer two probes. The electronic conductivity of the composite electrode was calculated [8] as

$$\sigma = \frac{\ln(2)}{\pi t}\left(\frac{I}{V}\right) = \frac{0.221}{t}\left(\frac{I}{V}\right) \tag{4.1}$$

4.1.1.3 Electrochemical measurements

Capacity was measured using $LiMn_2O_4$ composite electrode/lithium half-cells with C/2 from 3.5V to 4.5V for 30 cycles.

Electrochemical Impedance Spectroscopy (EIS) measurements were performed to measure impedance change due to the different ratio among active material, carbon black and PVDF binder. Each concentration of manganese was measured with EIS at different voltages (3.5, 3.7, 3.9, 4.1 and 4.3 V). Before conducting EIS measurements, the cells were rested in the Open Circuit Voltage (OCV) condition for 2 hours to stabilize for accurate measurement. AC impedance spectra were obtained by applying sinusoidal waves with an amplitude of 5 mV over frequencies ranging from 100 kHz to 10 mHz.

4.1.2 **Simulation methods**

In order to investigate the changes in cell performance with different ratio of active material, carbon black and PVDF binder, numerical simulations were implemented. Different carbon black and PVDF ratio will influence different parameters such as the electronic conductivity, interfacial resistance and manganese dissolution rate of the electrode. Using the electronic conductivity measurements, electronic conductivities of different samples were estimated. Manganese dissolution rate was measured using ICP-OES. Interfacial resistance was measured using Electrochemical Impedance Spectroscopy (EIS). These parameters are transferred into the numerical simulation developed in Chapter 2 which can predict battery performance with more accuracy since these parameters also influence other parameters simultaneously.

Interfacial resistance change due to PVDF binder was considered in the simulation by using equation (4.2). If we measure the charge transfer resistance at same voltage, only reaction rate constant k_0 changes in the equation. It is hard to achieve the exact value of each parameter in the experiment, relative charge transfer resistance ratio is used to provide the relative value in the simulation. In this equation (4.2), R is a gas constant, T is temperature, n_e is the number of electron exchange, F is Faraday's constant, c_{max} is the maximum solid phase concentration, k_0 is a reaction rate constant and x is the intercalation level.

$$R_{ct} = \frac{RT}{{n_e}^2 F^2 c_{\max} k_0 (M_{Li^+})^{0.5} (1-x)^{0.5} x^{0.5}} \tag{4.2}$$

4.2 Results

4.2.1 **Experiment results**

4.2.1.1 Four point probe conductivity measurements

Table 4.2 shows the electronic conductivity measurements of $LiMn_2O_4$ composite electrode samples with different ratio of active material, carbon black and PVDF binder. It can be clearly seen that the conductivity of the electrode significantly varied among the different samples. For example, the sample 1 has more than 30 times higher electronic conductivity compared to the sample 8. These results mainly come from the amount of carbon black in the composite electrode. Electronic conductivity of $LiMn_2O_4$ is only about 0.2 $x10^{-6}$ ~$2x10^{-6}$, the conductivity of overall composite electrode is highly dependent on the amount of carbon black [9-11].

4.2.1.2 Manganese dissolution due to different PVDF/C ratio

Figure 4.1 shows the amount of dissolved manganese ions in the electrolyte with different ration of active material, carbon black and PVDF binder. Higher ratio of carbon black to PVDF binder in the electrode causes more Mn dissolution. Moreover, the amount of dissolved manganese ions increases considerably when active material is 90% compared to 85%. This means that the amount of carbon black is more influential factor than the amount of active material on manganese dissolution in the composite electrode.

4.2.1.3 Interfacial resistance due to different PVDF/C ratio

In addition to manganese dissolution and electronic conductivity change, interfacial resistances also change significantly due to different ratio of PVDF and carbon black. Figure 4.2 shows the EIS spectra with different amount of active material and C/PVDF ratio. When active material is 90% and C/PVDF ratio is 0.4, the impedance of the electrode significantly increased compared to other samples due to the imbalance of the amount of active material, carbon black and PVDF. Because the amount of PVDF was too much compared to the amount of carbon black, electronic conductivity of the composite electrode was significantly decreased.

In order to track the changes of impedance more thoroughly, the interfacial resistance changes in Figure 4.2 were extracted as shown in Figure 4.3. As the voltage goes higher, the interfacial resistance tends to become smaller due to the effect of the decrease of hopping length governed by the decrease of the numbers of electron carriers.

When active material is 90% and C/PVDF ratio is 1, impedance was smallest among different ratio of C/PVDF samples. This result indicates that the ratio of C/PVDF contributes more to increase the total resistance than the amount of the active material. Moreover, impedance of the cell increased more with smaller PVDF/C ratio when there is the same amount of active material (85%). It means that interfacial resistance increased when the amount of PVDF is increased. Thus, interfacial resistance is mostly influenced by the amount of PVDF whereas manganese dissolution is affected by the amount of carbon black. The amount of dissolved manganese and interfacial resistance value due to different components of the electrode will be transferred to the numerical simulations.

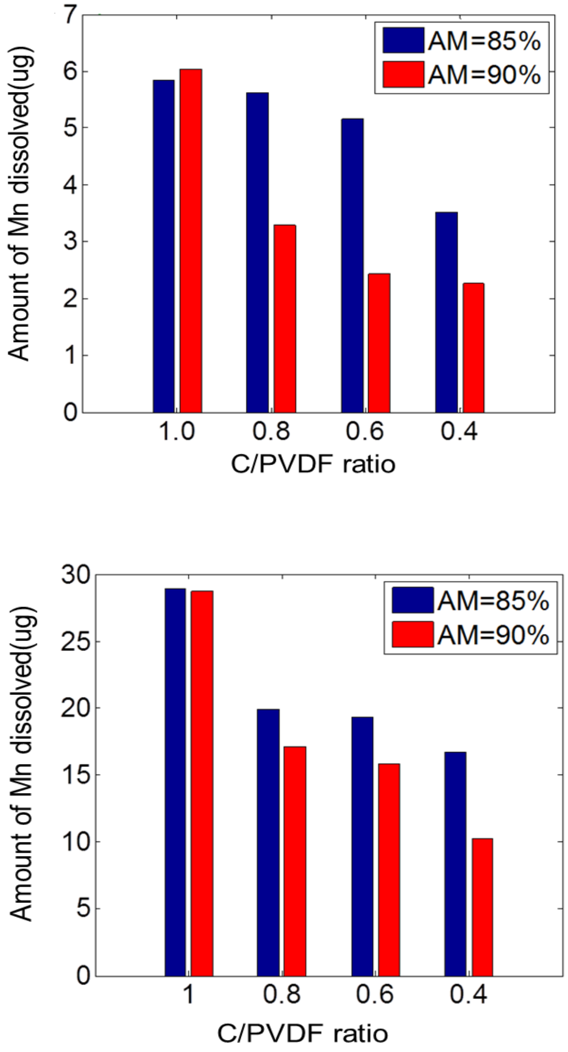

Figure 4.1 the amount of manganese dissolved in the electrolyte with different C/PVDF ratio after (a) 15 cycles and (b) 50 cycles

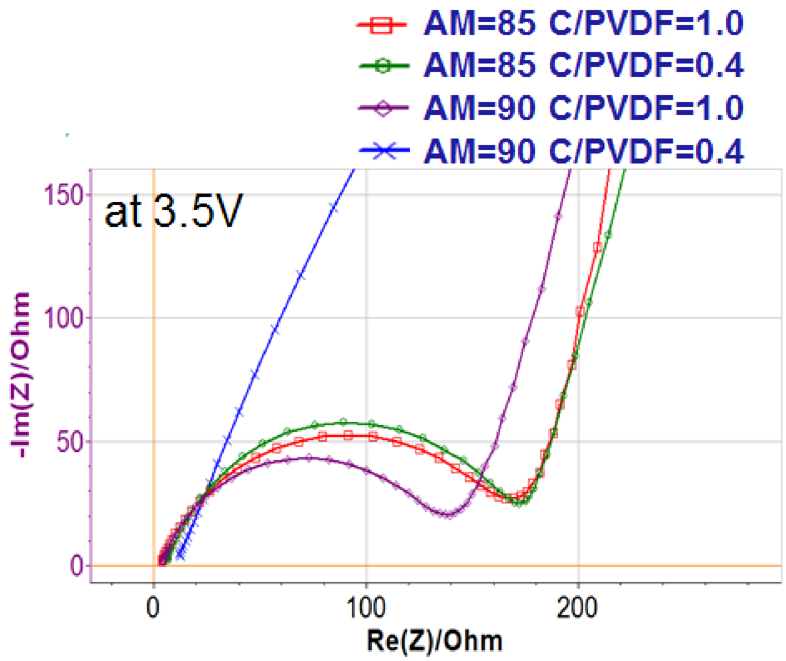

Figure 4.2. EIS spectra with different C/PVDF ratio

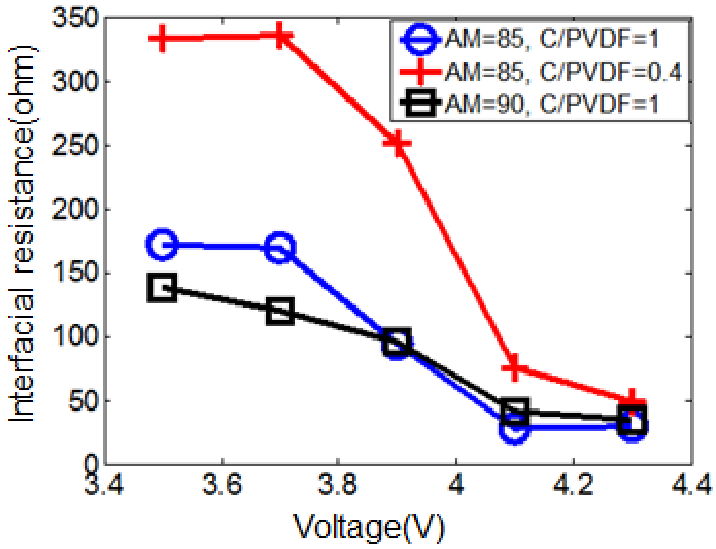

Figure 4.3 interfacial resistance change with different voltage and AM, PVDF/C ratio

4.2.1.4 Simulation results due to different PVDF/C ratio

Figure 4.4 shows the capacity change with increasing cycle number with different PVDF/C ratio considering electronic conductivity, manganese dissolution and binder effect. In order to understand the effect of each parameter, only the effect of electronic conductivity and manganese dissolution was considered in Figure 4.4(a). Since the manganese dissolution accelerates with time, the capacity will decrease as the cycle number increases. Thus, the higher ratio of carbon black to PVDF causes more capacity decrease as cycle number increases. As can be seen in Figure 4.4(a), the slope of the line is steeper when the amount of carbon black is increased in the electrode.

Due to the different conductivity of the electrode, the initial value of the capacity slightly changed. However, the electronic conductivity itself does not affect too much on the capacity since the electronic conductivity is large enough even though the electronic conductivity is minimum. On the other hand, the changes in resistance due to different PVDF/C ratio influences on the capacity significantly. Figure 4.4(b) shows the capacity change due to different C/PVDF ratio of the electrode considering manganese dissolution, impedance and electronic conductivity. It can be seen that capacity decreases as the amount of binder increases, up to 10% decrease of the capacity in the case of C/PVDF = 0.4 compared to the C/PVDF is 1. This result indicates that interfacial resistance is important factor which determines the initial capacity of the system. However, as the cycle number increases, the capacity decreased more rapidly when there is more carbon black in the composite electrode. Moreover, this work only considered the active material loss due to Mn dissolution. If the effect of side reactions and degradation of electrode due to Mn dissolution are considered in this simulation, the capacity decrease of the cell will be more significant. Thus, it is important to consider the side reactions of the battery system especially during long-term cycling.

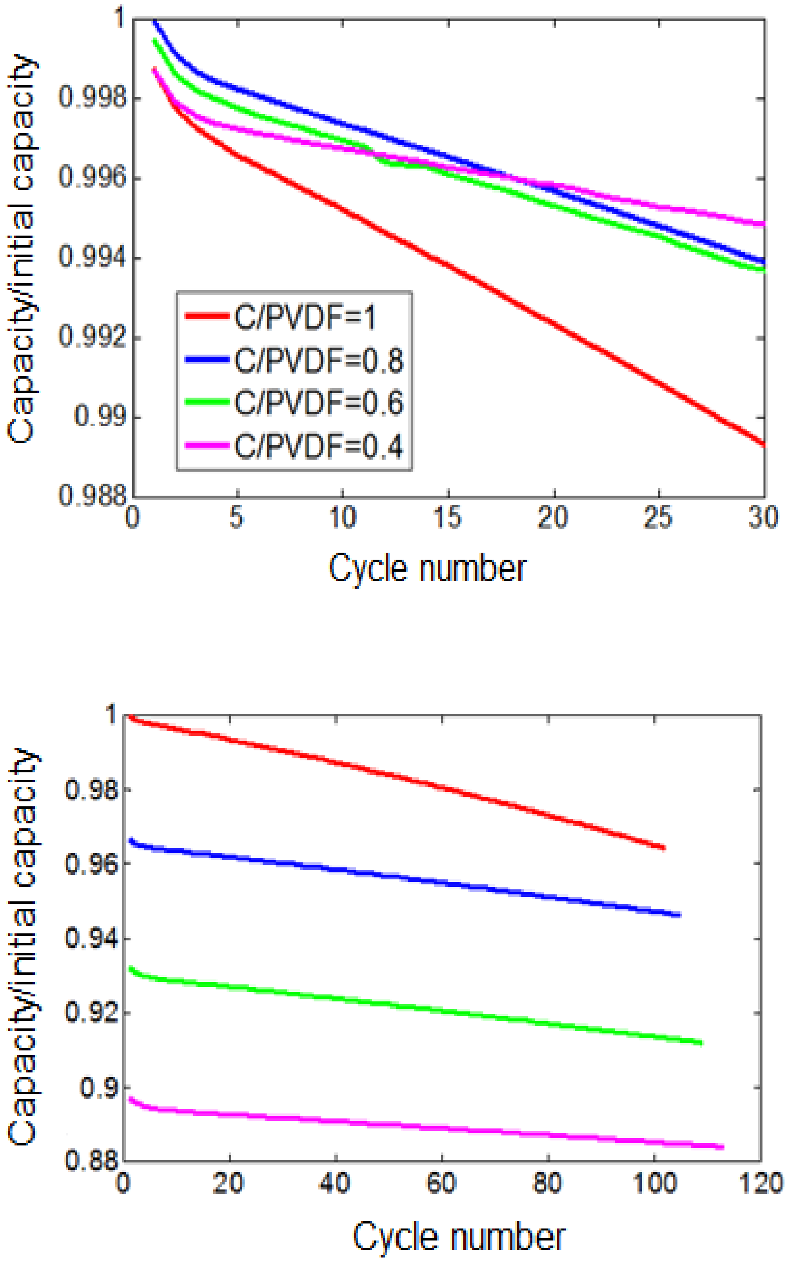

Figure 4.4 Capacity change with cycle number with different C/PVDF ratio when considering parameters of (a) electronic conductivity and Mn dissolution and (b) electronic conductivity, Mn dissolution and binder effect

4.2.1.5 Experiment results due to different PVDF/C ratio

In order to validate the simulation results, experiments are also performed with different C/PVDF ratio. Figure 4.5 shows the voltage profile with different C/PVDF ratio within the same amount of active material in the electrode. It can be seen that ohmic drop of the profile is significantly larger when C/PVDF ratio is 0.4 compared to C/PVDF ratio is 1 due to the higher resistance of the binder effect.

Figure 4.6 shows the changes in the discharge capacity of the $LiMn_2O_4$ composite electrode with cycle number. The trend of the capacity profile from the experiment is similar to the simulation results which can be seen in Figure 4.4(b). From the experiment results, a sample with C/PVDF ratio =0.8 shows the best performance among other samples. The major difference between simulation and experiment results is the initial value of capacity of C/PVDF is 1 and 0.8 in Figure 4.6. The initial capacity of the sample with C/PVDF=1 was largest in the simulation whereas the initial capacity of sample with C/PVDF=0.8 was largest in the experiment. This discrepancy may be originated from the estimation of the relative charge transfer value, which should be different with the real experiment value.

The initial capacity of the electrode is governed by the electronic conductivity and interfacial resistance. Initial capacity significantly decreased when C/PVDF ratio is 0.4 due to the ohmic drop of the cell. Higher ratio of polymer binder to conductive additives increases the interfacial resistance by ion- blocking effect at higher binder contents in the electrode. However, initial capacity also slightly decreased when C/PVDF ratio is 1. If there is too much carbon black in the composite electrode compare to the PVDF binder, it is not sufficient to cover all the active material and carbon black.

The slope of the capacity is mainly influenced by the manganese dissolution. It can be also seen that the slope of the capacity decrease is steeper at higher C/PVDF ratio due to Mn dissolution. Higher amount of carbon black increases the utilization and power performance of the electrode, but also increases dissolution of the manganese and other side reactions. These results show that there is a trade-off among the amount of carbon black, conductive additives and active material. It is important to find an optimal ratio of C/PVDF/active material to maximize the battery capacity.

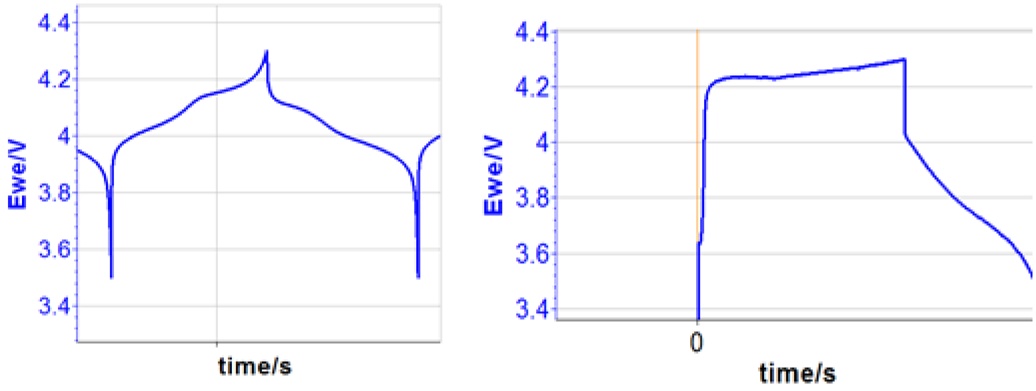

Figure 4.5 Voltage profile of LiMn$_2$O$_4$ composite electrode with (a) active material is 90% and , C/PVDF is 1 and (b) active material is 90% and , C/PVDF is 0.4

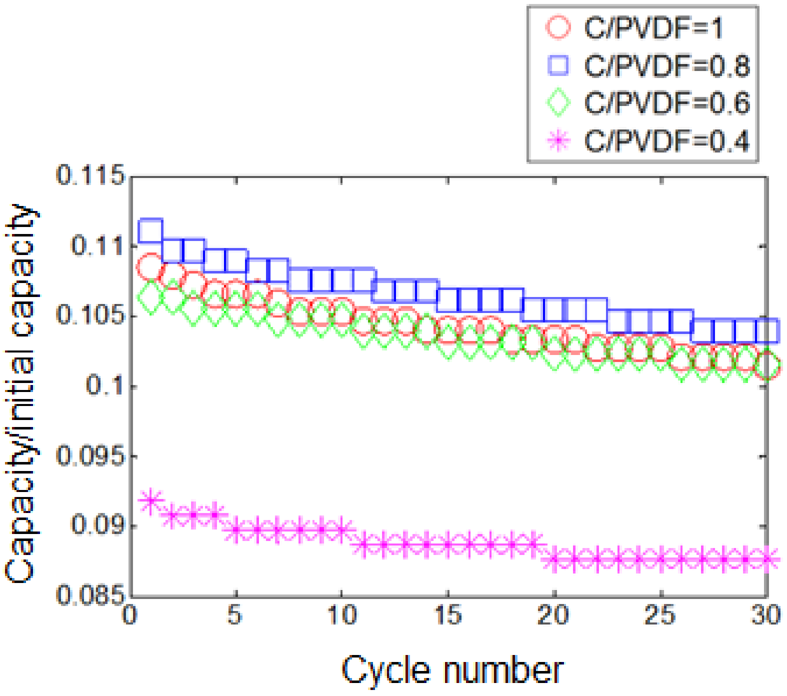

Figure 4.6 Capacity change with cycle number with different C/PVDF ratio

4.3 Conclusions

Active material, conductive additives and binder effect of composite electrode on battery performance was investigated using various experiments such as conductivity measurement, EIS, capacity measurements and computational techniques. It is found that higher ratio of polymer binder to conductive additives increase the interfacial resistance. Moreover, increase in carbon contents of the electrode results in increase of dissolved manganese ions from the $LiMn_2O_4$ composite electrode. Carbon-dependent dissolution rate and PVDF-dependent resistance were observed, which implies that these factors should be considered for optimize the battery performance. Pseudo 2D electrochemical model was updated with measured parameters such as conductivity, dissolution and impedance. Cell performance changes with different component ratio of active material, carbon black and PVDF binder from the simulation results show the similar trend with the experiment data. Also, manganese dissolution becomes important as cells cycle longer due to the accumulation of dissolution. At initial cycle, our simulation predicted that difference of the discharge capacity was up to 10% in the case of C/PVDF = 0.4 compared to the C/PVDF is 1. This difference is mainly originated form the difference in interfacial resistance among different samples. However, the capacity difference is narrowed to 8 % after 100 cycles due to the Mn dissolution. Therefore, composition ratio among active material, carbon black and PVDF binder in $LiMn_2O_4$ composite electrode is the critical factor that determines the battery performance. By considering all these major parameters that influence the cell performances, investigation of optimal ratio of the constituents will be performed in the future.

BIBLIOGRAPHY

[1] P. Arora, R.E. White, M. Doyle, Journal of The Electrochemical Society, 145 (1998) 3647-3667.

[2] T. Marks, S. Trussler, A.J. Smith, D. Xiong, J.R. Dahn, Journal of The Electrochemical Society, 158 (2011) A51-A57.

[3] D.H. Jang, Y.J. Shin, S.M. Oh, Journal of The Electrochemical Society, 143 (1996) 2204-2211.

[4] Y.H. Chen, C.W. Wang, X. Zhang, A.M. Sastry, Journal of Power Sources, 195 (2010) 2851-2862.

[5] S. Mandal, J.M. Amarilla, J. Ibáñez, J.M. Rojo, Journal of The Electrochemical Society, 148 (2001) A24-A29.

[6] G. Liu, H. Zheng, X. Song, V.S. Battaglia, Journal of The Electrochemical Society, 159 (2012) A214-A221.

[7] G. Liu, H. Zheng, S. Kim, Y. Deng, A.M. Minor, X. Song, V.S. Battaglia, Journal of The Electrochemical Society, 155 (2008) A887-A892.

[8] F.M. Smits, Bell System Technical Journal, 37 (1958) 711-718.

[9] M. Park, X. Zhang, M. Chung, G.B. Less, A.M. Sastry, Journal of Power Sources, 195 (2010) 7904-7929.

[10] J. Molenda, W. Kucza, Solid State Ionics, 117 (1999) 41-46
.

[11] J. Marzec, K. Świerczek, J. Przewoźnik, J. Molenda, D.R. Simon, E.M. Kelder, J. Schoonman, Solid State Ionics, 146 (2002) 225-237.

CHAPTER 5

ELECTRONIC AND BONDING PROPERTIES OF $LiMn_2O_4$ SPINEL WITH DIFFERENT SURFACE ORIENTATIONS AND DOPING ELEMENTS AND THEIR INFLUENCE ON MANGANESE DISSOLUTION

Rechargeable batteries using lithium intercalation compounds as the cathode have been extensively studied during the past decade. However, lithium intercalation compounds exhibit significant capacity fading, especially during long-term cycling or storage at elevated temperatures [1-4]. One of the key mechanisms of Li-ion battery degradation involves transition metal dissolution from the cathode materials [5, 6]. Among the various lithium intercalation compounds based upon transition metals, which include Mn, Ni, Co, Fe, and Zn, those based upon manganese showed the largest amount of metal ion dissolution [7]. Substantial efforts have been made to understand manganese dissolution mechanisms and further improve battery performance.

Manganese dissolution is an interfacial reaction between the electrode and the electrolyte that relies, to a large extent, upon the surface structures and orientations of the materials. To understand the mechanisms of manganese dissolution, it is essential to understand the reactions taking place at the electrode-electrolyte interface. These reactions depend on the stability, structures, and changes in energy at the electrode surface. Accordingly, electrode surface properties and processes of the have been widely studied using both experimental and computational techniques. For instance, the faceting of solid-state reacted $LiMn_2O_4$ powder particles with different orientations was experimentally investigated. [8] TEM analysis showed that (111) planes possess the lowest surface energy among the low-index surface planes. First-principle calculations have been also used to study surface properties of $LiMn_2O_4$ spinel. Benedek et al. investigated the surface energies and oxidation states of $LiMn_2O_4$ spinels with low index surface structures. [9] Karim et al. revisited the calculation of surface properties and found that the (111) surface is the most stable facet by creating a partial inverse spinel arrangement. [10] In addition to surface stability, different surface orientations of the electrode have also been shown to have an effect on Mn dissolution. [11]. Spinel with the (111) plane exposed to the electrolyte solution suffers significantly less degradation than spinel with the (110) plane exposed to the electrolyte solution. [11] However, a clear explanation of the impact of surface orientation on manganese dissolution is still missing from the previous studies. Investigating the impact of surface orientation on Mn dissolution will broaden our understanding of Mn dissolution.

Preventing or minimizing manganese dissolution is important to improve the performance of this material. Doping with elements that can be substituted by manganese ions is known to be an effective way to prevent manganese dissolution. Various metals, such as Al, Co, Cr, Cu, Fe, Mg, and Ni [12-24], were partially substituted by manganese to prevent the dissolution of manganese. Previous studies have found that the introduction of cations with low oxidation number increases the oxidation state of Mn ions. [25-27] When the oxidation number of the Mn ions in the $LiMn_2O_4$ spinel increases, the overall concentration of Mn^{3+} ions decreases. This phenomenon seems to prevent the Jahn-Teller distortion and disproportionation reactions of unstable Mn^{3+} ions by reducing the concentration of Mn^{3+} ions; this eventually reduces Mn dissolution. Techniques like this have significant success when all of the Mn on the cathode surface is tetravalent [28]. Alternatively, one can also create a nonstoichiometric spinel in which Mn ions are replaced by Li (i.e. $Li_{1+\delta}Mn_{2-\delta}O_4$). This has the same effect of increasing the overall Mn valence. This method has also been shown to increase stability in the higher voltage region [29]. However, doping with other metal ions, such as Y^{3+} [30, 31], showed behavior that was the opposite of that seen with other elements. Although doping with yttrium can electrochemically activate manganese to increase its specific capacity, it also promotes dissolution of manganese into the electrolyte. [30] Apparently, doping the structure with elements of low oxidation number is not the only technique that can be used to decrease Mn dissolution. Kim et al. claimed that Mn dissolution is also strongly correlated with the covalent nature of the Mn-O bond [32]. To further understand why doping with certain elements decreases manganese dissolution, a detailed analysis of the electrode's electronic properties in the presence of different doping elements should be investigated.

In summary, the current research investigates the effect of surface orientation and doping on the dissolution of Mn ions from $LiMn_2O_4$ structures using first-principle calculations. The aim of our current research is to understand why certain surface orientations and element dopings more effectively prevent manganese dissolution. By calculating the electronic and bonding properties of electrodes with different surfaces and dopings, manganese dissolution mechanisms and their prevention can be more fully understood. Specifically, this study conducts a thorough investigation of the changes in surface stability, manganese oxidation state, enthalpy of formation (EOF) of manganese vacancies, electronic properties and bonding properties of electrodes with different surface orientations and element dopings. The calculation results are then validated and compared with previous calculations and experimental results.

5.1 Methods

First-principle electronic structure calculations were performed within the generalized gradient approximation (Perdew-Wang 91 parameterization of the exchange correlation potential) plus U (GGA +U) implementation of density functional theory. The Vienna *ab initio* simulation package [33] plane-wave pseudopotential code was used with the projected augmented wave (PAW) method. A plain cutoff energy of 600 eV was used in this study to ensure good convergence during cell parameter relaxations. A U value of 4.84 eV was chosen for the Mn atoms.

5.1.1 **Surface structure of $LiMn_2O_4$**

Benedek et al. [9] adopted low-index surface terminations to simulate the surface structure in their $LiMn_2O_4$ model. In this study, a similar approach was used to create a $LiMn_2O_4$ surface structure model. Three $LiMn_2O_4$ surface models with different orientations [(001), (110) and (111)] were constructed. Given the variety of terminations that are possible, we only considered the common features of $LiMn_2O_4$ surfaces with low index numbers. Within each orientation of the surface, different terminations of atoms on the surface are also possible. For instance, the (110) orientation of the $LiMn_2O_4$ structure has 2 different planes, which consist of a MnO_2 slab and a $LiMnO_2$ slab, occupied in turn. Therefore, two different terminations are available in the (110) orientation. The energy required to break the bond from each MnO_2 and $LiMnO_2$ termination should be different because they have different atoms and because bonds are present near them. Similarly, we adopted Mn_4O_8 and Li_2 terminations in the (001) orientation and Mn, Mn_3 and O_4 terminations of the (111) orientation. By considering different surface atom terminations, a total 7 $LiMn_2O_4$ surface slab models were built in this study. Ideal stoichiometry was maintained by transferring atoms from one surface of the slab to the opposite surface. A vacuum slab was placed on the both sides of the $LiMn_2O_4$ slab structure for the relaxations.

In addition to different surface orientations and terminations, the ferromagnetic (FM) and antiferromagnetic (AFM) orderings of manganese atoms were also considered. There are two possible magnetic orderings to achieve anti-ferromagnetism within the spinel manganese oxides [34]: AFM ordering with (001) and (110) directions. The AFM arrangement with (110) direction was adopted in this work because it has been reported that the AFM ordering of (110) direction has slightly lower energy than AFM ordering of (001) direction.

5.1.2 **Element (Co, Cu, Cr, Fe, Mg Ni and Sn) Doping on $LiMn_2O_4$**

Figure 5.1 shows the element-doped $LiMn_2O_4$ structure with (001) surface orientation. Doping elements (Co, Cu, Cr, Fe, Mg, Ni and Sn) replaced Mn atoms between other two Mn atoms. The changes in electronic and bonding properties of the Mn atoms were investigated by placing different doping elements between them. The $LiM_{0.25}Mn_{1.75}O_4$ stoichiometry of the doped structure was maintained. In this study, changes in average intercalation voltage, oxidation state of manganese, and bonding properties due to doping with different elements (Co, Cu, Cr, Fe, Mg, Ni and Sn) were investigated using first-principle calculations.

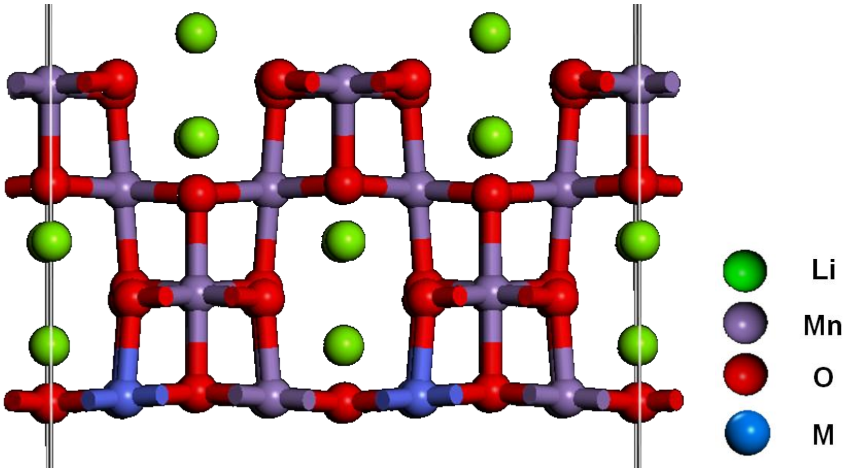

Figure 5.1 element (M= Co, Cu, Cr, Fe, Mg, Ni and Sn) doped-$LiMn_2O_4$ structure with (001) surface orientation

5.2 Results

5.2.1 **Surface orientations/terminations of $LiMn_2O_4$**

5.2.1.1 Surface energy change with different orientations

The surface energy quantifies the breakdown energy of molecular bonds in the cleaved materials. The surface energy can also be defined as the additional energy generated at the surface of a material compared with that of the bulk material when surfaces are newly generated. Accordingly, surface structures with smaller surface energies are more stable. Thus, the relative stabilities of surfaces with different orientations and structures can be derived by comparing the differences in their surface energies. The surface energy σ, can be computed as

$$\sigma = \frac{[E_{slab} - NE_{bulk}]}{2A} \tag{5.1}$$

where E_{slab} is the energy of the slab supercell, E_{bulk} is the bulk energy per atom, N is the number of atoms and A is the cleavage area of the slab structure.

The surface energies of different orientations/terminations of $LiMn_2O_4$ slab model was calculated using equation (5.1). Table 5.1 shows the surface energies of different orientations and terminations in both the FM and AFM slab structures after relaxation. The surface energy of the each slab structure can be used as a measure of its relative stability, which determines the probable form of structures within the same orientation. For example, lithium terminations in the (001) structure will be a more likely structure than manganese or oxygen terminations because its surface energy is critically lower than that of the other terminations. Among the 7 different surface terminations and orientations, the surface structures of (001)_Li_2, (110)_M_4O_8, and (111)_Mn have the smallest surface energy within the same orientations for both FM and AFM structures.

The surface energies of the different surface structures are similar to those reported in the literature [9], except for the (111)_Mn_3 structure, as shown in Table 5.1. The surface energy of the (111)_Mn3 structure is dramatically changed compared with those of the other structures. Discrepancies between the literature values and the results of our calculation of the (111) surface energy probably come from the surface reconstruction that occurs during relaxations. Our calculations show an intensive reconstruction of the (111) surface during relaxations. These results are consistent with previous findings that Mn-terminated (111) surfaces experience surface reconstruction during relaxations [9, 10]. Benedek et al. [9] found that the Mn-terminated (111) surface structures undergoes extensive migration of Li and O atom from the bulk to the surface, as well as stoichiometric mixing of the Li, Mn and O components. Karim et al. [10] also studied the reconstruction of (111) orientations with relatively high surface energy; they claimed that reconstruction is an indication of the inherent instability of the (111) surface. Karim et al. [10] also found that the (111) surface becomes more stable when employing local cation inversion at the (111) surface. In this work, surface reconstructions were also found in (111) surfaces with relatively high surface energy. However, the surface energy is higher than those from previous reports, displayed in Table 5.1. Due to intensive reconstruction, the final relaxation structures and their corresponding energy states might be changed during relaxations. Smearing methods, width of smearing, and other computational methods may influence the final relaxation structures and their corresponding energy states.

The surface energies of $LiMn_2O_4$ structures with FM and AFM ordering are also similar, except for surface structures with (111) orientations. The reconstruction of (111) surfaces results in surface energies for surfaces with FM ordering that are different than those of surfaces with AFM ordering, after relaxation. The spin configuration of the surface structure may influence the surface energy of each of the terminations and orientations, which results in differences in surface energy between FM and AFM structures.

5.2.1.2 Changes in formation energy of manganese vacancy with different orientation (Mn)

The manganese vacancy formation energies of were calculated using the $LiMn_2O_4$ surface slab model with different orientations/terminations. Different terminations of the $LiMn_2O_4$ structure have different atoms present on the surface. The energy required to break a bond from each termination should be different because they have different numbers of atoms and because bonds are present near them. The energy needed for manganese atoms to break free from the structure can be calculated using the manganese vacancy formation energy, as described in equation (5.2):

$$E_F = \frac{1}{m}(E[Li_N Mn_{2N-M} O_{4N}] - NE[LiMn_2O_4]) + \mu_{Mn} \tag{5.2}$$

where E_F is the manganese vacancy formation energy, N is the number of chemical formulas in the system, M is the manganese deficiency number and μ_{Mn} is the chemical potential of manganese. The nearest Mn atom was terminated in order to calculate the minimum energy caused by the vacancy of a manganese atom.

Surface structure	Surface energy of Ferromagnetic Ordering (J/m^2)	Literature value of surface energy for Ferromagnetic ordering ([9],[10]) (J/m^2)	Surface energy of Antiferromagnetic ordering (J/m^2)
(001)_Li_2	0.554	0.58, 0.87	0.601
(001)_Mn_4O_8	1.199	0.98,1.28	1.229
(110)_$LiMnO_2$	1.233	0.99,1.39	1.248
(110)_MnO_2	1.162	1.19,1.52	1.155
(111)_Mn	0.834	0.85,N/A	0.898
(111)_Mn_3	1.682	1.29,1.18	1.625
(111)_O_4	1.201	1.30,N/A	1.537

Table 5.1 Surface energy of different surface structures of $LiMn_2O_4$ in AFM and FM ordering

	Formation energy of manganese vacancy with Ferromagnetic ordering(eV)		Formation energy of manganese vacancy with Antiferromagnetic ordering(eV)	
Surface structure	not relaxed	relaxed	not relaxed	relaxed
(001)_Li_2	13.399	13.507	13.38	14.006
(001)_Mn_4O_8	9.448	15.013	9.175	10.233
(110)_$LiMnO_2$	9.033	12.047	10.628	9.185
(110)_MnO_2	12.657	6.612	13.470	5.161309
(111)_Mn	8.377	8.578	8.392	8.290
(111)_Mn_3	2.630	8.0547	11.592	9.162
(111)_O_4	11.261	10.565	10.565	11.185

Table 5.2 Formation energy of manganese vacancy with different surface structures of $LiMn_2O_4$ with AFM and FM ordering

The formation energies and electronic structures of defects in oxygen-deficient $LiMn_2O_4$ were previously investigated to determine the preferred defect types in $LiMn_2O_4$ structures. [35] Simple oxygen vacancies in the $LiMn_2O_4$ structure were found to exhibit the lowest formation energy among the oxygen-vacancy-type defects. Similarly, the formation energies of simple Mn vacancies in $LiMn_2O_4$ with different surface structures were investigated in this study.

By comparing the manganese vacancy formation energies of different surface orientations, the orientation/termination that is more likely to contribute to manganese dissolution by a breaking bond from the structure can be determined. Table 5.2 shows the manganese vacancy formation energies of $LiMn_2O_4$ with AFM and FM ordering having different surface structures. To compare the different manganese vacancy formation energies within the different orientations, the smallest surface energy within the same orientations was chosen to compare with the others. From previous surface energy calculations, the surface structures of (001)_Li_2, (110)_M_4O_8, and (111)_Mn have the smallest surface energy in the same orientations for both FM and AFM structure among the 7 different surface terminations and orientations.

Among FM surface structures, the manganese vacancy formation energies of (001)_Li_2, (110)_M_4O_8, and (111)_Mn are 13.5 eV, 6.61 eV and 8.57 eV, respectively. Among AFM surface structures, the manganese vacancy formation energies of (001)_Li_2, (110)_M_4O_8, and (111)_Mn are 14.0 eV, 5.16 eV and 8.29 eV, respectively. Among the three different orientations, the manganese vacancy formation energies of the surface structures with FM ordering had values similar to those with AFM ordering. The (110) surface orientation has the smallest manganese vacancy formation energy, whereas the (001) surface has the largest. This result is consistent with the previous TEM results [11] that $LiMn_2O_4$ with the (111) plane exposed to the electrolyte suffers significantly less degradation than $LiMn_2O_4$ with the (110) plane exposed to the electrolyte.

5.2.1.3 Bond length change due to different surface orientations

To understand why certain orientations have smaller dissolution effects and smaller manganese vacancy formation energies, the bonding properties among different surface orientation/terminations were investigated. The number of Mn-O bonds near the manganese atom and the bond lengths of Mn-O bonds change with different surface orientations and different terminations of the structure. In general, the length and strength of the bond are inversely proportional with each other. If bond length decreases, the energy required to break the bond increases. Moreover, if there are additional bonds near the atom, the energy required to break the Mn-O bond also increases. There are different numbers of bonds near the manganese atoms with different terminations and orientations among $LiMn_2O_4$ samples with different surface structures. Moreover, the bond lengths near the manganese atom are uniquely determined by the atom's surroundings and the structure during relaxation. Thus, number of Mn-O bonds and their bond lengths will be uniquely determined by the surface orientation/terminations. The numbers of Mn-O bonds, the average Mn-O bond lengths, and the manganese vacancy formation energies of surfaces with FM and AFM ordering can be found in Table 5.3 and Table 5.4, respectively.

To understand the relationship among manganese vacancy formation energy, bond length, and the number of Mn-O bonds near the manganese atoms in the surface structures, these properties are plotted separately. Figure 5.2 and Figure 5.3 show the relationship among manganese vacancy formation energy, bond length and the number of Mn-O bonds near the manganese atoms in the surface structures with FM and AFM ordering, respectively. At a glance, it seems that there is no conspicuous relationship among the number of bonds, bond length and manganese vacancy formation energy. However, a larger number of Mn-O bonds correlates with higher manganese vacancy formation energy. Moreover, if we compare the manganese vacancy formation energy and bond length in cases containing the same number of bonds, they are inversely proportional to each other. For example, the (001)_Li_2 structure has the highest manganese vacancy formation energy, since the manganese atom has five Mn-O bonds in its vicinity. Surface structures with 4 Mn-O bonds near the manganese atom have smaller manganese vacancy formation energies than surface structures with 5 Mn-O bonds, but higher manganese vacancy formation energies than structures with 3 Mn-O bonds. Among the surface structures with 4 Mn-O bonds, the average bond length near the Mn atom is inversely proportional to the manganese vacancy formation energy. The (111)_Mn_3 structure is an outlier among the surface structures. If it followed the trend, it should have either a larger bond length or smaller manganese vacancy formation energy. The reason for this result comes mainly from surface reconstruction that occurs during relaxation of the (111) structure. Without this exception, the manganese vacancy formation energy seems to be be determined by the number of bonds near the manganese atom and the bond length of each of the Mn-O bonds.

AFM surface structures show a similar trend with different numbers of bonds. Those structures with a larger number of Mn-O bonds near the surface have higher manganese vacancy formation energies, as shown in Figure 5.3. However, the relationship between the bond length and the manganese vacancy formation energy is not as clear as that seen with the FM structures. This is due to the different spin configurations of nearby Mn atoms. The differences in spin configuration affect the Mn-O bond length, which affects the manganese vacancy formation energy. From these results, it can be concluded that the manganese vacancy formation energy changes with different surface orientations and that this change is caused by differing numbers of Mn-O bonds near the Mn atom and the bond length of each bond.

Surface structure	# of Mn-0 bonds	Average Mn-0 bond length(A)	Formation energy of Mn vacancy(eV)
(001)_Li_2	5	1.879	15.013
(001)_Mn_4O_8	4	1.679	13.507
(110)_$LiMnO_2$	4	2.002	12.047
(110)_MnO_2	3	1.960	6.612
(111)_Mn	3	2.192	8.578
(111)_Mn_3	3	1.868	8.0547
(111)_O_4	4	2.344	10.565

Table 5.3 The number of Mn-O bonds, average Mn-O bond length and formation energy of manganese vacancy on the surface with ferromagnetic ordering

Surface structure	# of Mn-0 bonds	Mn-0 bond length(A)	Energy of Mn vacancy(eV)
(001)_Li_2	5	1.869	14.006
(001)_Mn_4O_8	4	1.667	10.233
(110)_$LiMnO_2$	4	2.008	9.185
(110)_MnO_2	3	2.225	5.161
(111)_Mn	3	2.048	8.290
(111)_Mn_3	3	1.660	9.162
(111)_O_4	4	2.114	11.185

Table 5.4 The number of Mn-O bonds, average Mn-O bond length and formation energy of manganese vacancy on the surface with anti-ferromagnetic ordering

5.2.1.4 DOS calculation , distribution with different orientations

To understand the effect of surface orientation on manganese dissolution, first-principle calculation methods were used to calculate the electronic properties of the surfaces. Previous studies have reported that the oxidation state of the manganese ions influences manganese dissolution. [25-27, 32] The oxidation state of manganese is closely related to the number of electrons in the d-orbitals, which consist of the e_g and t_{2g} orbitals. The e_g orbital consists of the d_{x2-y2} and d_{z2} orbitals and the t_{2g} orbital consists of the d_{xy}, $d_{xz,}$ and d_{yz} orbitals. Generally, it is assumed that only 3 electrons inhabit the t_{2g} level in the electronic configuration of an ideal high-spin Mn^{4+} ion. The electronic configuration of an ideal high-spin Mn^{3+} ion is assumed to have only 3 electrons in the t_{2g} orbital and one electron in the e_g orbital. If only one electron is placed in the e_g orbital, that electron is placed in either the d_{x2-y2} or the d_{z2} orbital. Due to the presence of the electron, the degeneracy of the two orbitals breaks down, decreasing the geometric stability and leading to Jahn-Teller distortion. Due to this instability, avoiding the Mn^{3+} state of manganese prevents Jahn-teller distortion, resulting in reduced Mn dissolution. [25-27].

To observe the electronic properties and the oxidation state of the manganese atom, the projected density of state (PDOS) of a manganese atom on the surface was investigated. Comparisons of the PDOSs of Mn atoms in (001)_Li_2, (110)_Mn_4O_8, and (111)_Mn surface structures can be found in Figure 5.4 through Figure 5.7. The “+” and the “-“ signs in these Figures indicate the up and down spin directions of the manganese atoms. Since the oxidation state of the manganese is determined by the d-orbital state with highest energy, only energy changes from -10 to +10 eV are extracted.

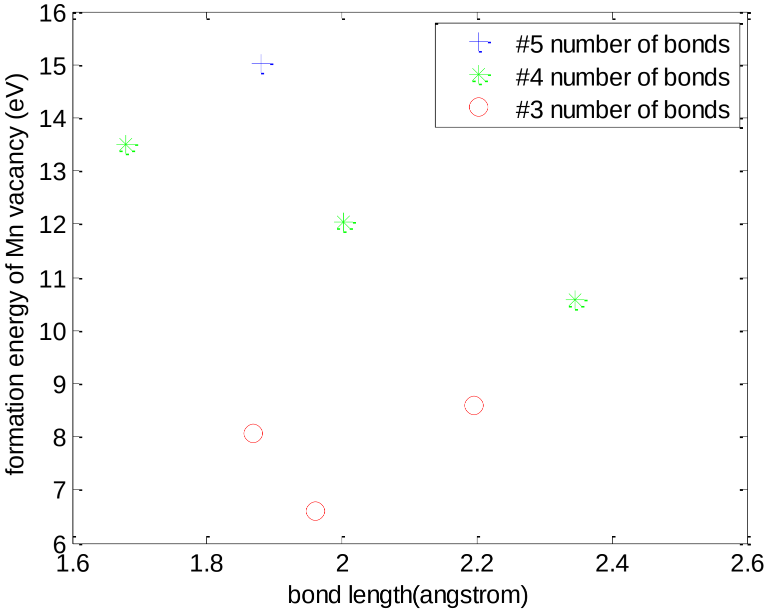

Figure 5.2 Relationship among the number of Mn-O bonds, average Mn-O bond length and formation energy of manganese vacancy on the surface with ferromagnetic ordering

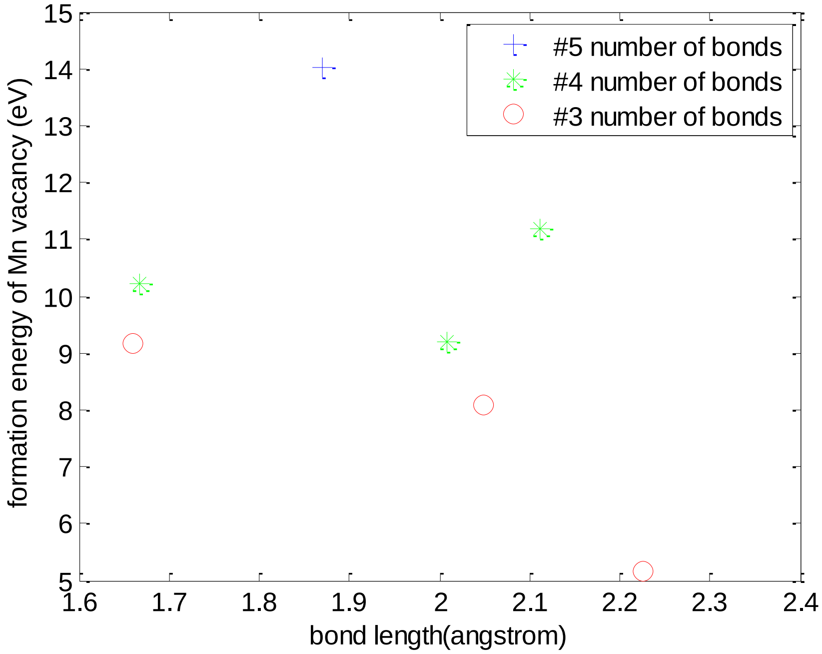

Figure 5.3 Relationship among the number of Mn-O bonds, average Mn-O bond length and formation energy of manganese vacancy on the surface with anti-ferromagnetic ordering

Figure 5.4 Comparisons of t2g orbital in Mn projected DOS among (001)_Li2 , (110)_Mn4O8, and (111)_Mn surface structures

Figure 5.4 compares the complete t_{2g} orbitals of the manganese atoms on the surfaces of three different surface structures. From these results, it can be seen that the up-spin t_{2g} level is fully filled with electrons because it is below the Fermi energy level. Since the t_{2g} orbitals are completely filled with electrons whether the manganese atom has an oxidation number of 3 or 4, the t_{2g} orbitals of different surface structures are not significantly different among them. However, the e_g orbitals from the three different surface structures show different patterns than the t_{2g} orbitals, as shown in Figure 5.5. The DOS of the high state e_g orbitals in the up-spin have splits near the Fermi level with different surface structures. The (001)_Li_2 structure has a peak at the highest energy (near 3 eV) and the (110)_M_4O_8 structure has a peak at the lowest energy state (<-1 eV) among the highest energy peaks. As the energy state of the e_g orbital increases above 0 eV, it will become harder to fill the e_g orbital with electrons. This means that increasing the energy state of the e_g orbital increases the possibility of the existence of a Mn^{4+} state, which will be beneficial for preventing Mn dissolution.

To further investigate the state of the e_g orbital, the DOSs of the d_{x2-y2} and d_{z2} orbitals are plotted separately. Figure 5.6 and Figure 5.7 show the projected DOSs of the d_{x2-y2} and d_{z2} orbitals of the manganese atom. As seen in Figure 5.6, there are no significant differences among the d_{x2-y2} orbitals found in different structures. However, the d_{z2} orbitals found in different structures show dramatic changes in up-spin states. The DOS changes in the d_{z2} orbital come from Jahn-Teller distortions related to elongation. When a molecule possesses a degenerate electronic ground state, it will distort its structure to remove degeneracy and form a lower energy state. Elongation and compression are two ways to remove the degeneracy. When elongation occurs, the axial bond length increases and degeneracy is broken by the stabilization of the d orbitals with a z component. The energies of the d orbitals with a z component (d_{z2}) decrease while the energies of the d orbitals without a z component (d_{x2-y2}) increase. On the other hand, when compression occurs, the axial bond length decreases and the degeneracy is broken by the stabilization of d orbitals without a z component. The energies of d orbitals without a z component (d_{x2-y2}) decrease while the energies of d orbitals with a z component (d_{z2}) increase. From the results of our calculations, it can be seen that the energy of only the d_{x2-y2} orbital increases in all three surface structures. This means that a Jahn-teller distortion related to elongation is present in the surface manganese atom.

The changes in the DOS peak energy state are different among the three different structures. The (001)_Li_2 structure shows a DOS peak at a higher energy state in the up-spin state. In contrast, the (110)_Mn_4O_8 structure has a DOS peak at the smallest energy state in the up-spin state, as shown in Figure 5.6. The relative position of the Mn 3d levels is shifted to a high-energy region in the (001)_Li_2 structure. Since the relative peak position of Mn 3d level in (001)_Li_2 is shifted to the right, above the Fermi level, more energy is needed for an electron to fill the e_g orbital. This implies that more energy is needed to achieve the 3+ oxidation state of manganese. Thus, the (001)_Li_2 surface structure has the lowest possibility to be in the 3+ oxidation state and the (110)_Mn_4O_8 structure has the highest possibility to be in the 3+ oxidation state. These results agree with previous calculations of the manganese vacancy formation energy, which indicate that the (110) orientation is the most vulnerable and the (001) orientation is the least vulnerable to Mn dissolution.

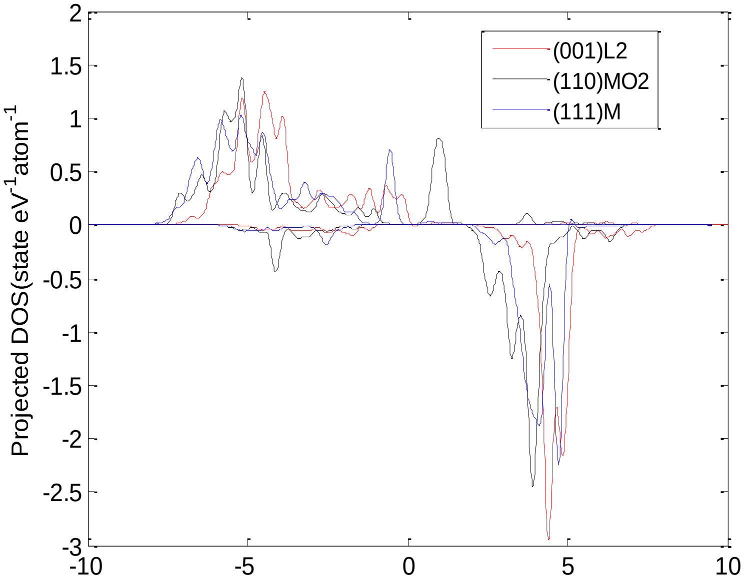

Figure 5.4 Comparisons of t_{2g} orbital in Mn projected DOS among (001)_Li_2 , (110)_Mn_4O_8, and (111)_Mn surface structures

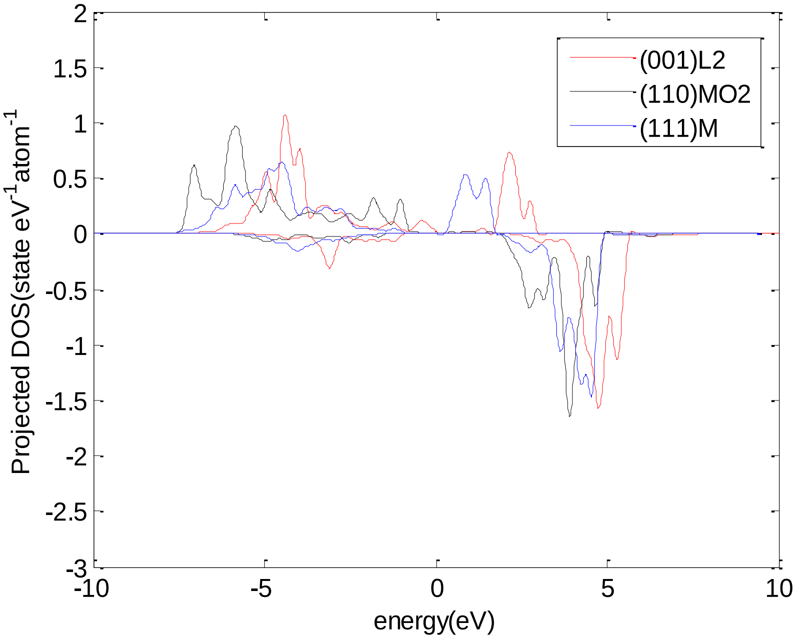

Figure 5.5 Comparisons of e_g orbital in Mn projected DOS among (001)_Li_2 , (110)_Mn_4O_8, and (111)_Mn surface structures

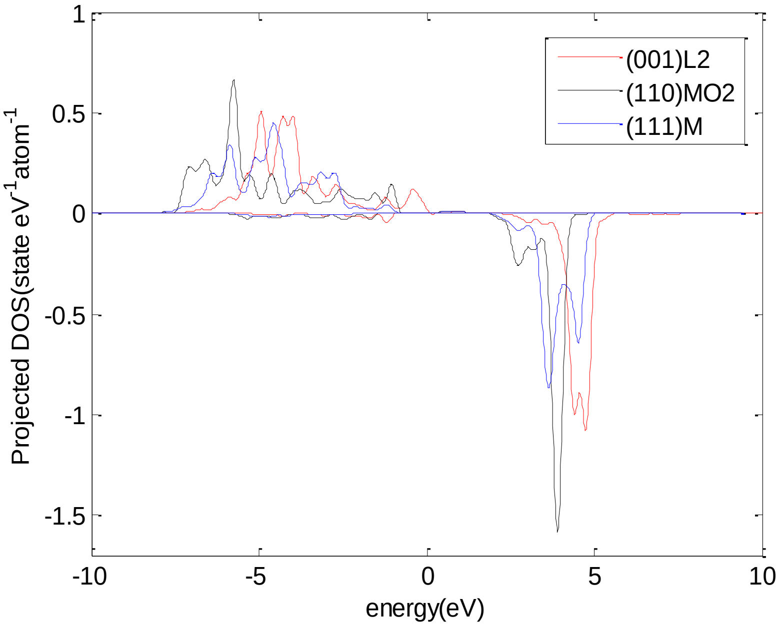

Figure 5.6 Comparisons of d_{z2} state in eg orbital in Mn projected DOS among (001)_Li$_2$, (110)_Mn$_4$O$_8$, and (111)_Mn surface structures

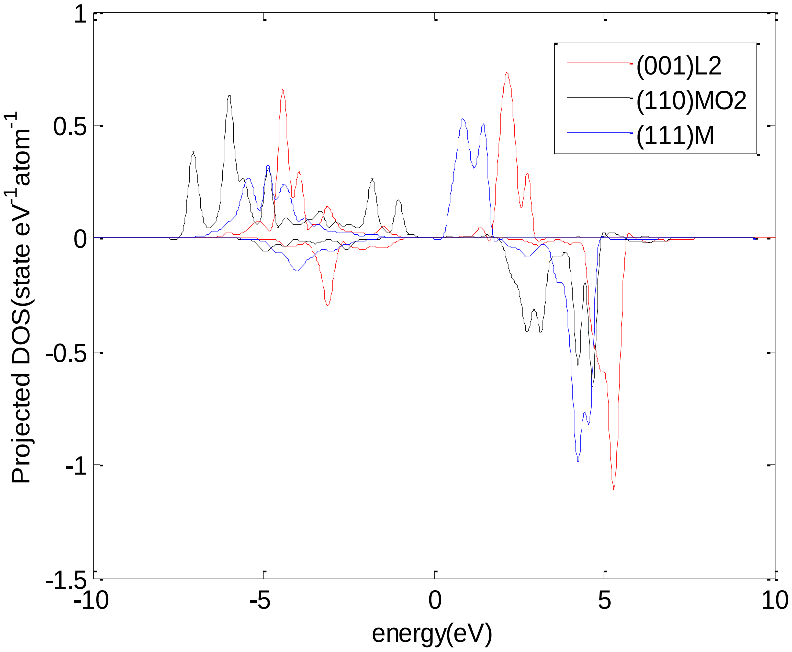

Figure 5.7 Comparisons of d_{x2-y2} state in eg orbital in Mn projected DOS among (001)_Li$_2$, (110)_Mn$_4$O$_8$, and (111)_Mn surface structures

5.2.2 **Element (Co, Cu, Cr, Fe, Mg Ni and Sn) Doping on $LiMn_2O_4$**

To validate the results of our calculations of the structures of element-doped $LiMn_2O_4$s, the average intercalation voltages were calculated after doping with different elements. The average intercalation voltage was calculated from changes in the Gibbs free energy of lithiated and delithiated $LiMn_2O_4$ structures, as shown in Equation (5.3):

$$V = -\frac{G[(LiMn_2O_4)_n] - G[(Li)_{n-z}(Mn2O4)n]}{zF} + \mu(Li) \tag{5.3}$$

where G stands for the Gibbs free energy, n is the number of chemical formulas in the system, z is the amount of lithium extracted from the structure, and μ is the reference chemical potential of the system. The total energies of the fully lithiated and de-lithiated structures were calculated, and then the average intercalation voltages were predicted. Table 5.5 shows the average intercalation voltages for the $LiM_{0.5}Mn_{1.5}O_4$ to $M_{0.5}Mn_{1.5}O_4$ transition (M= Mn, Co, Cr, Cu, Fe, Mg, Ni and Sn) taken from references [12, 14-20, 36-40], from experiments [12, 15, 37, 39, 40] and from the calculations performed in this work. The results clearly show that the values calculated in this work are within the range of those in the references and similar to those taken from experimental results. Since it is more beneficial to operate a battery in the higher voltage region, most doping elements, except for Sn, were favorable in terms of intercalation voltage.

5.2.2.1 Energy change associated with different doping elements

Figure 5.8 shows the average changes in the EOF per atom that result from doping the system with different elements. A positive change in the EOF means that the total energy of the system is increased (endothermic). Conversely, a negative change in the EOF represents a decrease in the total energy (exothermic). These endothermic and exothermic changes that result from doping can be attributed to lattice distortions related to ionic radius differences and vacancy formation [41]. From the results of our calculations, doping with Co, Cr, Fe, and Ni show an increase in the overall energy state of the total DOS, whereas doping with Cu, Mg, and Sn show a decrease in the overall energy state.

The EOF tends to increase as the doping element moves from left to right in the periodic table (Cr, Mn, Fe, Co, Ni and Cu). Table 5.6 shows the changes in EOF per atom and the electronegativities of the transition metal elements. As the atomic number increases, the EOF increases (Cr, Mn, Fe, Co, Ni and Cu). This result is similar to the increasing trend in the electronegativity of the transition metal elements. Since electronegativity is a function of the atom's ionization energy and a positive ionization energy shows endothermic behavior in our system, the increasing trend of the EOF is quite consistent with the increasing trend of the electronegativities. However, doping with Mg or Sn did not follow any specific trend in EOF.

Doping elements	Reference	Experiment results	Calculations in this work
No doping	3.78~4.05V [12, 14, 16, 17, 19, 36]	4V [12]	4.01
Co	3.9~4.2V [17, 37]	4.2 V [37]	4.06
Cr	4.04~4.5V [17, 19, 20, 38]	4.5 V [39]	4.11
Cu	4.15~4.56V [18, 20, 39]	4.45 V [39]	4.50
Fe	3.8~4.28V [17, 19, 40]	4 V [40]	4.24
Ni	4.12~4.8V [15, 17, 39]	4.35 V [15]	4.25
Mg	N/A	N/A	4.79
Sn	N/A	N/A	3.82

Table 5.5 Average intercalation voltage from $LiM_{0.5}Mn_{1.5}O_4$ to $M_{0.5}Mn_{1.5}O_4$ (M= Mn, Co, Cr, Cu, Fe, Mg, Ni and Sn) in references [12, 14-20, 36-40], experiments [12, 15, 37, 39, 40] and calculated values

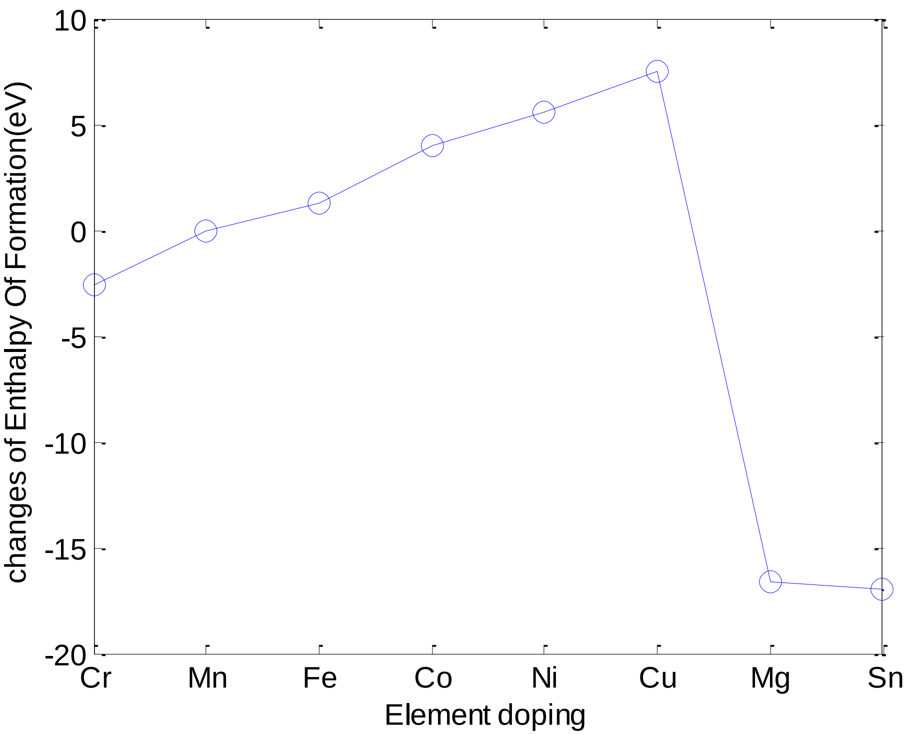

Figure 5.8 Change of enthalpy of formation energy per atom due to different doping elements

atom	Atomic number	change of EOF per atom(eV)	electronegativity(allen scale)
Cr	24	-2.619	1.65
Mn	25	0	1.75
Fe	26	1.315	1.8
Co	27	3.956	1.84
Ni	28	5.547	1.88
Cu	29	7.496	1.85

Table 5.6 Changes of EOF per atom and electronegativity in transition metal elements

5.2.2.2 DOS calculation , distribution with different doping elements

To observe the effect of doping on the electronic properties of $LiMn_2O_4$ structures, the total DOS was investigated after doping with different elements. Figure 5.9 shows the total DOS of $LiMn_2O_4$ with and without Co doping. The shape of the total DOS diagram is shifted to higher energy states, especially in the higher energy region. In contrast, the total density of states of $LiMn_2O_4$ with Sn doping and Cr doping are shifted to lower energy states, as shown in Figure 5.10 and Figure 5.11, respectively. From our calculations, the overall trend of the total DOS is the same as the trend of EOF, as shown in Figure 5.8. Our calculations of DOS changes with transition metal elements are consistent with those in the literature [17, 18], which also showed that doping with transition metal elements changes the overall energy state of the DOS. Our results are also similar to those of previous reports [17, 18], which found that the electronegativity of the transition metal ion affects the changes in DOS.

To investigate changes in the oxidation state and electronic properties of Mn ions in the $LiMn_2O_4$ structure, the projected DOSs of Mn atoms with different doping elements were investigated. Figure 5.12 compares the projected DOSs of Mn atoms in $LiMn_2O_4$s with Cr doping, Cu doping, or no doping. It can be seen that doping with elemental Cu shifted the overall PDOS of the Mn atom to a higher energy level. As seen with the effects of orientation, a shift to the higher energy region makes it more difficult to fill the orbitals with electrons to create Mn^{3+} ions in the structure. This means that doping with Cu is an effective way to increase the oxidation state of manganese. However, doping with Cr shows the opposite behavior, compared with Cu doping, in the DOS state. Figure 5.12 shows that doping with Cr shifts the overall PDOS of the Mn atom to a lower energy level. Projecting the DOS of the Mn atom in the Cr-doped structure gave results that were opposite of the predictions that doping with metals of low oxidation number will increase the overall energy state to higher level. It seems the electronegativity of the transition metal element might be more related to the PDOS of the Mn atom than the oxidation number of the doping element. Doping with a transition metal element of higher electronegativity shows larger energy shift in the PDOS of the Mn atom.

On the other hand, Figure 5.13 shows the comparisons between projected DOS of the Mn atom in the $LiMn_2O_4$ structure with Mg doping, Sn doping, or no doping. Figure 5.13 shows that doping with either Mg or Sn increased the up-spin state below the Fermi level, whereas doping decreased the down-spin state above the Fermi level. These two PDOSs of the Mn atom in the Mg and Sn-doped structures do not show different trends, even though Mg and Sn have different oxidation numbers. Similarly, the DOS state of the Mn ion may not be directly related to the oxidation states of these two elements.

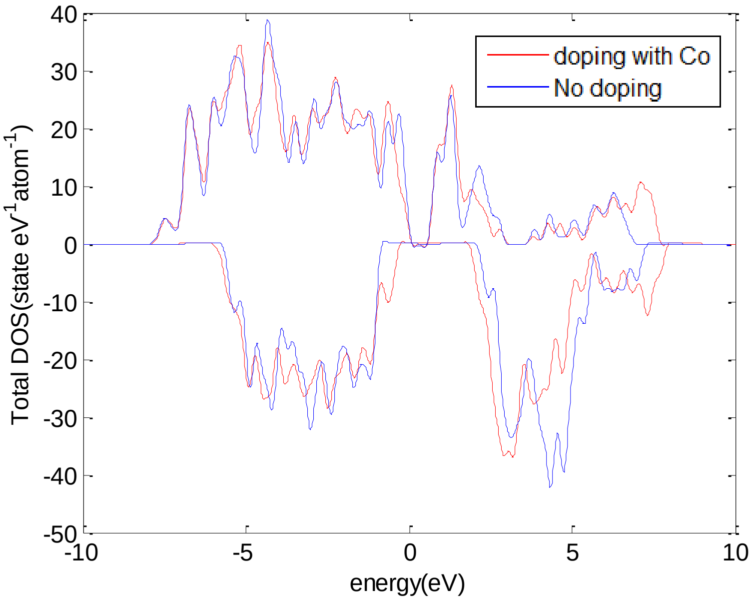

Figure 5.9 total DOS of $LiMn_2O_4$ structure with Co doping and without doping

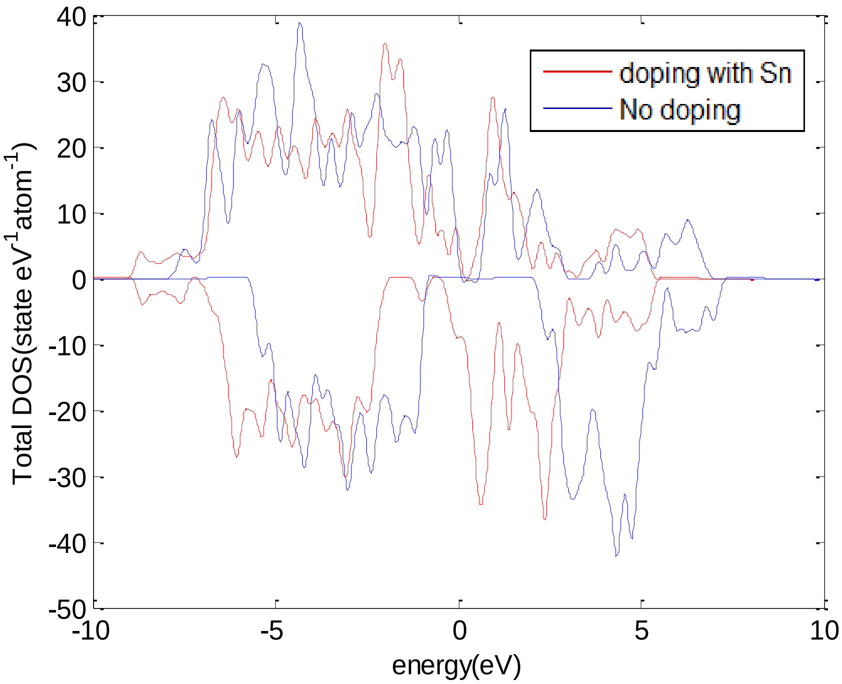

Figure 5.10 total DOS of $LiMn_2O_4$ structure with Sn doping and without doping

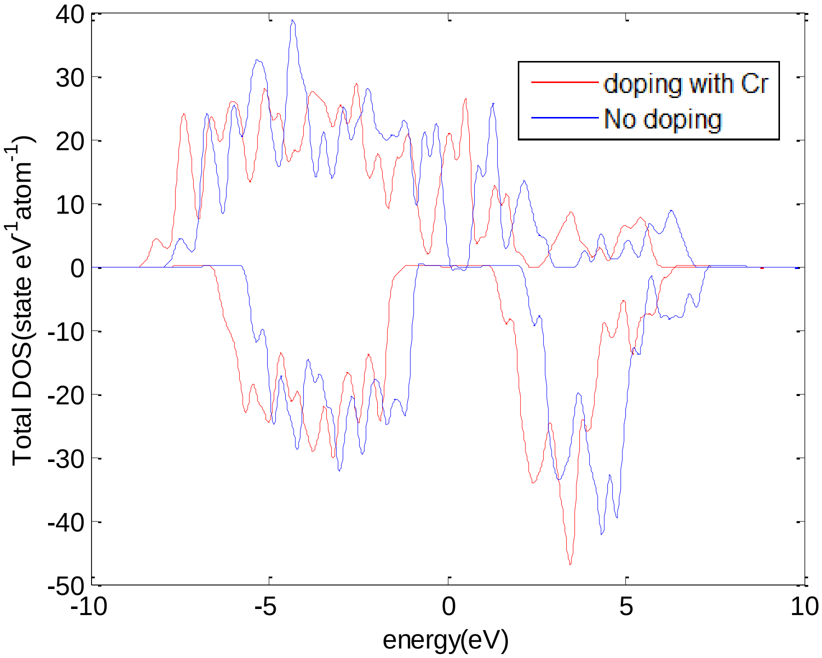

Figure 5.11 total DOS of $LiMn_2O_4$ structure with Cr doping and without doping

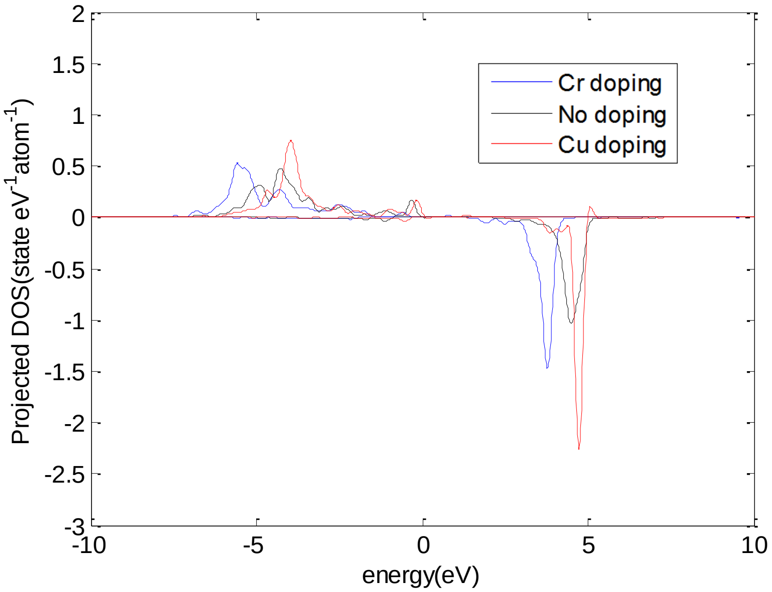

Figure 5.12 projected DOS of Mn atom of $LiMn_2O_4$ structure with Cr, Cu doping and without doping

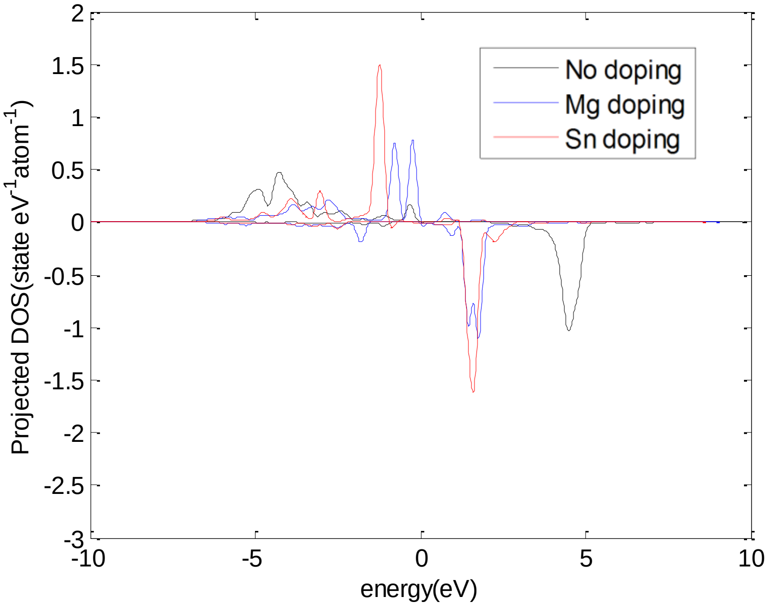

Figure 5.13 projected DOS of Mn atom of $LiMn_2O_4$ structure with Mg, Sn doping and without doping

5.2.2.3 COHP (Crystal Orbital Hamiltonian Population) analysis

To further expand our understanding of the electronic and bonding properties of Mn, the COHP (Crystal Orbital Hamiltonian Population) of Mn in structures with different dopings were investigated. A COHP diagram gives information regarding bonding, anti-bonding, and non-bonding energy regions within a specified energy range. COHP divides the band-structure energy into the sum of orbital interactions [42-44]. If there are bonding contributions, the system energy is lowered, and the COHP has a negative value. Conversely, if there are anti-bonding contributions, the COHP has a positive value. Figure 5.14, Figure 5.15, and Figure 5.16 compare the COHP diagram of the manganese atom in a $LiMn_2O_4$ structure without doping to those doped with Cu, Sn, or Mg. The x-axis of the diagram indicates the negative value of the COHP. This means that values in the figure that are >0 indicate a bonding state and negative values of –COHP indicate an anti-bonding state of the Mn atom. The zero energy state of the diagram is adjusted to the Fermi energy.

When we compare the bonding state below the Fermi level (when all the electrons are filled in the atom), the Mn atom with Cu doping shows more bonding state and less anti-bonding state than the Mn atom without doping, as shown in Figure 5.14. This result is the exact opposite of the results displayed by the Mn atom with Sn doping, which shows less bonding state and more anti-bonding state of the Mn atom, as shown in Figure 5.15. A state showing more covalent bonding and less anti-bonding increases the covalency of the Mn-O bonds, which reduces Mn dissolution. At higher temperatures, a number of electrons become activated over the Fermi level. A sharp peak of positive (anti-bonding) COHP appears in the lower energy above the Fermi level in the Mn atom with Sn doping. If an anti-bonding state dominates above the Fermi level, electronic instability it is expected to be increased. However, the positive peak (anti-bonding) of the COHP decreases in the Mn atom with Cu doping. This result indicates that doping with Sn ions is likely to decrease stability at higher temperature, which will aggravate Mn dissolution. Doping with Mg ions results in a state with more covalent bonding and less anti-bonding as shown in Figure 5.16. Although overall energy state is decreased after doping with Mg, as seen with Sn doping, there are more COHP in the stable energy state (low energy state near -20 eV) than without doping. These results also indicate that doping with Mg is beneficial for preventing Mn dissolution.

To compare the bonding characteristics with different doping elements numerically, total integrations of the COHPs with different doping elements were performed. Table 5.7 shows the values of the total integrals of the COHPs with different dopings, with respect to the energy where all the electrons are filled in manganese atom. Energy integration of the COHP represents a chemical bond to the distribution of specific atom energies. [42] These results show that doping with Co, Cr, Cu, Fe, Mg and Ni increase the bonding state of the Mn-O bond. However, doping with Sn increased the anti-bonding state. These results are consistent with experimental results from the literature, which showed that doping with Sn increases Mn dissolution whereas doping with other elements decreases Mn dissolution. From the COHP analysis, element doping was beneficial to increase the Mn-O bonding state in the order of Mg, Ni, Co, Fe, Cr and Cu below the Fermi energy level. However, these elements also affect the oxidation state of Mn in $LiMn_2O_4$ structure at higher temperature. For instance, Mg- doped $LiMn_2O_4$ structure have more Mn^{3+} oxidation state at higher temperature because DOS of e_g orbital above Fermi energy will decrease to the lower energy region. Although Mg doping will increase the bonding state of Mn-O bonds, high temperature will increase the Mn^{3+} oxidation state which will increase the instability of the structure.

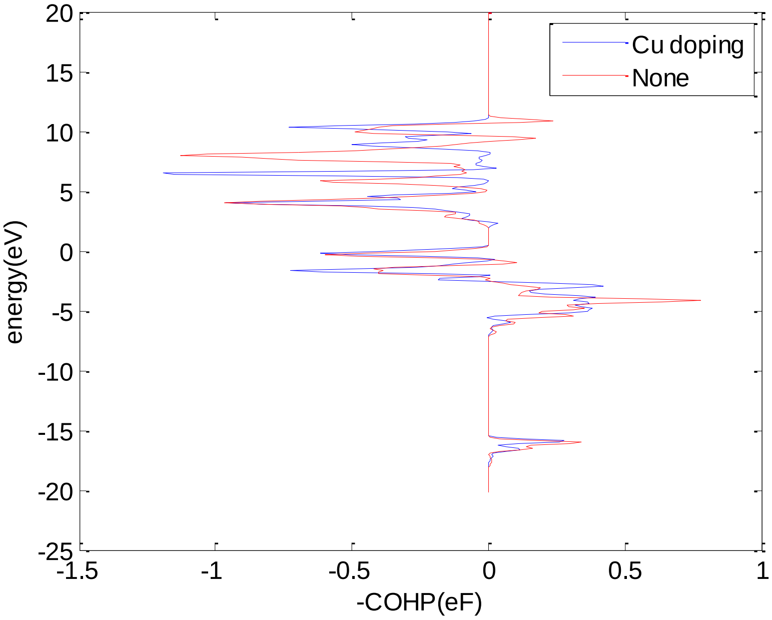

Figure 5.14 COHP diagram of manganese atom of $LiMn_2O_4$ structure with Cu doping and with doping

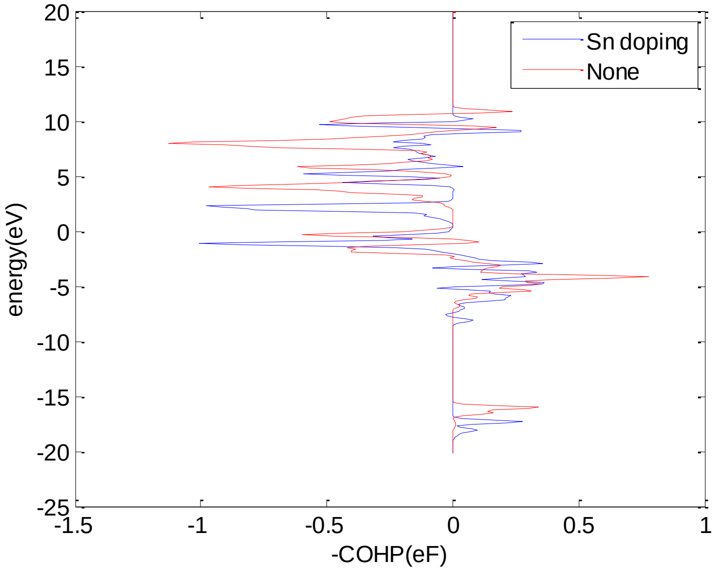

Figure 5.15 COHP diagram of manganese atom of $LiMn_2O_4$ structure with Sn doping and with doping

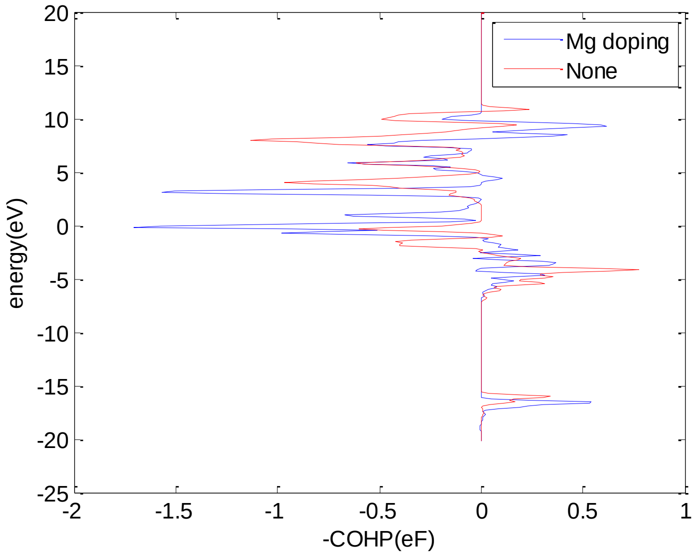

Figure 5.16 COHP diagram of manganese atom of $LiMn_2O_4$ structure with Mg doping and with doping

Doping element	Integration of COHP(eF)	change (%)
no doping	-1.3089	0
Co	-1.53937	17.60791504
Cr	-1.36651	4.401405761
Cu	-1.31086	0.14974406
Fe	-1.40853	7.611735045
Mg	-2.18478	66.91725877
Ni	-1.59129	21.57460463
Sn	-1.06316	-18.7745435

Table 5.7 Integration of COHP value and changes with different doping elements

5.3 Conclusions

The effect of surface orientations and doping on the dissolution of Mn ions from $LiMn_2O_4$ structures was investigated using first-principle calculations. Specifically, the changes in surface stability, manganese oxidation state, manganese vacancy EOF, electronic properties and bonding properties with different surface orientations and element doping were examined. To validate the model of the surface structure and doped structures of $LiMn_2O_4$, their surface energy and average intercalation voltage were compared with the results of several previous studies.

Based on our results, surface orientations with a larger number of Mn-O bonds and smaller bond length require more energy to break the Mn-O bonds. The Mn vacancy formation energies showed that increasing energy is needed to break the Mn-O bond in the surface orientations (001), (111), and (110). These results agree with the PDOS of the Mn atom, which shows that the (001) surface has the lowest possibility to be in the 3+ oxidation state and the (110) surface has the highest possibility to be in the 3+ oxidation state.

Changes in the electronic and bonding properties of Mn atoms due to different doping elements were investigated. Within the transition metal elements, a DOS analysis showed that the Mn ion PDOS is more related to the electronegativity of the doping element than the oxidation state of the doping element. However, doping with Mg and Sn does not show the specific trend with respect to changes in the Mn PDOS. To further investigate the electronic and bonding properties of the Mn atoms, a COHP analysis was conducted with different doping elements. Doping with Co, Cr, Cu, Fe, Mg and Ni increase the bonding state of the Mn-O bond, whereas doping with Sn decreases the bonding state. These results are consistent with the experimental results from previous literature, which showed that doping with Sn increases Mn dissolution whereas doping with other elements decreases Mn dissolution. From the COHP analysis, element doping was beneficial to increase the Mn-O bonding state in the order of Mg, Ni, Co, Fe, Cr and Cu below the Fermi energy level. However, these elements also affect the oxidation state of Mn in $LiMn_2O_4$ structure at higher temperature. In order to understand overall transition metal dissolution, both bonding state and oxidation state should be considered.

In conclusion, Mn dissolution from $LiMn_2O_4$ structures is strongly correlated with the electronic properties and bonding properties of the structure's Mn-O bonds. It is important to understand the electronic and bonding properties of these Mn-O bonds to prevent Mn dissolution. In addition, avoiding unstable Mn^{3+} is important to prevent Jahn-teller distortions and disproportionation reactions at higher energy states of the structure.

BIBLIOGRAPHY

[1] P. Arora, R.E. White, M. Doyle, Journal of The Electrochemical Society, 145 (1998) 3647-3667.

[2] Y. Dai, L. Cai, R.E. White, Journal of The Electrochemical Society, 160 (2013) A182-A190.

[3] D. Zhang, B.S. Haran, A. Durairajan, R.E. White, Y. Podrazhansky, B.N. Popov, Journal of Power Sources, 91 (2000) 122-129.

[4] J. Vetter, P. Novak, M.R. Wagner, C. Veit, K.C. Möller, J.O. Besenhard, M. Winter, M. Wohlfahrt-Mehrens, C. Vogler, A. Hammouche, Journal of power sources, 147 (2005) 269-281.

[5] J. Shim, R. Kostecki, T. Richardson, X. Song, K.A. Striebel, Journal of Power Sources, 112 (2002) 222-230.

[6] L. Yang, M. Takahashi, B. Wang, Electrochimica Acta, 51 (2006) 3228-3234.

[7] W. Choi, A. Manthiram, Journal of The Electrochemical Society, 153 (2006) A1760-A1764.

[8] M.-R. Huang, C.-W. Lin, H.-Y. Lu, Applied Surface Science, 177 (2001) 103-113.

[9] R. Benedek, M.M. Thackeray, Physical Review B, 83 (2011).

[10] A. Karim, S. Fosse, K.A. Persson, Physical Review B, 87 (2013) 075322.

[11] M. Hirayama, H. Ido, K. Kim, W. Cho, K. Tamura, J.i. Mizuki, R. Kanno, Journal of the American Chemical Society, 132 (2010) 15268-15276.

[12] R. Koksbang, J. Barker, M.Y. Saïdi, K. West, B. Zachau-Christiansen, S. Skaarup, Solid State Ionics, 83 (1996) 151-157.

[13] A. Osnis, M. Kosa, D. Aurbach, D.T. Major, The Journal of Physical Chemistry C, 117 (2013) 17919-17926.

[14] B. Xu, 'Develop high energy high power Li-ion battery cathode materials: a first principles computational study', (2012).

[15] Y. Ein-Eli, J.T. Vaughey, M.M. Thackeray, S. Mukerjee, X.Q. Yang, J. McBreen, Journal of the Electrochemical Society, 146 (1999) 908-913.

[16] L.u.r. Benco, J.-L. Barras, M. Atanasov, C.A. Daul, E. Deiss, Solid State Ionics, 112 (1998) 255-259.

[17] S. Shi, C. Ouyang, D.-s. Wang, L. Chen, X. Huang, Solid State Communications, 126 (2003) 531-534.

[18] S. Shi, D.-s. Wang, S. Meng, L. Chen, X. Huang, Physical Review B, 67 (2003) 115130.

[19] Y. Liu, T. Fujiwara, H. Yukawa, M. Morinaga, Computational Materials Science, 22 (2001) 309-317.

[20] S.H. Buta, 'A first prinicples investigation of transitional metal doping in lithium battery cathode materials ',(1999).

[21] M.E.A. y de Dompablo, J. Morales, Journal of The Electrochemical Society, 153 (2006) A2098-A2102.

[22] Y.M. Chiang, D.R. Sadoway, Y.I. Jang, B. Huang, H. Wang, Electrochemical and Solid-State Letters, 2 (1999) 107-110.

[23] T. Tsuji, M. Nagao, Y. Yamamura, N. Tien Tai, Solid State Ionics, 154–155 (2002) 381-386.

[24] H.J. Bang, V.S. Donepudi, J. Prakash, Electrochimica Acta, 48 (2002) 443-451.

[25] D.H. Jang, Y.J. Shin, S.M. Oh, Journal of The Electrochemical Society, 143 (1996) 2204-2211.

[26] D.H. Jang, S.M. Oh, Journal of The Electrochemical Society, 144 (1997) 3342-3348.

[27] J.M. Tarascon, E. Wang, F.K. Shokoohi, W.R. McKinnon, S. Colson, Journal of The Electrochemical Society, 138 (1991) 2859-2864.

[28] J.-W. Song, C.C. Nguyen, H. Choi, K.-H. Lee, K.-H. Han, Y.-J. Kim, S. Choy, S.-W. Song, Journal of The Electrochemical Society, 158 (2011) A458-A464.

[29] R.J. Gummow, A. de Kock, M.M. Thackeray, Solid State Ionics, 69 (1994) 59-67.

[30] X. He, J. Li, Y. Cai, Y. Wang, J. Ying, C. Jiang, C. Wan, Journal of Power Sources, 150 (2005) 216-222.

[31] X. He, W. Pu, Y. Cai, X. Wang, C. Jiang, C. Wan. ACTA CHIMICA SINICA, 63 (2005) 1853-1856.

[32] Y. Kim, J. Lim, S. Kang, International Journal of Quantum Chemistry, 113 (2013) 148-154.

[33] R. Benedek, M.M. Thackeray, J. Low, T. Bučko, The Journal of Physical Chemistry C, 116 (2012) 4050-4059.

[34] C.Y. Ouyang, S.Q. Shi, M.S. Lei, Journal of Alloys and Compounds, 474 (2009) 370-374.

[35] Y. Koyama, I. Tanaka, H. Adachi, Y. Uchimoto, M. Wakihara, Journal of The Electrochemical Society, 150 (2003) A63-A67.

[36] M.K. Aydinol, G. Ceder, Journal of The Electrochemical Society, 144 (1997) 3832-3835.

[37] C.H. Shen, R.S. Liu, R. Gundakaram, J.M. Chen, S.M. Huang, J.S. Chen, C.M. Wang, Journal of Power Sources, 102 (2001) 21-28.

[38] C.M. Julien, A. Mauger, Ionics, 19 (2013) 951-988.

[39] B. Xu, 'Develop high energy high power Li-ion battery cathode materials: a first principles computational study',(2012).

[40] K. Amine, H. Tukamoto, H. Yasuda, Y. Fujita, Journal of Power Sources, 68 (1997) 604-608.

[41] M.D. Goncalves, P.S. Maram, R. Muccillo, A. Navrotsky, Journal of Materials Chemistry A, 2 (2014) 17840-17847.

[42] R. Dronskowski, P.E. Bloechl, The Journal of Physical Chemistry, 97 (1993) 8617-8624.

[43] V.L. Deringer, A.L. Tchougréeff, R. Dronskowski, The Journal of Physical Chemistry A, 115 (2011) 5461-5466.

[44] S. Maintz, V.L. Deringer, A.L. Tchougréeff, R. Dronskowski, Journal of computational chemistry, 34 (2013) 2557-2567.

CHAPTER 6

CONCLUSIONS AND FUTURE WORK

6.1 Conclusions

The current research aims to improve cycle and calendar life of Lithium-ion battery system by 1) investigating manganese dissolution and deposition mechanisms, 2) predicting cell degradations, 3) presenting optimized ratio for composite electrodes, and 4) presenting guidance to reduce manganese dissolution. To obtain the results, a number of experiments were conducted to understand degradation phenomena and to provide input parameters for simulations. Multi-scale simulations were implemented on both the cell scale and the atomistic scale level to predict the cycle life of systems and to investigate and prevent manganese dissolution, respectively. Moreover, comparisons between experiments and cell scale level simulations were conducted to gain an advanced understanding of degradation mechanisms and validate the modeling works.

The current study revealed that both active material loss and electrode degradation due to transition metal dissolution critically influence cell performance. Moreover, dissolved metal ions accelerate the formation of the decomposed layer on the anode surface and continuously cause capacity fade. These results suggest that reducing metal dissolution is necessary to improve capacity and cell performance. This dissertation presents effective solutions to reduce metal dissolution by optimizing composition ratio of composite cathode electrode and doping on to the electrode.

The following is a brief summary of findings from each chapter.

In Chapter 2, a series of $LiMn_2O_4$ composite electrode degradations and their impact on cell performance were investigated in this study, which features unique improvements in both experiments and simulations. Specifically in this chapter, this study focused on cathode degradation in the cell. It included parameter changes of the cathode electrode due to manganese ions, along with key input parameters measured using different analytical techniques. It also featured an improved electrochemical model that considered both side reaction mechanisms and degradations of the electrode. The simulations and experiments showed that active material decreased 4% and capacity decreased 9 % after 50 cycles due to side reactions. This result indicates that capacity decreased approximately 5% during 50 cycles as a result of changes in contact resistance, diffusion coefficient, and reaction rate coefficient due to degradations of cathode electrode. In conclusion, active material losses due to degradation mechanisms as well as parameter changes due to degradation of the electrode critically influence cell performance.

Chapter 3 focuses on side reactions of the negative electrode. A thorough investigation of side reactions caused by dissolved manganese ions on graphite composite electrode was conducted based on complementary measurement techniques including CV, EIS, GCPL, ICP-OES, SEM and EDS. It is observed that the formation of the decomposed layer is accelerated by formation of reactive metallic manganese on the graphite surface and continuously causes capacity fade. Due to the higher reactivity of manganese on the surface, electrolyte reduction accelerates when the higher concentration of manganese in the electrolyte is added to the cell. Due to solvent reduction and SEI formation at initial cycle, charge capacity of the cell decreased 37% when adding 200ppm of manganese ions and only 17% when no manganese ions was injected. Moreover, the amount of lithium de-inserted from the graphite anode also increases due to manganese deposition. These processes also contribute to form thicker decomposed layers on the graphite surface and hinder the lithium transport process, which causes contact resistance and charge transfer resistance increase. After 20 cycles, about 15% of discharge capacity decreased when 200 ppm of manganese ions was added into the electrolyte.

Chapter 4 expands the focus of this research from $LiMn_2O_4$ materials to composite electrode by considering the effect of conductive additives and polymer binder. Numerical simulations were performed using updated simulation parameters with different composition ratio among active material, carbon black, and PVDF binder in $LiMn_2O_4$ composite electrode. At initial cycle, the simulation predicted that difference of the discharge capacity was up to 10% in the case of C/PVDF = 0.4 compared to the C/PVDF = 1. This difference is mainly originated from the difference in interfacial resistance among different samples. However, the capacity difference was narrowed to 8 % after 100 cycles due to the Mn dissolution. It is found that composition ratio among active material, carbon black, and PVDF binder in $LiMn_2O_4$ composite electrode is important factor that determines the battery performance. The composition ratio should be carefully considered and optimized to maximize the battery performance.

Lastly, the effect of surface orientations and doping on the dissolution of Mn ions from $LiMn_2O_4$ structure using the first principle calculation was investigated in Chapter 5. Specifically in this chapter, investigations of the changes in surface stability, oxidation state of manganese, the enthalpy of formation (EOF) of manganese vacancy, electronic properties and bonding properties with different surface orientations and element doping were investigated in Chapter 5. The results suggest that surface orientations with a larger number of Mn-O bonds and smaller bond length require more energy to break the Mn-O bonds. The Mn vacancy formation energies showed that increasing energy is needed to break the Mn-O bond in the surface orientations (001), (111), and (110). These results are consistent with the PDOS of the Mn atom, which shows that the (001) surface has the lowest possibility to be in the 3+ oxidation state and the (110) surface has the highest possibility to be in the 3+ oxidation state.

According to the COHP analysis, element doping was also beneficial to increase the Mn-O bonding state in the order of Mg, Ni, Co, Fe, Cr, and Cu below the Fermi energy level. Moreover, these elements also affect the oxidation state of Mn in $LiMn_2O_4$ structure at higher temperature. Thus, it is suggested that Mn dissolution is strongly correlated with both electronic properties and bonding properties of Mn-O bonds. In addition, avoiding unstable Mn^{3+} is important to prevent Jahn-teller distortions and disproportionation reactions at higher energy state of the structure.

6.2 Future Work

This dissertation investigates the fundamental physics underlying degradation mechanisms and presents effective solutions for minimizing metal dissolution and improving battery cell performance. To advance the current work, future work needs to consider 1) modeling the current experiment findings to describe the cell behavior quantitatively, 2) improving our current modeling by including more key parameters and degradation phenomena, and 3) further exploring the applications of the method developed from the current research. The followings are some examples of the future work extended from the current work.

6.2.1 **Modeling Side reactions due to Mn deposition and SEI layer interactions**

In Chapter 3, a thorough investigation of both manganese (Mn) deposition onto graphite and its side reactions is conducted based on complementary techniques including CV, EIS, GCPL, ICP-OES, SEM and EDS. It is found that the formation of the decomposed layer is accelerated by formation of reactive metallic manganese on the graphite surface. Also, battery cell experience non-passivation of the film layer contaminated by manganese ions. To quantitatively describe the interaction between manganese deposition and SEI layer, modeling work will be performed in the future.

6.2.2 **Optimizing current and Future composite electrode**

Chapter 4 focused on the effect of active material, conductive additives and binder from $LiMn_2O_4$ composite electrode on capacity fade in terms of manganese dissolution, conductivity and binder effect. It is found that higher ratio of polymer binder to conductive additives increase the interfacial resistance by ion- blocking effect at higher binder contents in the electrode. Moreover, increase in carbon contents of the electrode results in increase of dissolved manganese ions from the $LiMn_2O_4$ composite electrode. In addition to lower the specific capacity of the cell, inclusion of conductive additives and polymer binder also influence different properties and parameters of the battery performance. Therefore, there will be optimal ratio between active material, conductive additives and binder on the battery performance and battery health. By considering these effects affecting battery performance, optimal ratio between active material, carbon black and PVDF binder will be investigated to help understand and design battery system.